Doctoral Dissertations   Graduate School

12-2007

Processing and Phase Formation in Zr-Based Bulk-Metallic Glass-Forming Alloys

James Joseph Wall
University of Tennessee - Knoxville

Recommended Citation

To the Graduate Council:

I am submitting herewith a dissertation written by James Joseph Wall entitled "Processing and Phase Formation in Zr-Based Bulk-Metallic Glass-Forming Alloys." I have examined the final electronic copy of this dissertation for form and content and recommend that it be accepted in partial fulfillment of the requirements for the degree of Doctor of Philosophy, with a major in Materials Science and Engineering.

Peter K. Liaw, Major Professor

We have read this dissertation and recommend its acceptance:

Hahn Choo, Chain T. Liu, Dayakar Penumadu

Accepted for the Council:

Carolyn R. Hodges

Vice Provost and Dean of the Graduate School

(Original signatures are on file with official student records.)

To the Graduate Council:

I am submitting herewith a dissertation written by James Joseph Wall entitled "Processing and Phase Formation in Zr-Based Bulk-Metallic Glass-Forming Alloys". I have examined the final electronic copy of this dissertation for form and content and recommend that it be accepted in partial fulfillment of the requirements for the degree of Doctor of Philosophy, with a major in Materials Science and Engineering.

<div align="right">

_____

Peter K. Liaw, Major Professor

</div>

We have read this dissertation
and recommend its acceptance:

_____

Hahn Choo

_____

Chain T. Liu

_____

Dayakar Penumadu

<div align="right">

Acceptance for the Council:

_____

Carolyn R. Hodges, Vice Provost
and Dean of the Graduate School

</div>

Original signatures on file with the official student records

PROCESSING AND PHASE FORMATION IN Zr-BASED BULK-METALLIC

GLASS-FORMING ALLOYS

A Dissertation
Presented for the
Doctor of Philosophy Degree
The University of Tennessee, Knoxville

James Joseph Wall
December 2007

Dedication

This work is dedicated to Jessica, who showed me the way to the path through the woods…

Acknowledgements

Abstract

Bulk-metallic glasses have established a formidable presence in the scientific community in recent years, due to a number of properties that are uncharacteristic of metallically-bonded materials. One of the fundamental challenges facing researchers in this field is to develop new and improved processing methods with the ultimate goal of facilitating a large-scale industrial integration of the materials.

The research described herein is directed toward the pursuit of developing and improving upon the current state-of-the art in the science of bulk-metallic glass processing. A number of research and development projects were undertaken in this pursuit. First, the technology to process bulk-metallic glasses at the University of Tennessee was developed and successfully implemented. Second, bulk-metallic glasses were produced using aerodynamic levitation, which showed an improvement over the accessible cooling rates achievable employing other containerless-processing methods. Third, erbium was found to be a superior dopant to other rare-earth elements to neutralize the oxygen in a Zr-based glass-forming alloy. The alloy was found to form a glass in the presence of up to 16,000-atomic-ppm oxygen by microalloying with Er, with a relatively minor effect on the thermal and mechanical integrity of the materials. Fourth, metastable intermetallic phases were identified in as-cast VIT-105 alloy materials that contained oxygen, using diffraction. The diffraction study included the whole pattern fitting of diffraction from crystalline species in a BMG, an analytical approach that, if existing at all in the literature, is quite rare. Furthermore, this study included a novel approach to fitting diffraction from the glass. Fifth, oxygen-stabilized analogues to intermetallic

phases were found in the superheated-liquid state. The presence of Er was found to inhibit surface reoxidation, revealing its mechanism for the neutralization of oxygen. The results were used to propose a model for heterogeneous nucleation and the so-called "overheating threshold" in the alloy.

Table of Contents

Chapter 1: Introduction and Literature Review

1.1   General Introduction and Organization of the Dissertation

Over the past 20 years there has been a steadily increasing interest in the commercialization of bulk-metallic-glass (BMG) materials due to a number of atypical physical properties. One challenge that faces researchers in this emerging field is the development of the processing science, specifically, generating alloys and fabrication techniques that enhance the commercial viability of BMGs. In this dissertation, a background on the physical nature of the formation of glass and bulk-metallic glass processing is presented. This background information is followed by a number of experimental studies performed within the scope of the bulk-metallic-glass processing science.

In a general sense, this dissertation catalogues three years of research and development activities associated with the processing of Zr-based bulk-metallic glasses (BMGs). The research presented herein embodies a broad multidisciplinary scope, consisting of a number of processing-related components, rather than focusing on an individual materials-related issue. The current chapter discusses the history and physics of glass formation, leading into a discussion on processing ideology and methodology. The details of the analysis methods that were used for characterization studies are presented in Chapter 2, with the exception of those developed as a part of a particular investigation. The following chapters describe the individual research components. The

reader will notice that brief subject-matter specific *introductions*, as well as *conclusions* are presented in these chapters. The experimental descriptions in these chapters are limited in scope to detailed treatments of processing methods, as well as analysis methods that were developed specifically for the investigation. The final chapter presents a summation of the project that discusses what was gained from the research as a whole. General notes for each chapter and relevant vendor information are included in Appendix A. A schematic that illustrates the interrelationship among the themes of each chapter in this dissertation, and how they fit into the scope of the research is presented in Fig. 1.1.

A note to the Committee regarding format and content

The Committee Members will notice that, as was suggested in the previous section, Chapters 3 – 7 appear in a journal-article type format. The inclusion of co-authored journal articles in a dissertation is allowed per the policy of The University of Tennessee Office of Graduate Studies[1]. However, such chapters are normally preceded by a description of the student's contribution to the work. These descriptions do not appear in Chapters 3 through 7 of this dissertation, since I was the principal investigator in the associated studies and the primary author of the journal articles.

In addition, several experimental elements of the research were performed on a proprietary (or other) basis to benefit the project; hence, I did not participate directly in some of the associated experiments and/or analyses. As such, I claim no direct professional recognition for their appearance in this dissertation. These elements are noted below:

---

[1] *Guide to the Preparation of Theses and Dissertations / 10th Edition*, Knoxville: The University of Tennessee, 2003, p. 21.
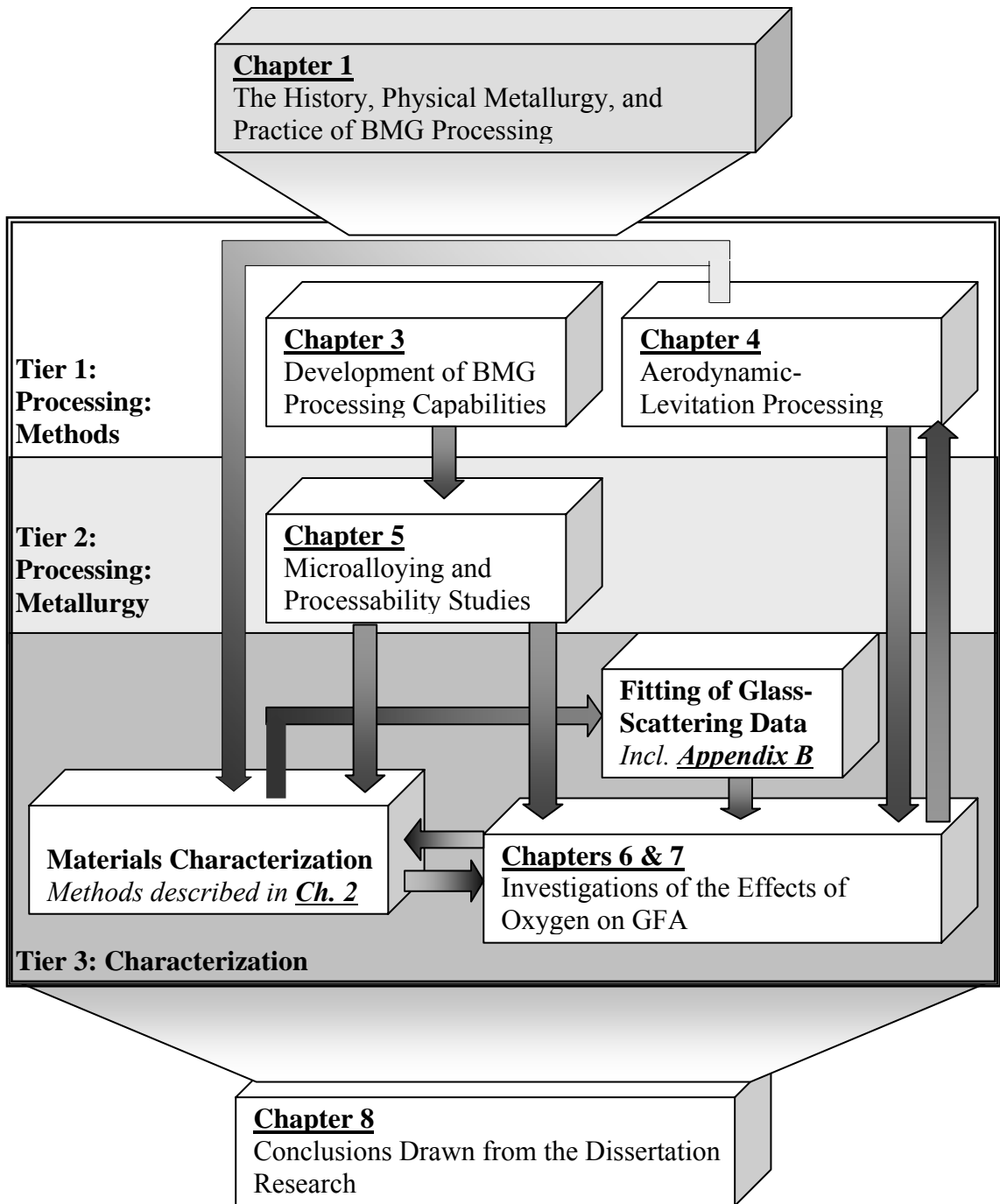
Figure 1.1 A schematic showing how the various research components are interrelated to benefit the global research theme of BMG processing science. The literature review and thermodynamic treatment of glass formation (Chapter 1) is provided to rationalize the experimental studies. The conclusions (Chapter 8) serve to merge the experimental components and present what was learned in the broad scope of the research.

1)   Chapter 4: (processing experiments).   The aerodynamic-levitation processing experiments were performed by the technical staff at Containerless Research, Inc. (CRI).   I provided the samples, defined the processing variables, analyzed the processing data, and conducted the forensic analyses on the as-processed samples.

2)   Chapter 5: (spectroscopic analyses).   The inductively-coupled plasma / optical-emission spectroscopy experiments and related analyses were performed by the technical staff at Shivatec, Inc. I provided the materials and defined the elements of interest for the spectroscopic studies.

3)   Chapter 6: (experimental technique).   The synchrotron x-ray beam-line aerodynamic-levitation experiments were performed by R. Weber of CRI, and Q. Mei and C. Bennmore, both of the Argonne National Laboratory. I provided the materials, defined the desired experimental conditions, and analyzed the scattering data.

4)   Chapter 7: (sample preparation). The raw materials for the electrostatic-levitation study were provided by C. T. Liu of UT and the Oak Ridge National Laboratory.

1.2   Definition of a Metallic Glass

A glass, by definition, is a material that is lacking in any long-range atomic periodicity. *Long-range*, in this context, is on the order of greater than a few atomic

distances (~ 10 Å). This characteristic is in contrast with crystalline materials, which exhibit a configurational order that can be described by a unit cell, which is a basal atomic configuration that is repetitious in 3-dimensional space. For practical purposes, a glass may be considered as a *disordered* material, although they consist of locally-ordered clusters. These ordered clusters, however, do not exhibit many of the properties that are commonly associated with grains, particularly with respect to deformation. The amorphous form of many materials is ubiquitous in nature, and they, in particular oxide glasses, have become a part of everyday life. *Metallic* glasses, alloys of metal elements[2], the compositions of which create a eutectic energy landscape that allows them to bypass cystallization and remain in their supercooled liquid configurations, were first produced by Duwez and co-workers in 1960 using $Au_{75}Si_{25}$ [1]. The first metallic glasses required very high cooling rates from the melt ($> 10^5$ K/s) to prevent nucleation and growth during processing, and, thus, could only be produced on μm-scale thicknesses using specialized rapid-quenching methods.   Rapid-quenching techniques, such as melt spinning and splat cooling, are still being used to probe, for example, the fundamentals of glass formation, phase separation, and crystal nucleation during reheating.

1.3   Origins and Emergence of Bulk-Metallic Glasses

*Bulk-metallic glass*es (BMGs), by contrast, are alloy compositions that experience a relatively easy transition from supercooled liquids to amorphous "solids"[3], allowing

---

[2] Note that elemental Zr has been shown to form a glass when exposed to extremely high pressures.
[3] In reference to BMGs the term "solid" does not refer to an equilibrium condition, but rather an atomic mobility threshold, related to the viscosity, at which the time to reach thermodynamic equilibrium becomes very large.

them to be produced in a monolithic form. The first bulk-metallic glasses were a Pd-Cu-Si ternary composition produced in 1974 by Chen et al. [2], who went on to produce other compositions in the Pt-Ni-P and Au-Si-Ge systems around this time [3]. Through the 1980's and early 1990's, the research groups of D. Turnbull, A. Inoue, and W. L. Johnson successfully identified glass-forming compositions in the Pd-Ni-P [4], Ln-Al-(Transition Metal) [5], and Zr-Ti-Cu-Ni-Be [6] systems, respectively, which showed excellent glass-forming abilities, allowing them to be prepared in a monolithic form with linear dimensions of ~ 1 cm. Based on these pioneering studies, a vast number of BMG-forming alloys have been identified by the aforementioned groups, as well as a multitude of others, ushering in a wave of scientific interest and progress in the field that continues today. Currently, there exist far more bulk glass-forming alloy compositions than were initially thought possible. These have been found in a number ternary, quaternaty, and higher-order systems, which may contain transition metals, lanthanides, and metalloids. Some noteworthy examples of these alloys are: $Zr_{52.5}Cu_{17.9}Ni_{14.6}Al_{10}Ti_5$ (VIT-105) [7], $[(Co_xFe_{1-x})_{.75}B_{.2}Si_{.05}]_{96}Nb_4$ [8], and the so-called "amorphous steels" [9, 10].

With the great many BMG-forming alloy compositions identified and their physical properties reasonably well understood, there are a multitude of potential applications for the materials. In addition to their anamolous physical properties (high strengths, high elastic limits, soft magnetic properties, etc..), possibilities exist for near-net-shape forming of BMGs by thermoplastic-forming methods, e.g., injection molding, near their glass-transition temperatures, T_g. This unique trait is due to their relative stability against crystallization in the supercooled-liquid region ($[T_x - T_g]$, T_x refers to the temperature at the onset of crystallization). In this region, metallic glasses undergo

softening as the viscosity, η, decreases several orders of magnitude, and the materials can be deformed by a homogeneous type flow. The first commercial venture to offer BMGs, Liquidmetal Technologies [11], was formed in 1987, and offers unique products and components in the areas of sporting goods, electronics, medical applications, and defense (Fig. 1.2).

In order to facilitate a large-scale commercialization of these materials, they must be able to compete, in a global marketplace, with more commonplace materials that can be processed inexpensively and with already existing equipment. Failure to do so will most likely limit them to niche markets and specialized applications. A number of research groups, as well as Liquidmetal Technologies, have made innovations in this area in the past several years, but the basic problem of the inadequate manufacturability of BMGs remains.

1.5   Glass Formation: Classical Nucleation Theory

1.5.1   Caveat

The most common way of preparing BMGs is cooling from the superheated-liquid state. In this context, glass formation in an alloy is essentially a cooperation between thermodynamics and kinetics. To *fundamentally* understand the science of BMG processing, one must possess an intimate knowledge of all of the governing processes, some of which are ambiguous at best. The definition of glass formation in

Figure 1.2   Examples of some commercial products made from bulk-metallic glass. Left is the Head Liquidmetal® Radical Racket, and right shows a Samsung mobile phone that uses injection-molded BMG hinges.

terms of thermodynamics and kinetics is an elegant one, but it does not explain every aspect. With that stated, the following is how I understand glass formation.

1.5.2   Thermodynamics and Kinetics of Glass Formation

The thermodynamic and kinetic aspects of glass formation can be reasonably well understood within the framework of the classical-nucleation theory. The thermodynamic-driving force for an undercooled alloy to nucleate crystalline precipitates is the difference in the Gibbs-free energy between the undercooled liquid and the solid, ΔG_{S-L}. This difference must be large enough to compensate for the energy required to create the solid/liquid interface, γ_{sl}, which is always positive and nonzero, for nucleation to occur[4]. As the net ΔG_{S-L} for a given amount of material is volume dependant, and the net γ_{sl} is surface-area dependant, the critical cluster radius, r^*, is defined as that at which the surface to volume ratio of the cluster makes nucleation energetically favorable for clusters with $r > r^*$:

$$r^* = \frac{2\gamma_{sl}}{\Delta G_{S-L}} \tag{1-1}$$

Thus, for small ΔG_{S-L} as one would encounter at shallow undercoolings, r^* is rather large, making nucleation statistically unlikely on laboratory time-scales. The driving force for crystal nucleation tends to become larger (r^* decreases) at increasingly

---

[4] This is not (exactly) so in the case of heterogoenous nucleation, which is discussed later.

deeper undercooling, as an alloy moves further below its melting point, making nucleation more likely. In a strictly thermodynamic sense, one would expect that the time for solidification to occur becomes very short for large undercoolings and eventually becomes physically unavoidable at some critical undercooling (the so-called Kauzmann temperature[5], T_K [12]). The thermodynamic aspects of glass formation can be visualized by considering the enthalpy, entropy, and Gibbs-free energy of the undercooled liquid as a function of the temperature (Figs. 1.3 - 1.5). The enthalpy of the transformation from the supercooled-liquid state to the crystalline-solid state, ΔH_{S-L}, is offset by the entropy change of the transformation, ΔS_{S-L}, at high temperatures, yielding the Gibbs-free energy, where:

$$\Delta G_{S-L} = \Delta H_{S-L} - T\Delta S_{S-L} \qquad (1\text{-}2)$$

At lower temperatures, ΔG_{S-L} is dominated by the enthalpy term, and the transformation is energetically maximized at T_K. If the material forms a glass before reaching T_K, it exists in a nonequilibrium state and remains there due to its very low atomic mobility[6].

Kinetics then, in the context of glass formation, becomes a critical factor. Glass formation occurs above T_K, as the atomic mobility decreases sharply with undercooling. Assuming a steady-state homogeneous nucleation, the nucleation rate in an undercooled liquid is [13]:

---

[5] At T_K, the entropy of the liquid, S_l, equals that of the solid, S_s. Further undercooling requires $S_l < S_s$, which is physically impossible, as it violates the 3rd law of thermodynamics.

[6] Note that as $t \to \infty$, the material will attain its equilibrium state. However, the amount of time required for this transformation to occur at room temperature makes it a negligible design consideration
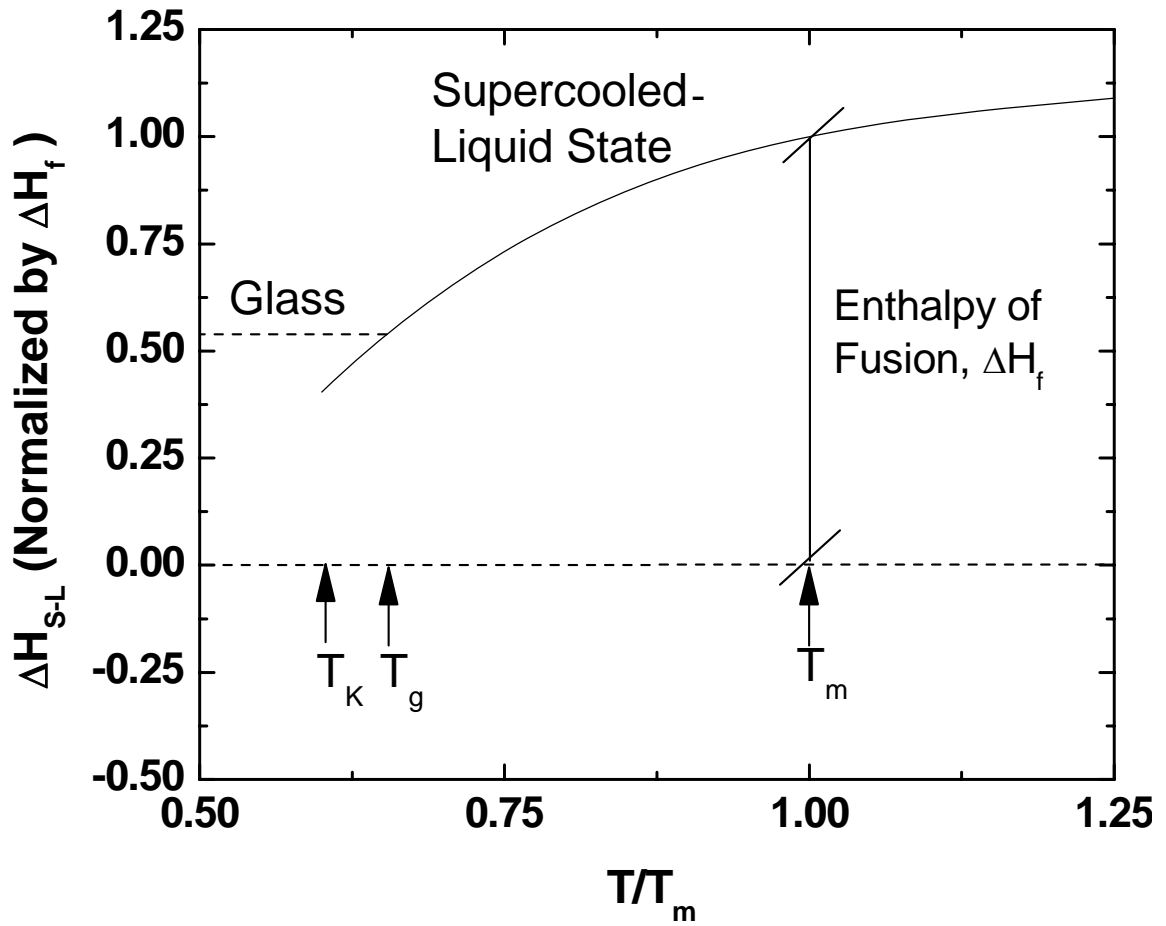
Figure 1.3   A hypothetical curve of the temperature dependence of the enthalpy of crystallization of a BMG-forming alloy in the supercooled-liquid state and after the glass transition.
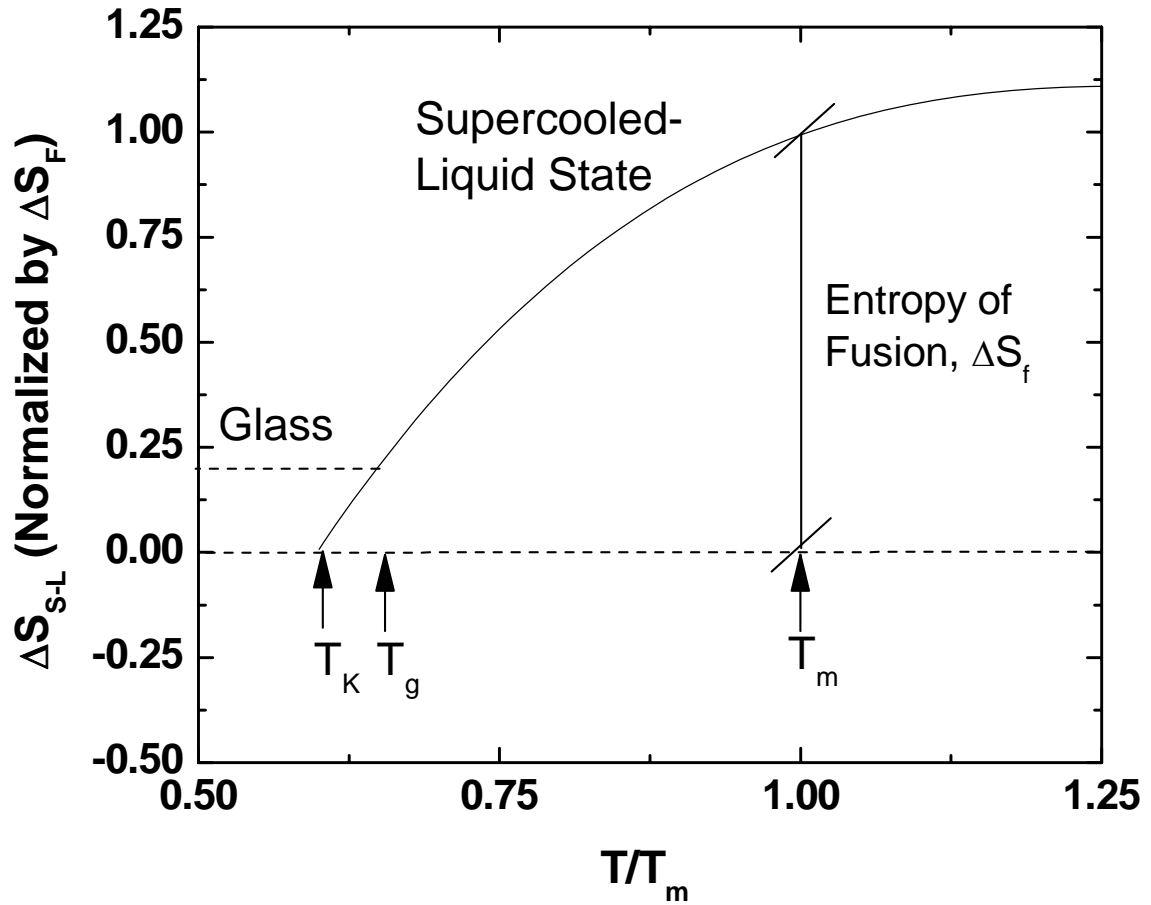
Figure 1.4   A hypothetical curve of the temperature dependence of the entropy of crystallization of a BMG-forming alloy in the supercooled-liquid state and after the glass transition.
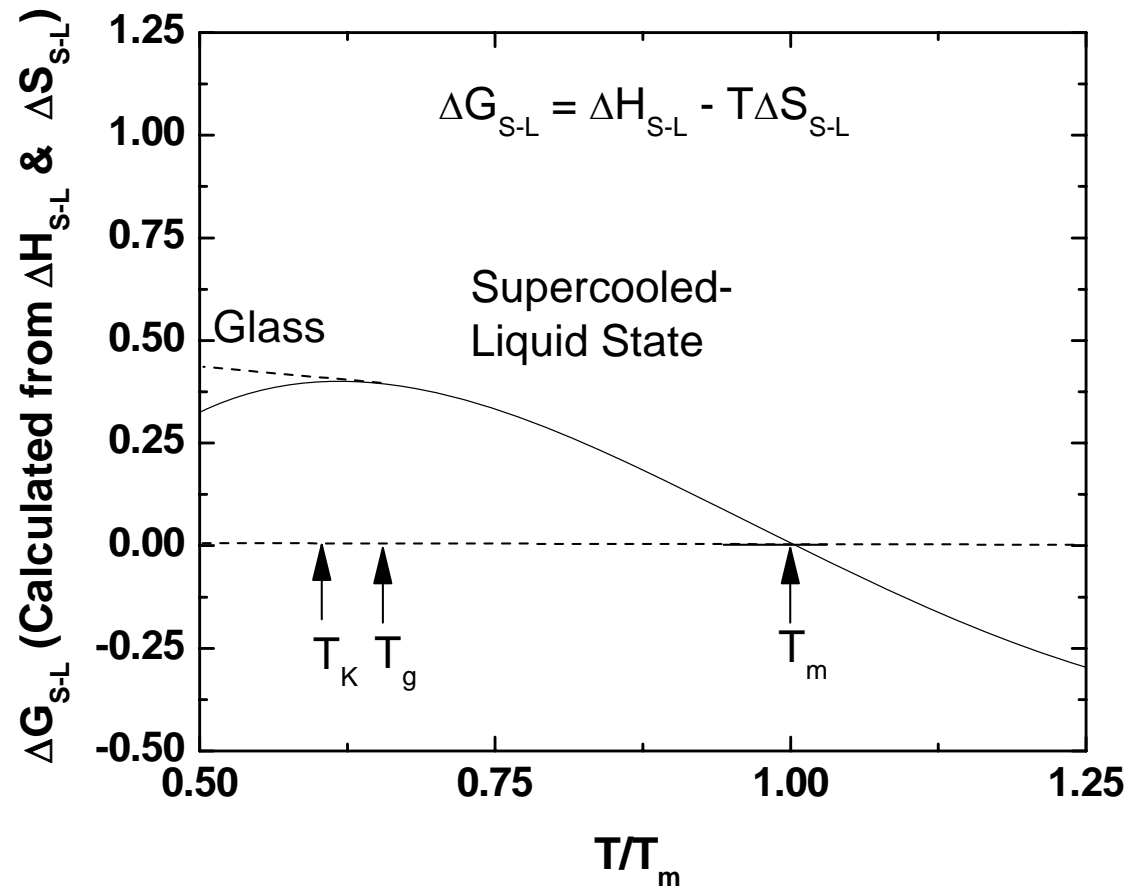
Figure 1.5 A hypothetical Gibbs-free-energy difference plot of a BMG-forming alloy in the supercooled-liquid state and after the glass transition.

$$N_v = C_0 D \exp\left(-\frac{\Delta G^*}{kT}\right)$$ (1-3)

where D is the effective diffusivity, C_0 is a constant, k is Boltzmann's constant, and the energy barrier for nucleation, ΔG^*, is:

$$\Delta G^* = \frac{16\pi\gamma_{sl}^3}{3(\Delta G_{S-L})^2}$$ (1-4)

As such, the stability of glass-forming alloys in the undercooled-liquid state is related to ΔG_{S-L} and the effective diffusivity [14]. In glass-forming compositions, ΔG_{S-L} is typically small, as they exist in deep eutectic energy wells, resulting in an exceptional stability of the liquid state below T_m.

In the context of the above discussion, the minimum cooling rate to bypass crystallization and form a glass, the so-called critical-cooling rate (CCR) may be defined as that at which, when solidification becomes energetically favorable, the viscosity, η (inversely proportional to the diffusivity by the Stokes-Einstein relation) is too high to facilitate a transformation to the equilibrium-crystalline solid. This is, of course, not an "all or nothing" event, as one approaches the CCR, and is essentially governed by statistics. The CCR, then, can be defined by setting a threshold crystalline volume fraction (e.g., $x = 10^{-6}$) that is considered to be a negligible amount in the glass. This convention allows one to define the CCR in terms of kinetics using a Johnson-Mehl-Avrami approach [15]:

$$x = 1 - \exp\left[-\left(\frac{\pi}{3}\right)N_v u^3 t^4\right] \qquad (1\text{-}5)$$

where u is the diffusion-controlled growth velocity of the crystalline phase. Using the approximation: $e^z \sim z$, for $z \ll 1$ and rearranging Eq. (1-5) yields the time to achieve a transformation:

$$t_x = \left(\frac{3x}{\pi N_v u^3}\right)^{\frac{1}{4}} \qquad (1\text{-}6)$$

The relationship between the kinetics and thermodynamics in a BMG-forming alloy and the nature of the CCR can be illustrated in a time-temperature-transformation (TTT) diagram (Fig. 1.6). Note that in the figure, the "nose" of the TTT curve is the left-most point of the curve. At temperatures greater than the "nose", dT/dt is positive (low ΔG and η), and ΔG^* is the limiting factor for nucleation. However, at temperatures lower than the "nose", dT/dt is negative (high ΔG and η), and the atomic mobility is the limiting factor.

1.5.3   Fragility, and an Entropy Model of Kinetics?

It was mentioned previously that glass formation may be considered as a *cooperation* between thermodynamics and kinetics. In my opinion, this is a very
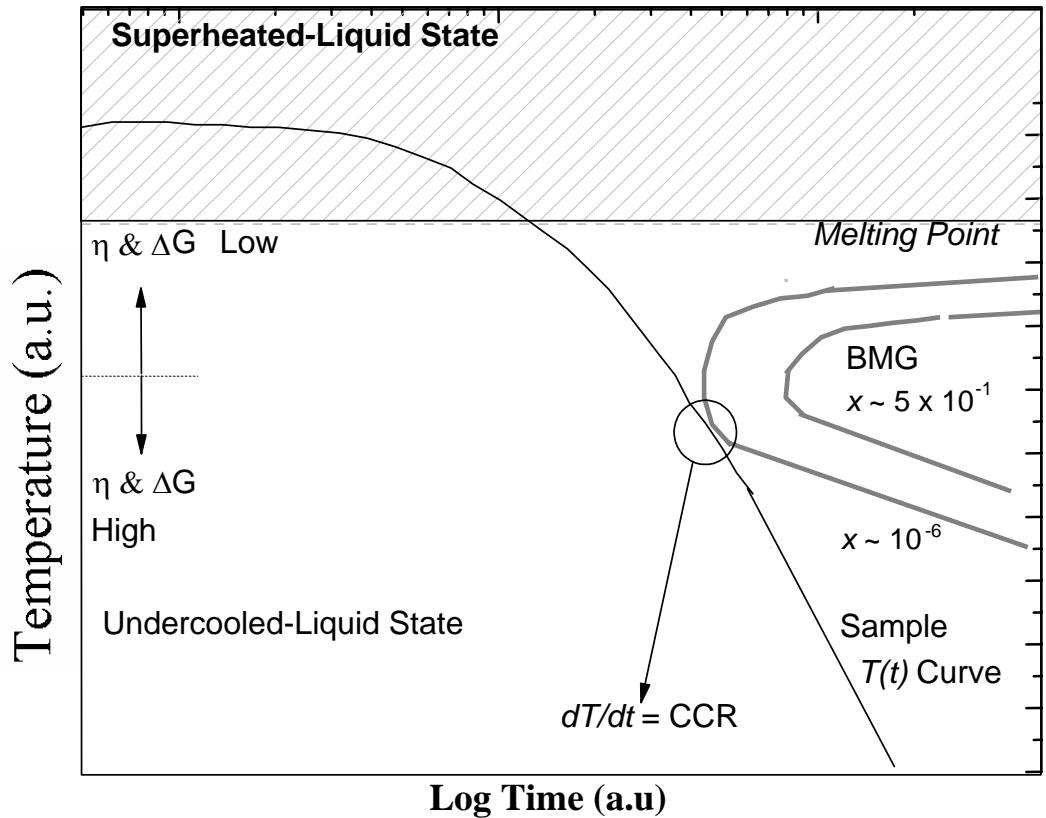
Figure 1.6   Hypothetical TTT curves of a BMG-forming alloy for $x \sim$ 10^{-6} and 5×10^{-1}. A higher glass-forming ability shifts the TTT curve to the right. The $T(t)$ curve is a hypothetical cooling curve from the melt (linear cooling). $\| dT/dt \|$ must be large enough to bypass the nose of the TTT curve or the material will contain crystallites.

effective way to understand glass formation, as it is based on chemical equilibrium states constrained by time. As it turns out, thermodynamics and kinetics may not be mutually exclusive physical properties of a material. To elaborate upon this concept, we must further define kinetics in terms of a liquid's viscosity. Angell, in a now famous paper in Science, proposed the concept of a liquid's *fragility*, Λ [16][7]. Λ was defined by Angell in terms of the viscosity, using a slightly-modified representation of the Vogel-Fulcher-Tammann model [15]:

$$\eta(T) = \eta_o \exp\left[\Lambda \frac{T_o}{(T - T_o)}\right]$$ (1-7)

where T is the temperature of the liquid, η_o is the extrapolated viscosity at $T = \infty$, and T_o is the Vogel-Fulcher-Tammann temperature, which is the extrapolated temperature at $\eta = \infty$. In this form, Λ indicates how well a liquid's temperature-dependant viscosity, Eq. (1-6), follows an Arrhenius behavior ($\Lambda = \infty$, $T_o = 0$). Relating Eq. 1-6 to the thermal properties of a glass using the relationship:

$$\frac{T_g}{T_o} = 1 + \frac{\Lambda}{2.303 \log\left(\frac{\eta_g}{\eta_o}\right)}$$ (1-8)

---

[7] The symbol *"D"* was used to represent the fragility in the original paper. I used the symbol *"Λ"* here to avoid confusion with effective diffusivity, defined as *"D"* in Eq. (1-2).

allows the construction of an Arrhenius plot of the viscosity of a glass-forming liquid, scaled by T_g, Fig. 1.7. Good glass-forming liquids, commonly called "Strong" liquids, are those that show a near-Arrhenius behavior, while poor glass-forming "fragile" liquids exhibit a distinct departure from this behavior. As such, the good glass-forming alloys, in a kinetic sense, show a relatively small change in the viscosity as a function of the temperature just above T_g. In more practical terms, "strong" liquids have an inherent tendency to remain in the liquid state as they approach the glass transition, while cooling from $T > T_g$, due to their poor atomic mobility. A liquid's *fragility*, then, is a quantitative physical measure of the kinetics of a glass.

During the course of this literature review, it became apparent that a commonly-held assumption within this field is that thermodynamics and kinetics are independent of one another. The idea that these are mutually exclusive physical phenomena seems intuitive, as thermodynamics is commonly thought of in terms of chemical energy equilibria, and kinetics, in terms of atomic-vibrational states. In 1999, Ito et al. [17] found that if the entropy of crystallization, ΔS_{S-L}, is plotted as scaled by T_g, its temperature evolution shows the same approximate character as the kinetic-fragility plot (Fig. 1.6) in water and several other liquids. The relationship, however, was unreliable at best [18] and was not applicable in some systems, thus far from any quantifiable general dependence phenomenon. However, in a recent article of Nature, Martinez and Angell [19] argue in support of revisiting the concept of a general thermodynamic definition of the kinetics of a liquid. Their approach was to redefine the entropy in terms of its configurational and vibrational components, S_c and $S_{e(vib)}$, respectively, where:
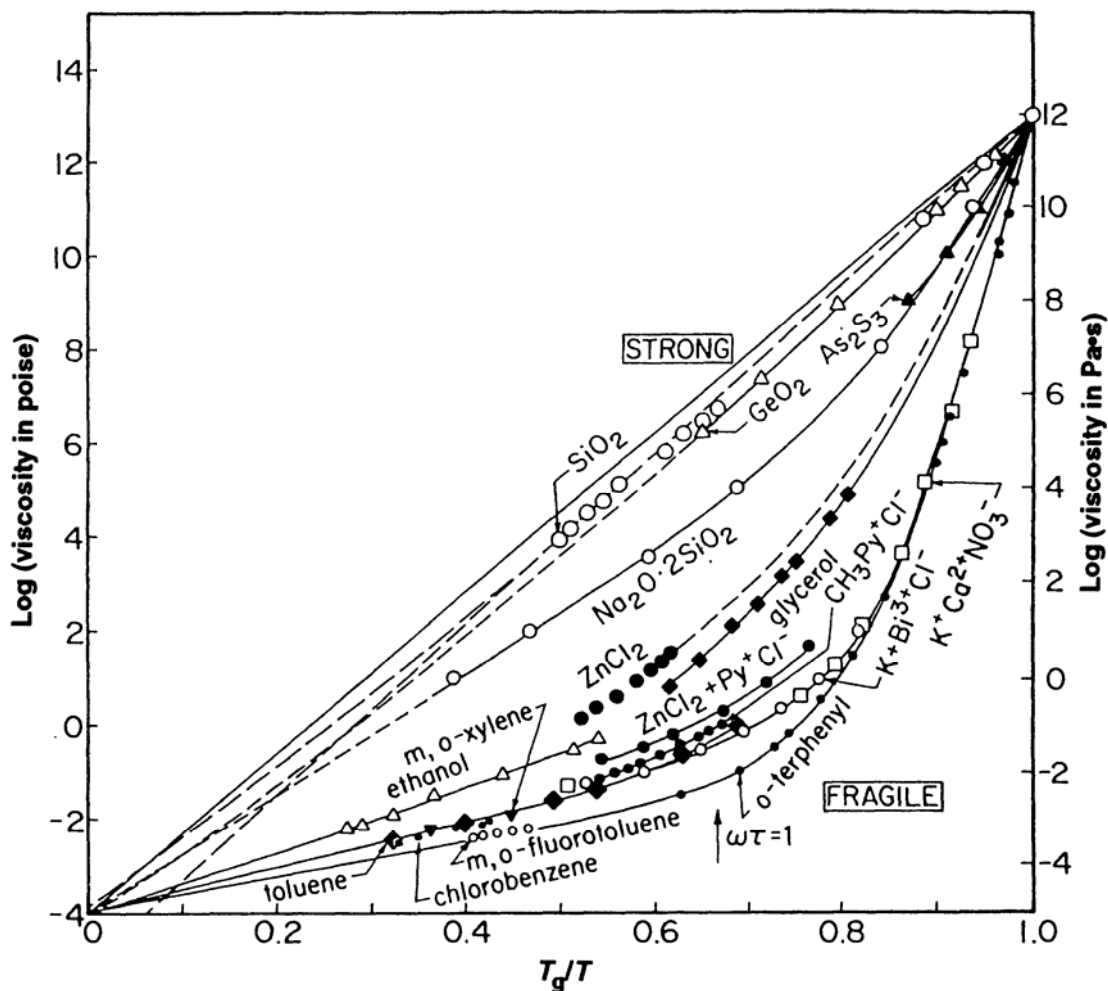
Figure 1.7   Arrhenius plots of η scaled by T_g for a number of liquids. Note that SiO_2, which very easily forms a glass, exhibits near-Arrhenius (strong) liquid behavior. Fragility, Λ, is a quantitative measure of the departure from an ideally-strong liquid. Note this figure was reproduced from Ref. [16].

$$\Delta S_{S-L}(T) = S_c(T) + S_{e(vib)}(T) \qquad\qquad (1\text{-}9)$$

The evolution of S_c and $S_{e(vib)}$ with the temperature in an undercooled liquid is shown in Fig. 1.8. The authors go on to state that the vibrational component of the entropy was likely the cause for the large discrepancies in the previous study, and that the relationship could be much more applicable than originally presumed. Further experimental and theoretical work in this field is required before determining if there exists a generally-accepted thermodynamic definition of kinetics, but, if there is, it would greatly simplify a number of physical descriptions of glass formation as well as molecular-dynamics simulations. As such, our understanding of the physical nature of glass formation is constantly evolving. This evolution is a strong indicator that bulk-metallic glasses, and glasses in general, have not begun to realize their full potential as engineering materials.

1.5.3   Additional Considerations

In addition to the above discussion, recent experimental investigations suggest the presence of miscibility gaps in the energy landscape of some BMG-forming alloys [20, 21]. These gaps act to destabilize the atoms in solution and could cause the energy barrier for nucleation, ΔG^*, to decrease with undercooling at a rate faster than that predicted by classical nucleation theory. In BMG-forming systems containing a
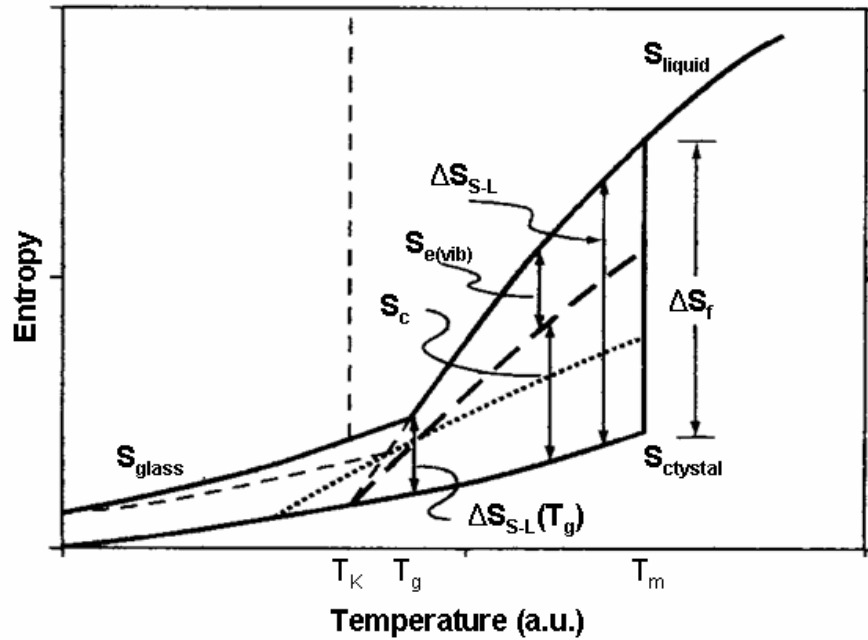
Figure 1.8 A hypotherical plot of the total entropy difference and components as a function of the temperature in the undercooled-liquid state and glass. Note that in this figure, the entropy values were not normalized by $S_{crystal}$. The figure is approximately as it appears in Ref. [19].

miscibility gap, the formation of a glass becomes more reliant on kinetics as liquid-liquid phase separation and, ultimately, crystallization by a spinodal decomposition becomes energetically favorable. In terms of thermodynamics and kinetics, then, the best glass-forming alloys are those that exhibit 1) a low driving force for crystal nucleation, and 2) sluggish kinetics (i.e., high viscosity) in the undercooled-liquid region, particularly in the presence of a miscibility gap. For further experimental and theoretical treatments of the kinetics and thermodynamics of glass formation, the reader is referred to Refs. [14, 16, 22-34].

1.5.2 *"Criteria" for Glass Formation*

Turnbull used the thermodynamic and kinetic factors influencing glass formation to formulate the first measurable parameter that could be used to describe how well an alloy should form a glass. He identified the reduced glass-transition temperature, $T_{rg} = T_g/T_m$, T_m being the melting temperature of the material, as a physical parameter indicative of the glass-forming ability (GFA) of an alloy. Assuming that the viscosity of the material follows the Vogel-Fulcher-Tammann model, and hence, the nucleation rate is proportional to $1/\eta$, nucleation becomes experimentally avoidable in a laboratory setting for $T_{rg} \geq 2/3$. As such, T_{rg} is commonly accepted as the first *criterion* for glass formation

The use of T_{rg} as a predictive measure points toward alloys with low melting points, as T_g cannot be easily predicted. Thus, it seems intuitive that to find good glass-forming alloys, one should probe eutectic compositions, where the crystalline phases are

"less stable" in relation to the supercooled liquid (low ΔG_{S-L}). This criterion is still being used to search for new glass-forming compositions, and has recently been modified by Lu and Liu into the γ parameter [35], where $\gamma = T_x/(T_g + T_m)$, which tends to predict numerical values of the CCR. The utility of the T_{rg} and γ criteria is realized during alloy development, using measured T_g, T_m, and T_x values. The initial efforts at finding BMG-forming compositions relied primarily on empirical approaches, rationalized by thermodynamics and kinetics, and which serve as the basis for current predictive models.

The *confusion principle*, elegantly described by Greer in 1993 [36], is based on the idea that crystalline phases become less stable in relation to a supercooled liquid as its configurational entropy is decreased. An undercooled liquid, therefore, is stabilized by a lack of "open space" on the atomic scale. An effective way of decreasing the configurational entropy in an undercooled liquid (i.e., forming a "more dense" liquid) is to add multiple elemental species of varying sizes. This principle ultimately led Johnson and Peker to develop the Zr-Ti-Cu-Ni-Be system [6, 37] from which a number of useful BMG compositions are derived. A. Inoue identified three empirical rules, based on the observed trends of a number of alloys developed by his group, as guidelines for identifying good glass-forming alloys [38]. These are:

1)   More that three elemental constituents[8].

2)   Different atomic-size ratios (above ~ 12%) among the three primary constituent elements.

3)   Negative enthalpies of mixing between the constituent elements.

---

[8] This remains a useful guideline, however, several binary BMG-forming alloys have recently been discovered.

1.6   Bulk-Metallic-Glass Processing

1.6.1   Practical Considerations

In describing the early stages of the BMG development, Greer described glass-forming alloys as being "diffucult to produce in the first place because they require such high cooling rates, and they show an ungrateful tendency to undo the good work by crystallizing on heating" [36]. The field of BMG-processing has come a long way with respect to identifying better glass-forming alloys, but this quote highlights one inescapable reality: BMGs are in a *nonequilibrium state*. That is, all alloys, to a greater or lesser extent, do not "want" to be in the glassy state when they are cooled from T_m, as it is thermodynamically unfavorable. The good glass-forming alloys are those that allow this condition to be reached because their atoms are sufficiently *lazy*[9] and *slow*[10] in the undercooled-liquid state. The atoms "know" that they should form a crystal but are not in a hurry to do so. BMG-processing methods are designed to take advantage of this sluggish crystallization behavior to quench the materials in their nonequilibrium-undercooled-liquid configurations before they are able to nucleate crystalline phases.

When processing BMG-forming alloys, particularly Fe and Zr based systems, it is important to consider their inherent reactivity in the liquid state. Consider again the classical nucleation theory. In an alloy containing, for example, oxide particles in the superheated-liquid state due to the contamination by air, during cooling from the melt, the thermodynamic energy barrier for nucleation is no longer governed by γ_{sl} as defined

---

[9]   Low thermodynamic driving force for nucleation.
[10] Poor atomic mobility (poor self-diffusion / high viscosity).

above. Assuming that the interfacial-energy difference between the equilibrium crystalline phase and the oxide particle, γ_{so}, is less than γ_{sl}, the undercooled liquid is destabilized in local regions around the particles. This material has a low energy pathway to nucleate crystalline phases using the oxide particles as substrates. This "nucleation catalysis" effect, described by Turnbull and Vonnegut in 1952 [39], occurs when the catalyst and nucleating phase have similar atomic arrangements on low index crystallographic planes (low γ_{so}). In metallurgy, this phenomenon is commonly referred to as *heterogeneous nucleation*. In practice, heterogeneous nucleation can result in the destruction of glass-forming ability in the presence of only several hundred ppm of oxygen, as shown experimentally by Lin et al. in a Zr-based BMG-forming alloy [7]. This phenomenon could be a large liability in an industrial setting, as very pure elemental-charge materials must be used and environmental control must be carefully maintained, driving up product costs.

Some of the best glass-forming alloys exhibit a degree of stability against heterogeneous nucleation, particularly from oxygen contamination, due to a large relative structural dissimilarity between impurity oxides and stable phases. Furthermore, as illustrated in a review article by Lu and Liu [40], microalloying with certain elements or combinations of elements can overcome the problem of contamination. They go on to describe the mode of operation of microalloying strategies to enhance GFA in contaminated-BMG-forming alloys as: a) reacting with the contaminant in the superheated solution to form anticatalyst particles that are benign to heterogeneous nucleation (large γ_{so}), or b) increasing ΔG^*, by either migrating to particle/liquid interfaces and raising γ_{so}, or stabilizing the glass directly, vis a' vis the *confusion*

principle. Rare-earth elements, in particular Y and Sc, are useful for eliminating the detrimental effects of oxygen in Fe-based (doped with Y) [41] and Zr-based (doped with Y or Sc) [42, 43] BMG-forming alloys.

1.6.2 Methodology

There are multitudes of processing methods to prepare BMGs resulting from the past 20+ years of research. Many of these methods are suited to quickly finding glass-forming compositions and/or probing BMG thermal properties. A particularly useful method for the production of BMGs from the melt, on the laboratory or industrial scale, is arc-melting elemental constituents into an ingot and, subsequently, casting the molten ingot (using gravity or vacuum pressure) into water-cooled tooling. Examples of drop and suction-cast Zr-based BMGs of differing geometries are shown in Fig. 1.9. Drop and suction-casting equipment can be made by modifying a commercially-available arc-melter, similar to that shown in Fig. 1.10. A description of the design of such a device can be found in Ref. [44], and will be presented in Chapter 3. One difficulty that arises in arc-melting ingots is the incomplete melting of refractory elemental species. Fan et al. showed how this difficulty may be overcome by employing an intelligent selection of melting sequences to encourage the homogeneous mixing [45]. Additional quench-casting methods employ inductive heating of the alloy, which has the added effect of agitating the superheated-liquid alloy due to alternating current (AC) magnetic fields.
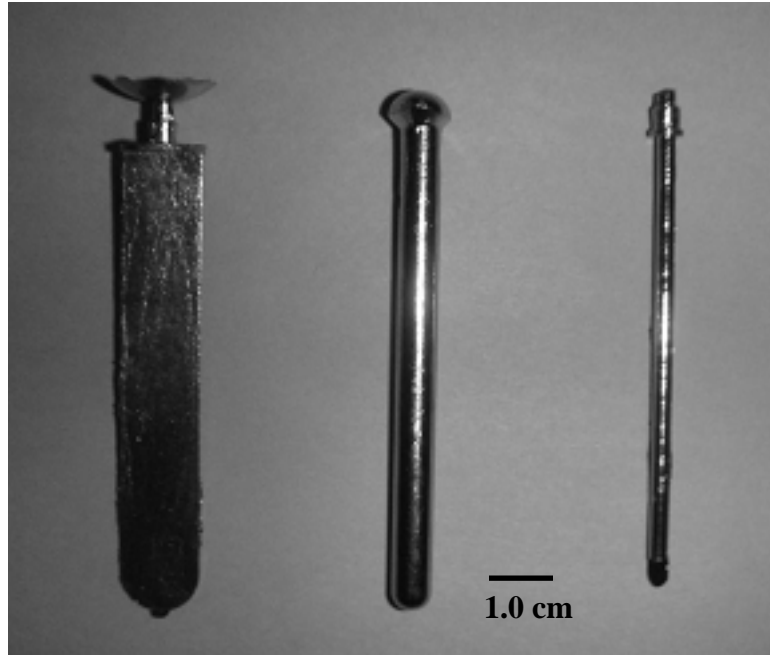
Figure 1.9 Suction-cast (left and right) and drop-cast (center) samples of $Zr_{52.5}Cu_{17.9}Ni_{14.6}Al_{10}Ti_5$ BMG.
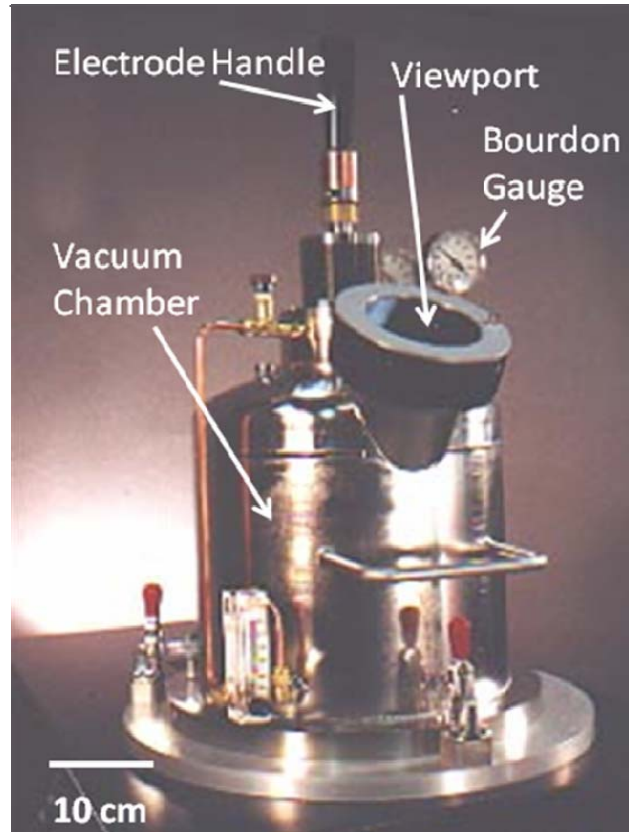
Figure 1.10   A picture of a Materials Research Furnaces model ABJ-900
arc-melting furnace.

BMGs have a unique ability to resist crystallization in the superheated-liquid state, allowing them to be shaped by superplastic-forming methods when reheating above T_g ($< T_x$). An example of this ability is the so-called *amorphous metallic plastic* [46], which is a Ce-based BMG that can be shaped in near-boiling water. A difficulty that arises with respect to forming by homogeneous flow is that all BMGs have finite stability when reheated to the supercooled-liquid region and will start to nucleate crystals if held there for a long period[11], as demonstrated by Kim et al. [47] . This consequence of heating would be particularly troublesome in the presence of a miscibility gap. Furthermore, strain-intensive methods, such as warm extrusion or forging, could cause dynamic heating to $T > T_x$, resulting in massive crystallization due to localized high strain rates. There is likely room for improvement in the area of manufacturing BMGs, particularly in the improvement of rapid heating / cooling technologies to accommodate their fickleness in the supercooled-liquid state.

---

[11] This phenomenon is used to intentionally nucleate crystalline precipitates in a BMG, creating so-called glassy matrix composites.

Chapter 2: Experimental Methods

The experimental techniques used in this research can be classified as either *processing* or *analysis* techniques. As stated in the introduction, in the present chapter, only the *analysis* techniques are treated. As this research project was focused heavily on processing, the individual processing components are elaborated upon in greater detail in the subsequent chapters.

2.1   Laboratory X-Ray Diffraction

This technique is commonly used to confirm the absence of crystallites in BMGs, or identify those present in, e.g., a glassy matrix-compoiste. Crystalline species in a material diffract incident radiation in a specific geometry, which may be predicted by the nature of their crystal structures. Diffraction peaks can be used to identify unit-cell geometries, which indicates the phases present in a material, by invoking Bragg's Law:

$$\lambda = 2d\sin(\theta) \tag{2-1}$$

where λ is the x-ray wavelength, which is usually constant, d is the interplanar spacing between (hkl) planes in the lattice, and θ is the scattering-vector angle. A simple illustration of this concept is shown in Fig. 2.1.
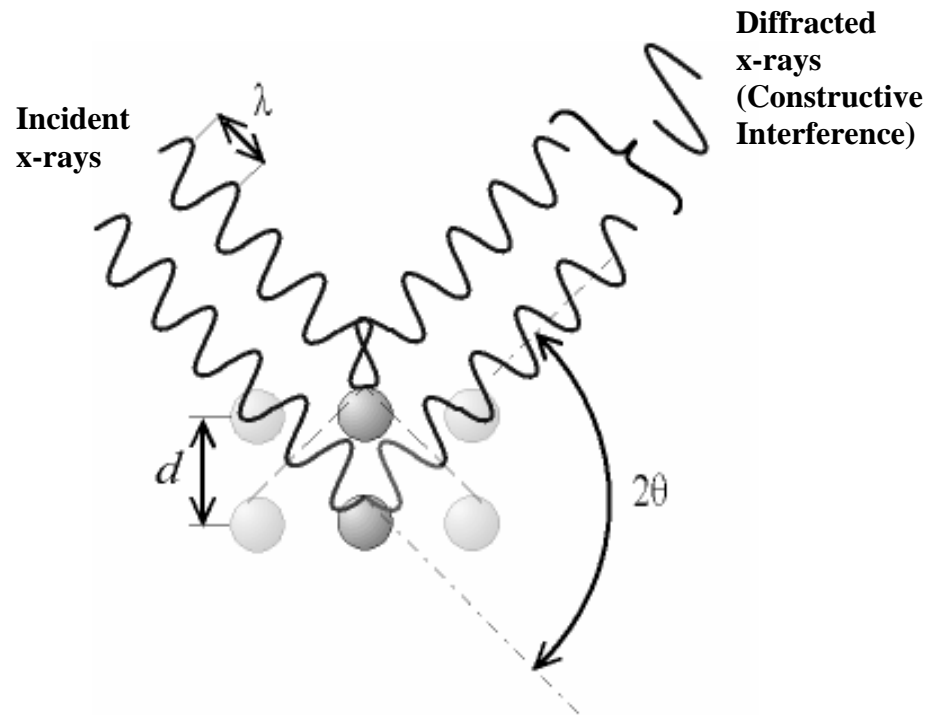
Figure 2.1   The geometry of diffraction in a crystal lattice. The conditions are satisfied for constructive interference, resulting in an intensity spike in the *I(2θ)* x-ray diffraction (XRD) spectrum, where *I* denotes intensity.

BMG materials, which contain no crystalline species, do not diffract the incident radiation into sharp peaks but, rather, into broad, "diffuse" humps in the *I(2θ)* spectra. These "humps" are characteristic of the local to medium range order of the glass. The laboratory XRD analyses described herein were performed using the wide-angle x-ray diffractometer in the diffraction laboratory of the University of Tennessee (UT) Materials Science and Engineering (MSE) Dept. (Phillips X-Pert, CuK_α).

2.2   Differential-Scanning Calorimetry

Differential scanning calorimertry (DSC) is commonly used to measure the thermal properties of BMG materials after processing. The calorimeter operates by heating a sample at a predetermined rate with a known quantity of the input energy and, subsequently, measuring the temperature response of the sample. Using the measured data, the differentials in the thermal response can be used to very accurately observe both endothermic and exothermic reactions in the sample as a function of the temperature and heating rate, *dT/dt*. The measured data allow the direct characterization of the glass-transition temperature, T_g, and crystallization temperature, T_x, in a sample. In addition, using this data, one can calculate the specific heat evolution, $c_p(T)$, and the enthalpy change, *ΔH*, during a reaction, using

$$\Delta H = m \int_{T_1}^{T_2} c_p \, dt \qquad\qquad (2\text{-}2)$$

where T_1 and T_2 are the onset and completion temperatures of the reaction, respectively and m is the sample mass. The DSC measurements for this research were performed using the calorimeter in the UT International Materials Institutes (IMI) laboratory (Perkin-Elmer Diamond DSC), Fig. 2.2.

2.3   Scanning-Electron Microscopy

Scanning-electron microscopy (SEM) is a versatile tool commonly used for microstructural analyses. Imaging techniques using secondary electrons (with a good spatial resolution) and backscattered electrons (sensitive to the atomic number, allowing Z-contrast imaging) were used for micostructural-characterization studies. These studies were performed using the facilities available at the UT electron-microscopy laboratory. Two microscopes were used: a field-emission SEM, equipped with a secondary-electron detector, and a thermionic SEM, equipped with a backscattered-electron detector.

2.4   Energy-Dispersive X-ray Spectroscopy

Energy-dispersive x-ray spectroscopy (EDS) is a spectroscopic method that is often coupled with an electron microscope fitted with an x-ray detector. The electron beam used for imaging excites x-rays of the characteristic energies specific to the atoms in the beam/sample interaction volume. These characteristic x-rays are produced when an electron, previously excited into an inner orbital of an atom, returns to its ground state on an outer orbital, releasing the energy difference as a photon.
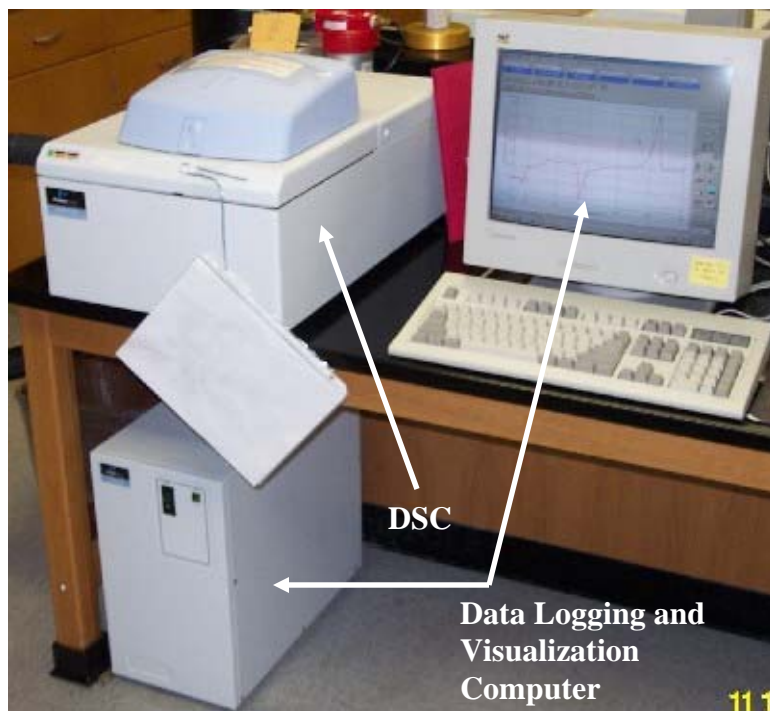
Figure 2.2 A photograph of a Perkin-Elmer Diamond differential-scanning calorimeter and data acquisition and analysis computer.

The excitation of characteristic photons allows a spectroscopic analysis of the elements that make up the electron-beam/sample interaction volume. Interfacing with EDS software allows the reproduction of multiple interaction volumes into 1-D and 2-D composition maps of a region of interest. The field-emission SEM mentioned in the previous section has this capability and was used to conduct spectroscopic analyses.

2.5 Universal-Testing Machine

Mechanical tests were done using a universal testing machine (MTS-810) under quasistatic loading conditions in compression, Fig. 2.3. The strain was measured using an MTS knife-edge strain gauge affixed to the samples (6.4-mm-diameter x 10-mm-length cylinders). The applied load was measured using a MTS load cell. The piston displacement was measured by a linear-variable-displacement transducer (LVDT). A commercially available data-acquisition software was used to log the extrinsic variables as a function of time. Analyses of the data sets were conducted to determine the compressive rupture strengths of the samples. The universal testing machine used for these experiments resides in the MSE materials-testing laboratory.

2.6 Wet-Chemical Analyses

Volume-averaged spectroscopic analyses were performed to determine the oxygen content of several BMG materials produced in this research. These analyses were

Figure 2.3 Photograph of an MTS series 810 servohydraulic universal-testing machine fitted with hydraulic sample grips.

performed with the inductively-coupled plasma / optical-emission-spectroscopy technique, commonly referred to as "wet chemical analyses". In this method, the sample is converted to a liquid form for analyses using various combinations of concentrated acids or bases and subsequent heating. The sample (in an aerosol form) is directed through the center of an argon-plasma torch. The energy of the plasma causes the sample atoms or ions to jump to their inner-shell orbitals. As the excited atoms and ions relax to their base states, they emit characteristic x-rays. The x-rays are focused onto a solid-state detector, which identifies each wavelength and its relative intensity. The $I(\lambda)$ spectrum is analyzed to find the intensity at the characteristic wavelength of the desired element. This information is, then, compared to calibration data for quantification. The wet-chemical analyses were conducted at Shiva Technologies, Inc., which is an internationally recognized leader in performing chemical analyses using a variety of methods, including the inductively-coupled plasma / optical emission spectroscopy technique.

2.7   Electrostatic-Levitation

Electrostatic-levitation (ESL) uses a large electrical-potential difference (up to 15 kV) between two vertically-mounted electrodes (top and bottom) to counteract the effect of gravity, effectively suspending a spherical sample in 3-D space in a high-vacuum chamber. The sample must be charged in order to realize the effect of the field. As such, an ultraviolet lamp is used to eject electrons from the sample during levitation. The sample is heated by a tetrahedral-laser-heating system and cooled by turning off the

heating laser, resulting in radiative heat transfer, which can be modeled by rearranging

Boltzmann's Law:

$$\frac{dT}{dt} = \frac{-3\sigma\varepsilon(T_s^4 - T_{inf}^4)}{C\rho r}$$

(2-3)

where r is the sample-sphere radius, σ is the Stefan-Boltzmann constant, ε is the sample

emissivity, T_s is the sample temperature, T_{inf} is the continuum temperature, C is the heat

capacity, and ρ is the density. Sample temperatures can be monitored using a two-

wavelength optical pyrometer, and high-resolution charge-coupled device (CCD) images

can be captured in-situ. The evolution of the sample specific-volume can be computed

by fitting the sample peripheries in the CCD images with LeGendre polynomials,

assuming that the sample is axisymmetric. Several images of the NASA Marshall Space

Flight Center electrostatic-levitator are presented in Fig. 2.4

Electrostatic-levitation provides a containerless environment in which to study the

thermophysical properties of materials during undercooling. This technique creates an

ideal environment to study oxygen-induced nucleation, since the absence of all physical

contact with the specimen removes the capacity of the material to heterogeneously

nucleate crystalline phases due to external factors, such as surface flaws in a mold wall.

This technique was used to characterize the effect of the oxygen contamination on the

free-cooling temperature profiles and corresponding specific-volume profiles of BMG

samples. These measurements were performed using the electrostatic-levitation facility

of the microgravity laboratory at the California Institute of Technology [48].
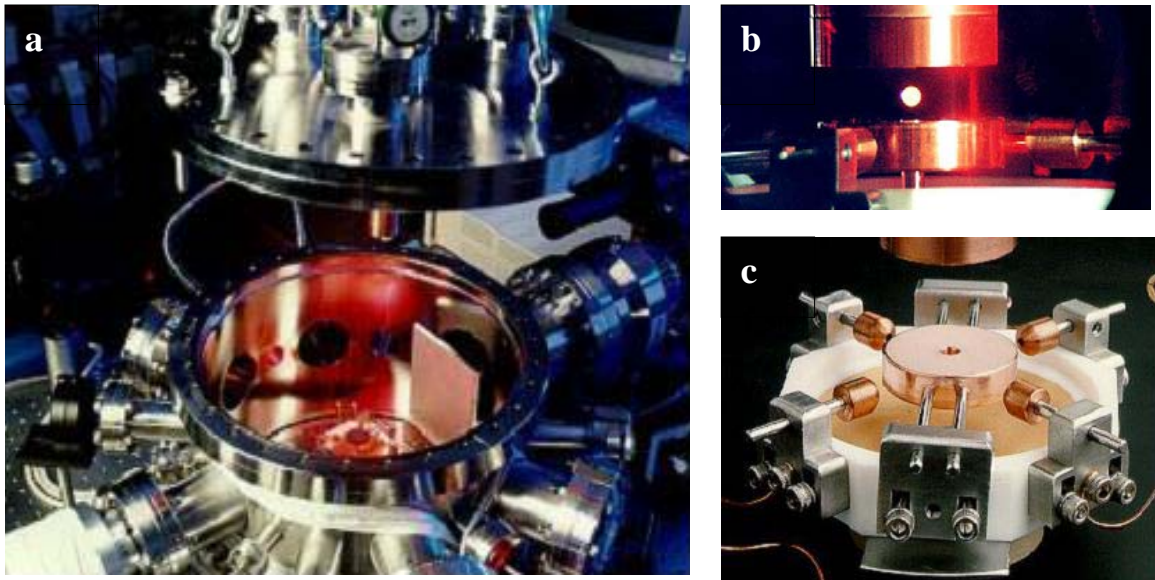
Figure 2.4   Photographs of the NASA Marshall Space Flight Center electrostatic-levitator.   a) is the bottom electrode of the levitator sitting in an ultra-high vacuum vessel.   The top electrode (hidden from the view) is fixed to the lid of the vessel, shown in the upper part of the image, b) is a sample (superheated liquid) suspended between the electrodes, and c) is the bottom electrode removed from the vacuum vessel. Note that the side electrodes, seen in image "c", control the sample position in the horizontal plane.

2.8　Synchrotron X-ray and Neutron Scattering

Synchrotron x-rays are high-energy photons generated at an electron accelerator by changing the direction of the wave vector of a pulse of electrons moving at close to the speed of light. The photons are generated using magnets (bending magnets or undulators) situated along the accelerator. The high-energy x-rays are, then, used for experimental investigations. The use of high energy (> 50 keV) x-rays allows probing of an appreciable volume of material (~ 2 mm in depth) with a relatively high atomic number. This characteristic is in contrast to x-rays produced by portable sources, which are limited in depth to tens of microns.

Synchrotron x-ray scattering (SXRS) studies were performed at the Advanced Photon Source of the Argonne National Laboratory, on beam line 1-ID (XOR-CAT) and beam line 11-ID (µ-CAT). The measurements were made in a transmission geometry using 80-115 keV x-rays detected by a 2-D image plate. The scattering data (2-D Debye patterns) were integrated into $I(2\theta)$ spectra.

Neutron scattering is a powerful tool for a multitude of materials-characterization studies. Neutrons, like laboratory and synchrotron x-rays, scatter from periodic structures in a geometry described by Bragg's Law. However, neutrons are not scattered by electrons in an atom, but rather only the atomic nuclei. This attribute results in their characteristic large penetration depths[12] and coherent scattering cross sections, σ_C, which vary irregularly with the atomic number. As such, when neutron scattering is used for comparison with x-ray-scattering data, the differences in relative intensities of the Bragg-

---

[12] Note that some elements, such as gadolinium, cadmium, and, to a lesser extent, boron, strongly absorb neutrons. In materials containing these elements, the penetration depth of thermal neutrons can be very small.

diffraction peaks can reveal the information about the site occupations in the structure of a polycrystalline sample. Neutron-scattering measurements were performed under ambient conditions using the General Purpose Powder Diffractometer (GPPD) at the Argonne National Laboratory, Argonne, IL. These facilities are time-of-flight neutron sources, meaning that the entire scattering patterns were collected using polychromatic radiation, the energy spectrum of which was determined by the neutron time of flight (TOF), allowing the conversion of the intensity energy spectrum $I(TOF)_{2\theta}$, to $I(d)$.

2.8.1   Scattering Data Analyses

The Rietveld method [49] was used to fit the diffraction data in the form of the $I(2\theta)$ spectra. The Rietveld method fits multiple peaks in a diffraction pattern by applying a profile function, which models the characteristic peak shape, and calculating a pattern from an input starting-structure. Applying Bragg's law (Eq. 2-1), the diffraction pattern of a crystalline phase may be simulated using:

$$I(2\theta)_{calc} = b(2\theta) + \sum_{i} I_i P_i (2\theta) \qquad (2\text{-}4)$$

where the subscript, $"i"$, refers to the ith Bragg reflection, b is the background function, P_i is the peak-profile function, and I_i is the theoretical integrated-intensity, which is a function of the structure factor, $S(Q)$, that represents the calculated intensity contribution of each hkl plane. For monochromatic synchrotron x-rays, a Bragg-peak profile, $P(2\theta)$,

can usually be modeled, using a multi-term Simpson's Rule integration[13] of the pseudo-Voigt function, $I_P(2\theta)$, where:

$$I_P(2\theta) = \omega \frac{2}{\Gamma\pi}\left[1+4\frac{(\Delta\theta)^2}{\Gamma^2}\right]^{-1} + (1-\omega)\frac{2}{\Gamma}\sqrt{\frac{\ln 2}{\pi}} \cdot \exp\left[-4\ln 2\frac{(\Delta\theta^2)}{\Gamma^2}\right] \qquad (2\text{-}5)$$

and:

$$H(2\theta) = \sum_{i=1}^{n} g_i I_P(2\theta) \qquad (2\text{-}6)$$

where Γ is the peak full width at half maximum (FWHM), ω is the mixing factor (defines partitions of the Gaussian and Lorentzian profile components). Note that in Eq. 11, g_i refers to the ith-component trigonometric function, the sum of which is used to model the peak asymmetry. The calculated pattern, $I(2\theta)_{calc}$, is fitted to the measured pattern using multiple least-squares refinements of dependant variables.

Rietveld fitting of the Bragg diffraction peaks was done using the General Structure Analysis System (GSAS) program. Fitting of the broad "amorphous" scattering peaks from the glass was done using GSAS in conjunction with a fitting technique developed specifically for this research. This technique is described in detail in Chapter 7 and Appendix B.

---

[13] A derivation can be found in Ref. [45]

Chapter 3: A Combined Drop / Suction Casting Machine for the Manufacture of Bulk-Metallic-Glass Materials

Foreword

The current chapter catalogues the development of the processing machinery used to produce bulk-metallic glasses. The proceeding is an incarnation of the formal research record, which was published in the peer-reviewed journal *Review of Scientific Instruments*, as shown below. The article has been lightly revised for the sake of the continuity of this dissertation.

Wall, J. J., Fan, C., Liaw, P. K., Liu, C. T., and Choo, H., "A Combined Drop / Suction Casting Machine for the Manufacture of Bulk-Metallic Glass Materials," *Rev. Sci. Instr.* **77,** 033902 (2006): Reference [44].

3.1   Introduction

Bulk-metallic glass (BMG) materials are a new class of structural materials that exhibit non-typical properties as compared with other metal alloys [50]. As their name suggests, BMGs are "glassy" metal alloys, which exhibit noncrystalline, amorphous structures. For this reason, BMGs are currently of significant interest in the field of condensed matter physics in an effort to bring a greater understanding to the nature of glass and the glass transition in metals, currently a largely unresolved problem [51, 52]. Due to their inherent absence of slip planes, the materials exhibit very high yield strengths (1 - 5 GPa) and elastic limits (~ 2%) [53], as well as demonstrate good fatigue-

endurance limits [54]. Also, BMG composites with crystalline inclusions in a glassy matrix are showing promise in enhancing the ductility of the materials while retaining their high strengths [55]. Furthermore, the materials can be cast into high-precision net shapes [56]. Due to their unique processing capabilities and high strengths, BMG materials are of great interest to the industrial community and have the potential to be used extensively in the aerospace and transportation industries in the future. In order to effectively design and test new BMGs with enhanced properties, it is critical to develop the capability to process them on the laboratory scale, in a timely and efficient manner.

Arc melting / drop casting as well as arc melting / suction casting are established processing technologies that have been developed in various laboratories in the past [57-59]. Drop casting is typically used to process materials with diameters larger than 6 mm, while suction casting is used for casting of materials in diameters under 6 mm (where the viscosity of the molten alloy hinders its flow into the mold). More recently, modified designs, such as that presented in [60], with rapid-quenching capabilities, have been developed in various laboratories to fabricate bulk amorphous alloys for subsequent analyses. The goal of this project was to combine and optimize these technologies to create an integrated drop and suction-casting machine, which may be used to quickly and efficiently fabricate BMG monoliths in various sizes and geometries.

3.2   Design Methodology

The first technological hurdle that hinders the casting of BMG materials into shapes suitable for laboratory analyses is that processing must be done in a very pure environment. Oxygen concentrations of several hundred atomic ppm can destabilize the amorphous structure and cause recalescence during cooling from the molten liquid state [7]. The second challenge for the production of BMGs is that in order to facilitate adequately sluggish crystallization kinetics of an alloy during processing from the melt, a condition that enables the retention of the amorphous (liquid) structure, the molten alloy must be quenched relatively quickly (typically $> 10^2$ K/s). The method chosen to accomplish this process is casting in an ultra-pure environment using arc melting, followed by the transfer of the molten liquid into water-cooled electrical-grade copper tooling. The choice of copper as tooling serves dual purposes. As a material that exhibits very good electrical conductivity, it is an ideal anode for the arc-melting process. Furthermore, copper is a very good conductor of heat, which will enable very fast cooling rates, facilitating the rapid vitrification of the alloy melts into amorphous monoliths.

The design of the metallic-glass-casting system was done to be retrofitted to an existing arc melter (Materials Research Furnaces ABJ-900), and proceeded on three fronts: (1) the modification of the existing arc-melter design to redefine the geometrical constraints, (2) the design of copper tooling to satisfy the geometrical, mechanical, and electrical constraints, and (3) the redesign of the vacuum system to provide a split chamber vacuum plus toggle-independent secondary vacuum ballast for suction casting. Furthermore, as the current drop-casting unit designs are relatively simple, suction-

casting units tend to be more complex and require more operator time and effort to complete a process. As such, the overall goal of the current design was to satisfy processing requirements with minimal user-complexity, fast turnover, and accessibility.

3.3 Design Description

3.3.1 Water-cooled-hearth design

A half-section three-dimensional (3-D) model of the hearth tooling is shown in Figure 3.1. The hearth sits under a vacuum bell and acts as the anode for the arc-current transfer by the cathode during arc melting under an Ar cover. An outer steel flange (a) was attached to the furnace-base plate to allow the placement of the tooling below the existing base while maintaining the vacuum integrity. A water-cooled, oxygen-free Cu hearth (b), of an approximate diameter of 250 mm, with a tapered sleeve, was fabricated and fixed to the furnace base under the (hinged) vacuum bell. The hearth consists of two components (b1 & b2) fixed at the outer by bolts patterned outside an o-ring and fixed at the inner by a hollow screw (c) with 2 o-ring seals on the underside to interface the bolt with b1 and b2. O-rings were placed around the hearth-water inlet and outlet to isolate the chamber from the outside environment (d). An electrical connection with the power supply was made via the outlet water tube of the hearth (e). The vacuum was pulled from a reducing flange (f) that was attached to the outer steel flange (a).
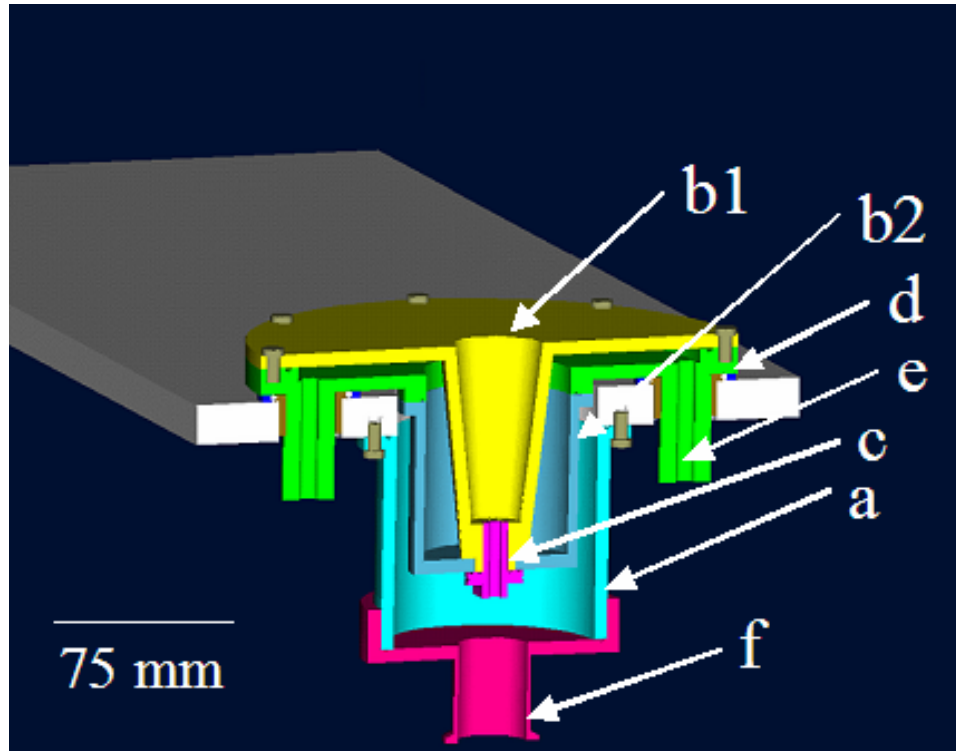
Figure 3.1   A half-section 3-dimensional model of the water-cooled Cu hearth; a is an extension flange, b1 is the hearth upper component, b2 is the hearth lower component, c is the hollow interface screw, d is the hearth / base plate o-ring seal, e is the water outlet tube, and f is the vacuum flange.

3.3.2 Tooling design

Three types of tooling were designed to interface with the hearth, as shown in Figure 3.2, including: an alloying crucible (a), in which elemental raw materials are combined to form an alloy of a predetermined composition, a 2-piece split-die (b) for drop casting, and a 4-piece split die (c) for suction casting. All tooling was tapered along the outer surface to seat to the taper angle of the water-cooled Cu hearth. The 4-piece suction-casting die was sized to seat in the hearth, leaving a 0.15-mm gap between the upper (crucible) portion and lower (mold) portion. The die was split to minimize the heat flow into the mold. The split-die is shown, as inserted into the hearth, in Figure 3.3.

3.3.3 Vacuum-system design

The vacuum system was designed to consist of 3 toggle-independent systems, utilizing one vacuum pump, which can work in sequence or independently. The systems include; (1) a sub-furnace system (main), which generates a vacuum below the water-cooled hearth within the outer flange (Fig 3.1, a). Two auxiliary systems are coupled to the main one via pneumatically-actuated-gate valves; (2) the arc-furnace bell, which controls the vacuum for the arc-furnace chamber above the water-cooled hearth; and (3) A 5-gallon ballast tank used to generate an impulse pressure drop in the sub-furnace system, which is, subsequently, utilized for suction casting by creating a pressure difference between the sub-furnace system and the furnace chamber (i.e., between the top and bottom of the casting mold). A simplified vacuum diagram is shown in Figure 3.4.
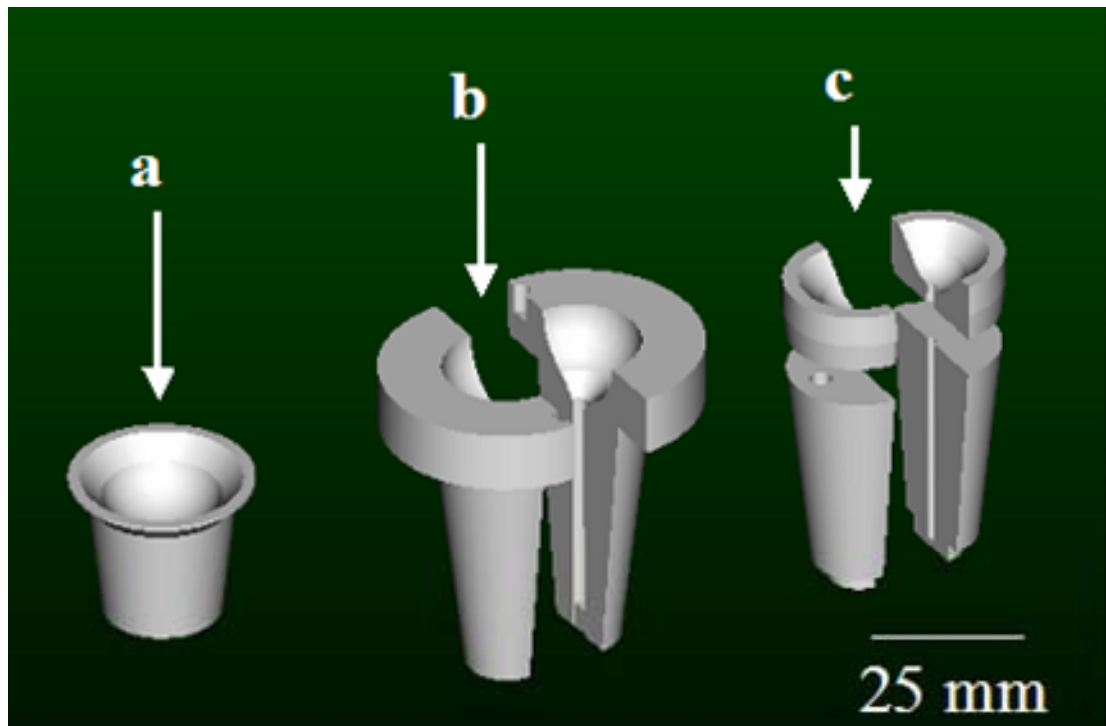
Figure 3.2 Tooling 3-D models: (a) is the alloying crucible, (b) is the 2-piece drop-casting split-die (exploded representation), and (c) is the 4-piece suction-casting split-die (exploded representation).
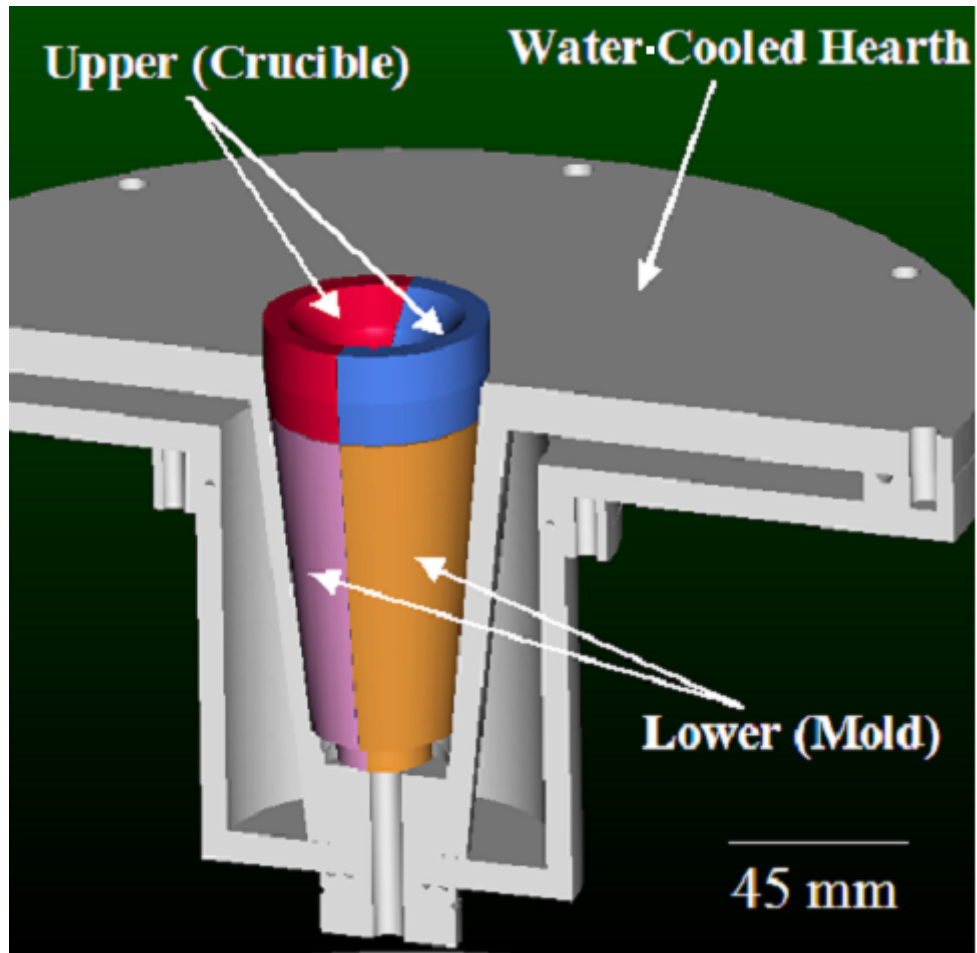
Figure 3.3 Assembly model of the 4-piece-suction-casting die inserted into the water-cooled Cu hearth (a half-section model of hearth is shown for clarity).
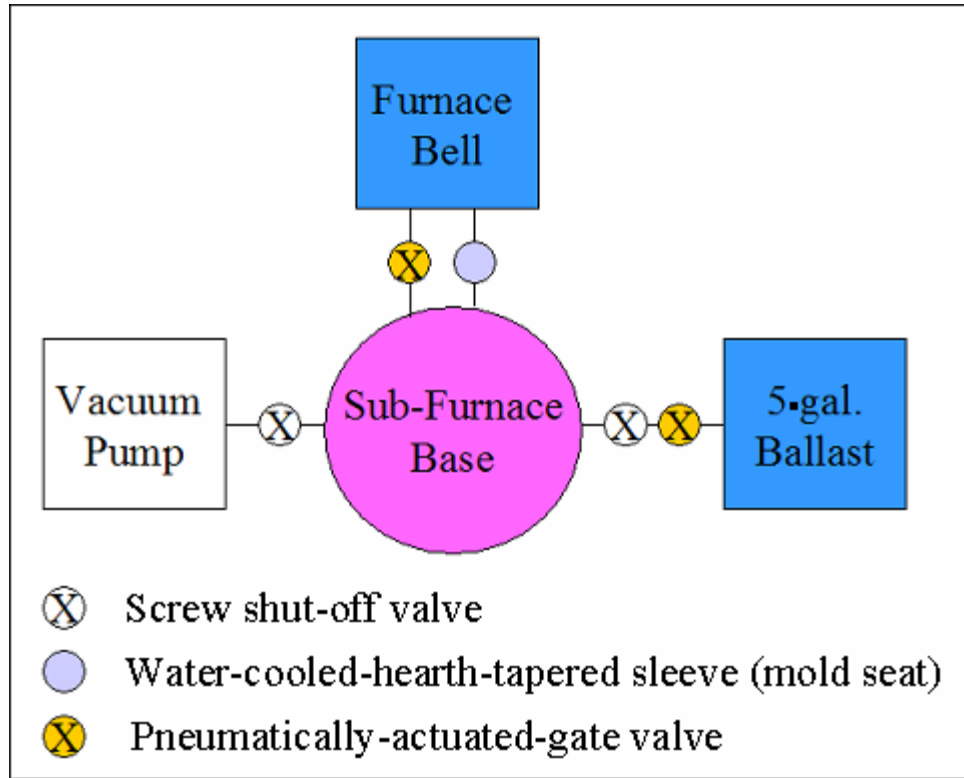
Figure 3.4   A simplified vacuum diagram showing the 3 toggle-independent vacuum systems.

3.4   System Operation

A process and instrumentation diagram for the system can be seen in Figure 3.5. The operation of the unit during alloy mixing in the crucible is relatively straightforward. The operator closes the screw valve linking the sub-furnace chamber and the ballast tank, and opens the pneumatic-gate valve (via an on-off switch) connecting the furnace bell and sub-furnace chamber. A vacuum is pulled on the two active systems, and the vacuum pump is, subsequently, isolated by a screw valve. The furnace bell and sub-furnace chamber are, then, back-filled with ultra-high purity (UHP) Ar, and arc melting proceeds, allowing alloying of the elemental raw materials. The same vacuum setup described above is used during drop casting. By replacing the Cu-alloying crucible with a 2-piece Cu drop-casting split mold, and melting an alloy charge in the arc-furnace, the alloy will drop into the mold via gravity and rapidly cool. The casting may, then, be removed, and the process repeated. Suction casting (using the 4-part-split die) proceeds by opening both the screw valve and pneumatic-gate valve linking the ballast tank and sub-furnace chamber. Likewise, the pneumatic-gate valve linking the sub-furnace chamber and furnace bell is opened. The entire system is, subsequently, evacuated. Under vacuum, the pneumatic-gate valve linking the ballast tank and sub-furnace chamber is closed. Then, the remaining linked system (the sub-furnace chamber and furnace bell) is back-filled with UHP Ar, and the alloy ingot is melted on the crucible portion (upper portion) of the suction-casting-split die. When the ingot is molten, the operator closes the pneumatic-gate valve connecting the furnace bell and sub-furnace
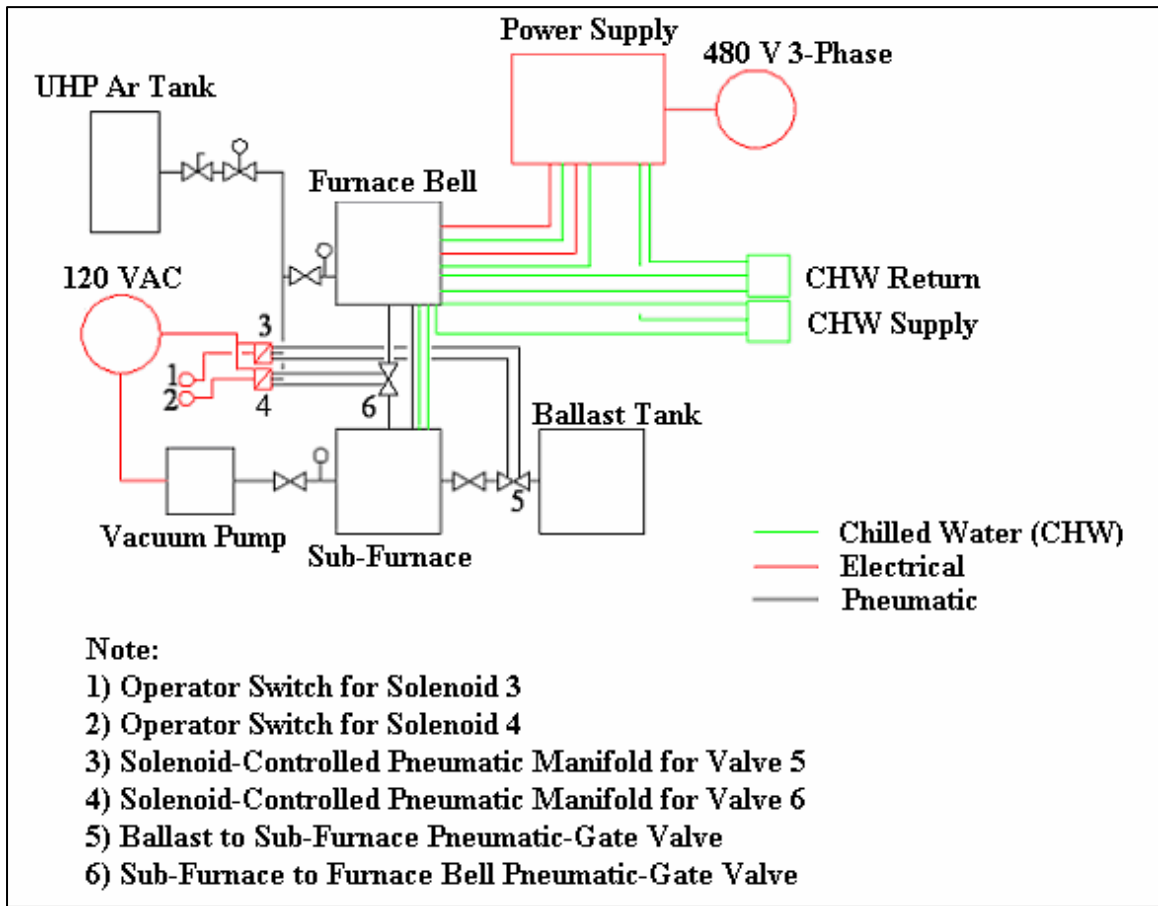
Figure 3.5   Drop/suction casting-system process and instrumentation diagram.

base, effectively isolating the two systems, and, then, immediately opens the pneumatic-gate valve linking the sub-furnace base and ballast tank. As the ballast tank was previously under vacuum, opening the valve generates an impulse pressure drop in the sub-furnace chamber that is not realized within the furnace bell. The pressure difference acts to pull the molten material into the split die where it rapidly cools (as the only path to equilibrate the pressures is through the mold). The casting is, then, removed, and the process may be repeated.

3.5   Results

Castings of Vitreloy 105 ($Zr_{52.5}Cu_{17.9}Ni_{14.6}Al_{10}Ti_5$, in atomic percent, at.%) were done in 3 geometries, drop-cast 6.4 mm x ~ 70 mm cylinders, suction-cast 3 mm diameter x ~ 70 mm cylinders and suction-cast 12 mm x 1 mm x ~ 70 mm plates, shown previously in Figure 1.9. X-ray diffraction (XRD) was performed on the as-cast specimens using a Phillips X-Pert diffractometer with CuK_α radiation, with a potential of 45 kV, and a current of 40 mA. The XRD spectra from a representative sample of each geometry are shown in Figure 3.6. In each case, a broad diffuse peak, typical of an amorphous Vitreloy 105, was seen, confirming that the as-cast samples did indeed vitrify during the casting process.
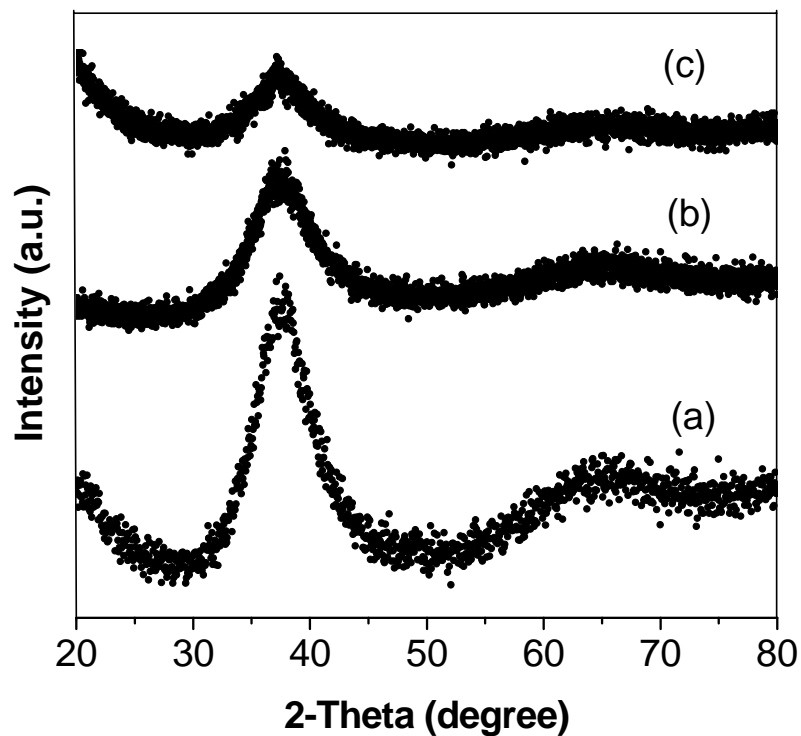
Figure 3.6   X-ray diffraction spectra from Vitrelloy-105; (a) drop-cast 6.4-mm diameter x ~ 70-mm-length rod, (b) suction-cast 1-mm x 12-mm x ~70-mm plate, and (c) suction-cast 3-mm diameter x ~ 70-mm length rod. All spectra show that the as-processed samples had a basic lack of any periodic crystal structure.

3.6   Discussion

The design of the water-cooled-Cu hearth was found to offer very fast changeover times of only a few minutes. The casting tooling sits in the tapered sleeve of the hearth, allowing all tooling to be removed through the top of the furnace base. As such, castings could be done, and new alloy charges loaded very quickly with very little user manipulation. This is a significant improvement over systems in which the casting tooling sits in a separate vacuum chamber from the furnace chamber and must be removed separately from the crucible. At the time of this writing, it has been demonstrated that BMGs of 3 different geometries have been successfully fabricated using the current machine design. It is expected that different and more complex casting geometries will be easily accommodated by additional split-mold designs.

Chapter 4: Aerodynamic-Levitation Processing of a Zr-Based Bulk-Metallic Glass

Foreword

The current chapter describes a set of experiments used as a "proof of concept" to confirm the utility of a novel method to process bulk-metallic glasses. This research has been published in the peer-reviewed journal *Materials Science & Engineering A*, as shown below, and has been revised slightly to fit within the context of this dissertation.

4.1 Introduction

Containerless methods have been used to study materials properties in undercooled alloys with a great deal of success [62-68]. The elimination of all contact points with the specimen effectively removes the extrinsic, low-energy, heterogeneous-nucleation pathways from an undercooled-alloy melt. Crystallization may proceed by homogeneous nucleation (assuming that the liquid is free of inoculants) following the criteria outlined by Turnbull [69]. Kim et al. [70] pioneered the application of electrostatic-levitation (ESL) [48] in an ultrahigh vacuum environment to process a bulk-metallic glass, $Zr_{41.2}Ti_{13.8}Cu_{12.5}Ni_{10}Be_{22.5}$ (Vit-1), using a Xe arc-lamp to heat a electrostatically-levitated specimen and, then, subsequently free-cooling at a rate that

bypasses crystallization. Further ESL investigations have focused on the measurements of the time-temperature-transformation (TTT) curves of bulk-metallic glasses [62, 71] as well as measurements of their thermophysical properties [22, 72, 73]. However, the use of ESL to study the vitrification behavior of BMG-forming-alloy spheres is limited due to the exponential decay nature of radiative cooling, as described in Chapter 2. It is apparent from Boltzmann's Law that due to the 4th-order relationship between the sample temperature and radiative emission, the cooling rate, dT/dt, due to the purely radiative heat transfer decreases quite rapidly during cooling as a function of the sample temperature, as can be seen in Eq. (2-3).

Aerodynamic levitation (AL) is an established containerless method for studying the liquid state of oxides [74] and reactive metals [75] as well as the production of rare-earth-aluminum-oxide (REAl™) glasses [76]. The process uses a specially-shaped nozzle to suspend a sphere of a material in a jet of gas. A laser is used to heat the levitated specimen. In a typical processing experiment, the specimen is taken beyond its melting temperature to a soak temperature (T_o), where it exists as a sphere of the levitated liquid. The specimen is, then, cooled at a predetermined rate, which is controlled by reducing the incident heating-laser power. By the nature of the levitation process, the specimen loses heat by both radiation and convection, giving a cooling-limit profile described by the approximation:

$$\frac{dT}{dt} = -\frac{3}{C\rho r}\left[\sigma\varepsilon(T_s^4 - T_{\text{inf}}^4) + h(T_s - T_f)\right] \tag{4-1}$$

where σ is the Stefan-Boltzmann constant and h is the convective-heat-transfer coefficient for the fluid flow past a sphere, described by Whittaker [77] as:

$$\text{Nu} = 2 + \left[0.4\,\text{Re}^{1/2} + 0.06\,\text{Re}^{2/3} \right] \text{Pr}^{0.4} \left(\frac{\mu}{\mu_s} \right)^{1/4} = \frac{2rh}{\alpha} \qquad (4\text{-}2)$$

where Nu is the Nusselt number, Re is the Reynolds number, Pr is the Prandtl number, α is the thermal conductivity of the fluid, and μ and μ_s are the levitating-fluid viscosities in the bulk and at the surface, respectively. As Nu, for this case, is approximately 8 orders of magnitude higher than σ (5.67 x 10^{-8} $\text{Js}^{-1}\text{m}^{-1}\text{K}^{-4}$), it becomes apparent that the convective component begins to dominate dT/dt below $\sim$ 1,200°C in clean-metallic samples (emissivity, $\varepsilon \sim$ 0.2). The convection component in Eq. (4-1) facilitates containerless processing at comparatively fast cooling rates (e.g., $dT/dt \sim$ 70 K/s at $T =$ 800ºC for the current study) as compared to ESL. The higher physical limit of the cooling rate afforded by aerodynamic levitation allows the linear control of the specimen-cooling profile, throughout the supercooled-liquid region and at relatively fast cooling rates. As such, AL processing is well suited for the characterization of BMG materials near their respective critical-cooling rates. A schematic of the aerodynamic levitator is shown in Fig. 4.1.

This chapter presents the data from AL-processing experiments performed on a Zr-based-glass-forming alloy, $Zr_{57}Ti_5Ni_8Cu_{20}Al_{10}$ [78], processed at cooling rates from 1.2 K/s to 69 K/s as a primary investigation of the applicability of the processing method to BMGs.
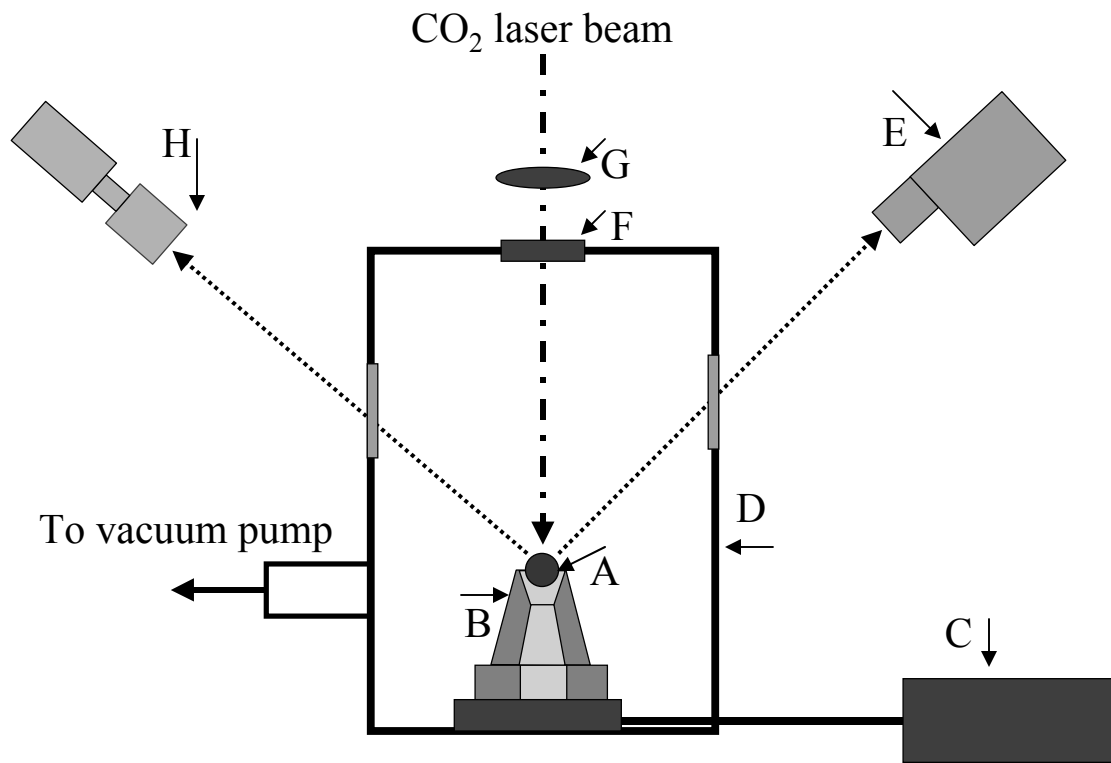
Figure 4.1 Schematic of the aerodynamic-levitator components. A – levitated sample; B – levitation nozzle; C – gas-flow-control system; D – chamber; E – optical pyrometer; F – CO_2-laser window; G – CO_2-laser-focusing lens; H – video camera. The chamber is equipped with viewports and connected to a vacuum-pump and pressure-control system.

4.2 Experimental Procedure

A $Zr_{57}Ti_5Ni_8Cu_{20}Al_{10}$ ingot was prepared by alloying the composition using high-purity (> 99.9%) elements and arc melting in a water-cooled-Cu crucible under a Ti-gettered, ultra high-purity (UHP) Ar atmosphere. Spherical specimens of ~ 3 mm diameter (approximately 130 mg each) were prepared by breaking up the master-alloy ingot and arc-remelting the small pieces on a water-cooled-Cu plate. The surface tension of the melt, coupled with the relatively high surface-area to volume ratio of the samples, allowed the production and retention of a near-spherical shape during arc melting.

The AL-processing experiments employed a conical nozzle to direct a jet of "cleaned" UHP Ar (< 1 ppm O_2) underneath the spheroidal specimens to achieve levitation in a sealed chamber with optical viewports for the observation of the specimen and the measurement of the sample temperature. The flow rates of the UHP Ar during the aerodynamic-levitation processing experiments were between 400 and 800 standard cubic centimeters per minute (SCCM), yielding maximum O_2 fluxes of 1.79 x 10^{14} to 3.58 x 10^{14} O_2 molecules/second. The levitating specimens were heated by a CO_2 laser that was aligned coaxially with the conical nozzle. The laser spot was on the top of each specimen. The temperature was recorded at a rate of 12 Hz using a 900-nm-wavelength optical pyrometer (Chino model IR-CAS2CN3). The sample apparent temperatures, T_A, as measured with the optical pyrometer, were related to the true specimen temperature, T, by Wein's approximation to Planck's Law:

$$\frac{1}{T} = \frac{1}{T_A} + \frac{\lambda}{C_2} Ln(\varepsilon_\lambda)$$ (4-3)

where λ is the nominal wavelength (0.9 μm) of the pyrometer, C_2 is the second radiation constant (14,388 μm K), and ε_λ is the spectral emissivity at the pyrometer wavelength. The spectral emissivity at the known melting point of the alloy was determined by correlating Eq. (4-3) with the known onset melting temperature (822ºC, [79]) to the observed melting endotherm in the time-temperature data, using:

$$\varepsilon_\lambda = \exp\left[(T_m^{-1} - T_{A(m)}^{-1}) \frac{C_2}{\lambda} \right] \qquad (4\text{-}4)$$

where T_m is the melting temperature, and $T_{A(m)}$ is the apparent-melting temperature. The calculated spectral emissivity, $\varepsilon_\lambda(T_{A(m)})$, was used to correct the temperature values over the entire range studied. Note the apparent temperatures measured with the pyrometer were also corrected for the radiation reflected from the viewport window ($\varepsilon_\lambda = 0.92\varepsilon_{material}$).

The specimens were heated in the levitator to a soak temperature (T_o) of 1,100ºC, at which point they were in the superheated-liquid state, and, subsequently, cooled at varying rates. The specimens were cooled via radiation and forced convection by the levitation gas. The cooling rate was controlled by the CO_2 laser coupled with feedback controls. The specimens were weighed before and after their respective experiments.

X-ray diffraction (XRD) measurements were performed over an angular range of $20° < 2\theta < 80°$. The diffraction spectra, collected on the as-processed specimens sectioned near the sphere center, were used to confirm the vitrification of, and to identify

the phases that formed during recalescence in, the samples processed faster and slower than the critical-cooling rate, respectively.

4.3   Results

Representative time-temperature curves from the aerodynamic-levitation processed $Zr_{57}Ti_5Ni_8Cu_{20}Al_{10}$ specimens are shown in Fig. 4.2. The curves show exothermic-recalescence peaks for the samples processed at cooling rates below 11 K/s (1.2 to 8 K/s), which is indicative of the nucleation and growth of crystalline phases in the as-processed specimens. The specimens processed at faster cooling rates (11 to 69 K/s) showed no evidence of this exothermic activity in the time-temperature curves during cooling, and, thus, did not exhibit a massive transformation during cooling. The recalescence temperature, T_r, of the specimens that crystallized during processing was found to vary with the cooling rate from ~ 730ºC at 1.2 K/s to ~ 652ºC at 8 K/s, just below the critical-cooling rate (CCR), yielding undercooling values ranging from 92ºC to 170ºC (the maximum undercooling with recalescence), respectively. Mass loss/gain analyses typically showed that the Δm magnitudes were less than 30 µg, or 2.3×10^{-2} % of the total-sample-mass post-processing. Note that a mass loss in this setup would be primarily due to volitization of the samples, while a mass gain would likely represent the absorption of impurities from the levitation gas.

The x-ray diffraction spectra exhibited the expected broad "amorphous" peaks centered at $2\theta = 37º$ for the specimens processed at the cooling rates of 13 K/s to 69 K/s, Fig. 4.3. The specimen processed at the cooling rate of 13 K/s showed some sharpening
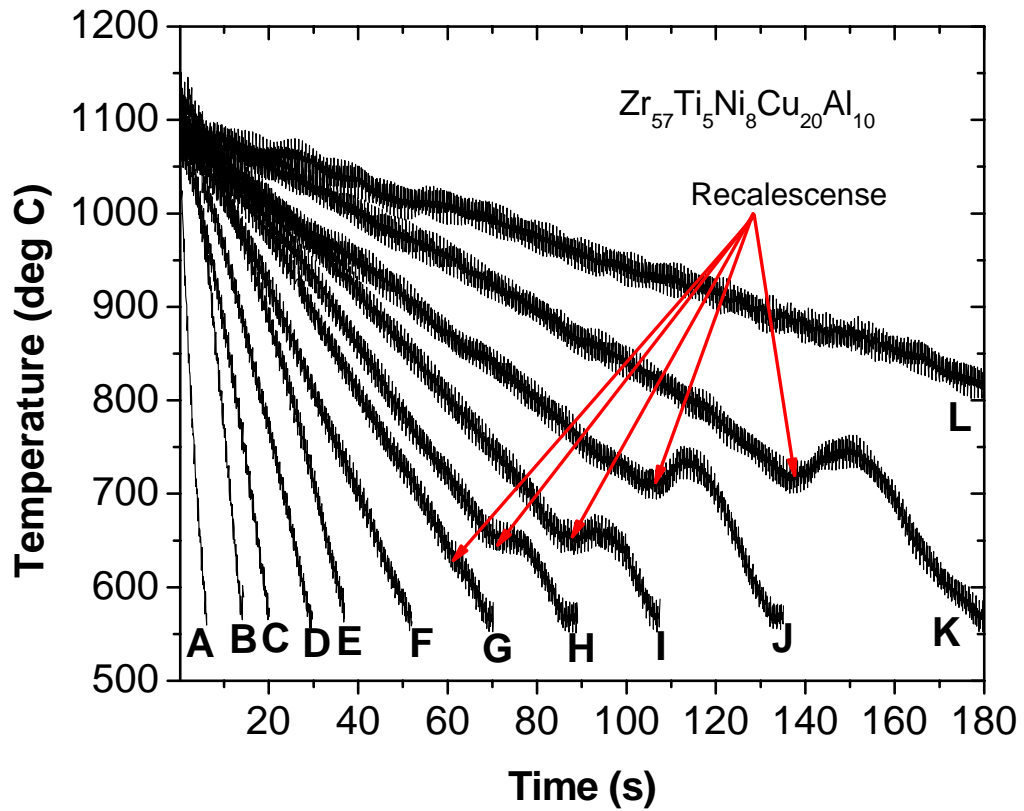
Figure 4.2 Time-temperature curves of $Zr_{57}Ti_5Ni_8Cu_{20}Al_{10}$ spheres processed with 69 K/s to 1.2 K/s cooling rates. The process cooling rates (slopes of the respective curves) are: A – 69 K/s, B – 38 K/s, C – 23 K/s, D – 16 K/s, E – 13 K/s, F – 11 K/s, G – 8 K/s, H – 6 K/s, I – 4.5 K/s, J – 3.5 K/s, K – 2.7 K/s, and L – 1.2 K/s (recalesced at t = 220 s, T = 730°C). Note that curve "G" exhibits a slight exotherm at ~ 625°C, which is not clearly visible in the scale used here.
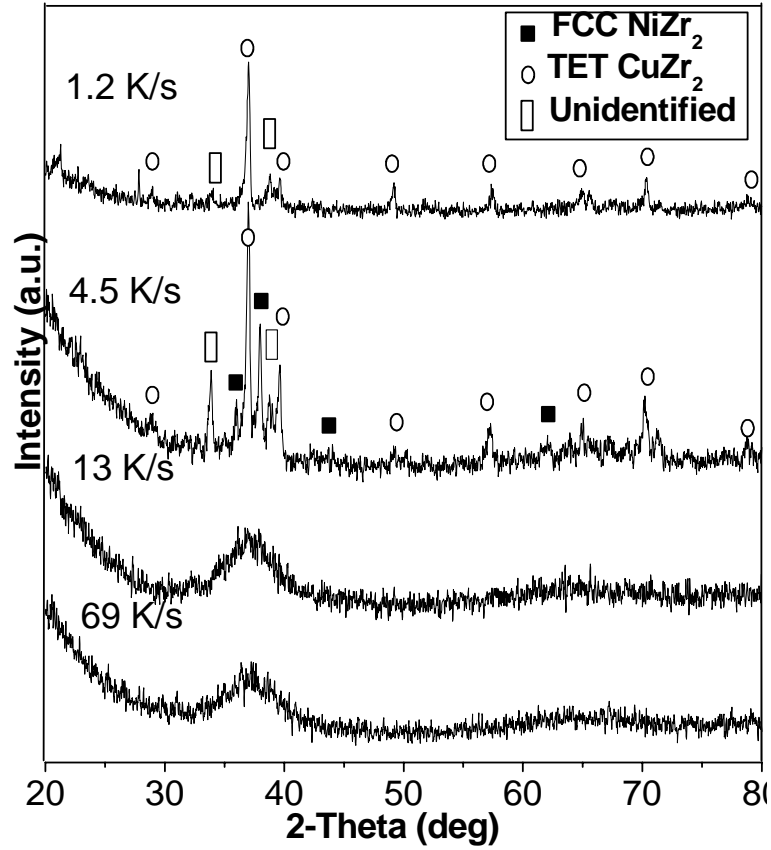
Figure 4.3 Representative XRD spectra from specimens processed at 69 K/s (lower), 13 K/s (lower mid), 4.5 K/s (upper mid), and 1.2 K/s (upper).

of the broad amorphous peak. The crystalline specimens processed below the CCR exhibited Bragg scattering from the tetragonal Zr_2Cu and cubic Zr_2Ni intermetallics as well as an unidentified phase. The crystalline samples processed near the CCR contained an appreciable amount of the metastable cubic Zr_2Ni phase, while the samples processed very slowly contained (primarily) Zr_2Cu. It must be noted that XRD spectra could not be collected for samples processed at 11, 8, and 6 K/s, as they were annealed before removal from the levitator.

4.4   Discussion

The application of AL to BMG processing allows one to directly probe the glass transition under a useful range of processing conditions. It is the hope of the authors that the flexibility of this technique will enable a further understanding of glass formation in alloys. Of primary concern with the use of AL processing to study bulk-metallic glasses is the inherent reactivity of most BMG-forming alloy systems. It has been seen that oxygen contamination can have a pronounced effect on the stability of Zr-based glass-forming alloys [71]. As mentioned previously, the levitation medium is potentially introducing oxygen into the system, with, for example, a maximum O_2 flux of 1.79×10^{14} molecules/second at a gas flow rate of 400 SCCM. In a 130-mg sample of $Zr_{57}Ti_5Ni_8Cu_{20}Al_{10}$ ($n = 1.05 \times 10^{21}$ atoms), assuming a 50%-O_2 absorption, this case would correspond to 0.1 ppm/second of O_2 being absorbed into the specimen. It is believed that the effect of traces of oxygen on nucleation is negligible at the small amounts (< 60 atomic ppm), which could occur in the short duration of the processing

experiments. It has been shown that the solubility of oxygen in superheated Zr-rich liquids is considerable before the precipitation of an oxide phase [80]. As such, the effect of oxygen contamination on the spectral emissivity of the superheated liquid was very likely negligible.

The AL-processing experiments can be performed so that the processing conditions prior to cooling (thermal history) are essentially the same for all the samples. This ability would allow the effects of doping or compositional variations on a liquid's stability to be observed directly. The duration of the processing experiments in this study (including a soak period at 1,100°C) for all specimens, with the exception of the 4.5 - 1.2 K/s cooling-rate experiments, was less than 300 seconds. Furthermore, a mass loss/gain analysis of the as-processed $Zr_{57}Ti_5Ni_8Cu_{20}Al_{10}$ specimens showed that the as-processed samples were typically within ± 30 μg of their original mass, indicating that the volatization was negligible. An appreciable absorption of impurities in the samples did occur at the + 30 μg extreme for the long duration experiment (1.2 K/s), which was likely due to primarily O_2 absorption from the levitation gas. However, the mass gain was negligible for samples processed near, and faster than, the CCR. We note that there exists a thermal gradient of several degrees Kelvin in the specimens from the laser spot to the underside. When the laser is blocked for free-cooling, this gradient diminishes. However, in the experiments where the incident laser power was slowly reduced (cooling at constant cooling rates), this gradient would persist throughout the cooling step. Nucleation in these samples would occur in the coolest region of the sample, on the underside where the levitation gas impinges. Nevertheless, the processing of bulk-metallic-glass specimens in a containerless environment was successfully carried out over

a range of cooling rates around the CCR. It is believed that this processing method may be employed to other systems with critical-cooling rates below ~ 70 K/s.

From the time-temperature data, we can conclude that there was no detectable exothermic transformation in the specimens processed at 11 K/s and faster. It is, then, apparent that the exact critical-cooling rate lies in the range from 11 K/s – 8 K/s for the bulk-metallic glass-forming alloy used in this study, $Zr_{57}Ti_5Ni_8Cu_{20}Al_{10}$, processed under AL conditions. This CCR could not be directly confirmed using XRD for the sample processed at 11 K/s, but is consistent with the data collected for the sample processed at 13 K/s. The XRD spectrum from the specimen processed near the CCR, at 13 K/s, showed some sharpening of the broad amorphous peak, as compared to that of the specimen processed at 69 K/s. This behavior is indicative of enhanced ordering as the processing conditions approach the limits of vitrification. Furthermore, the reclaseced samples processed near the CCR demonstrated an increasing exothermic output with decreasing cooling rate.   This phenomenon was likely the result of the nucleation and growth of a few crystallites without a massive transformation of the specimen due to the sluggish crystallization kinetics at sufficiently large undercooling.

4. 5   Conclusions

The bulk-metallic-glass-forming alloy used in this study, $Zr_{57}Ti_5Ni_8Cu_{20}Al_{10}$, was processed in a containerless environment at cooling rates of 69 – 1.2 K/s, using aerodynamic levitation.   The experimentally-measured critical-cooling rate for this composition was found to be 10 ± 1 K/s. Vitrification above the critical-cooling rate was

observed by tracking the time-temperature behavior of the cooling samples and confirmed by XRD. This study has shown that aerodynamic-levitation processing is a useful method to study the vitrification and solidification in glass-forming alloy systems over a relatively-wide range of cooling rates.

Chapter 5: Processing Zr$_{52.5}$Cu$_{17.9}$Ni$_{14.6}$Al$_{10}$Ti$_5$ (BMG-11) Metallic-Glass Containing High Levels of Oxygen by Microalloying With Erbium

Foreword

The current chapter describes the use of Er to neutralize the oxygen in a Zr-based BMG-forming alloy. Previous studies employed the use of rare-earth elements (Y and Sc) to achieve a similar effect. The use of Er was found to be an improvement over the previous studies. The contents of this chapter are a lightly revised version of a paper accepted for publication in the peer-reviewed journal *Materials Science & Engineering A*.

Wall, J. J., Fan, C., Liaw, P. K., and Choo, H., "Processing Zr$_{52.5}$Cu$_{17.9}$Ni$_{14.6}$Al$_{10}$Ti$_5$ (BMG-11) Metallic Glass Containing High Levels of Oxygen by Microalloying With Erbium," *Mater. Sci. Eng. A*. - in press (2007): Reference [81]

5.1   Introduction

Currently, there is much effort being directed toward the processing and commercialization of bulk-metallic glasses (BMGs). BMG materials based on a variety of metallic elements are of interest for their structural, chemical, magnetic, and/or electronic properties. Zr-based BMGs have been found to exhibit very high yield strengths (up to 2 GPa) and high elastic limits (~ 2 %) [53], as well as high fatigue-endurance limits [82-85]. High-strength Zr-based BMGs have been successfully implemented into several applications on a commercial scale [11]. One of the technical

hurdles that must be overcome to hasten a larger-scale commercialization of Zr-based, as well as other BMGs, is their typically stringent processing requirements. In order to form fully amorphous Zr-based BMGs, it is often necessary to use high-purity elemental-charge materials, and alloy and process them in an ultra-high purity environment. This caution must be taken to minimize the introduction of impurities into the alloys, which act to destabilize the glass by forming oxide particles that facilitate nucleation catalysis during undercooling due to small lattice disregistry with eutectic phases.

It was demonstrated by Lin et al. [7] that oxygen levels of ~ 5,000 ppm in BMG-11 can increase the critical-cooling rate by several orders of magnitude. Lu and Liu [35] showed that BMG-11 ingots containing 3,000 ppm oxygen routinely fail to vitrify during drop casting into a 6.4-mm-diameter water-cooled copper mold and, as such, proposed a microalloying strategy, based on a combination of B, Si, and Pb dopants, which stabilized Zr-oxide particles in solution. In a number of alloy systems, the glass-forming ability may be improved by doping with a "scavenging" element, which reacts with the impurity oxygen during processing to form particles benign to the heterogeneous nucleation of intermetallic phases [40, 41]. This method has been shown to be effective in processing impure Zr-based BMGs by doping with Sc and Y [42, 43]. The addition of Y to $Zr_{55}Al_{15}Cu_{20}Ni_{10}$ showed a tendency to form AlNiY, requiring relatively large amounts of the Y dopant (the cost is typically 3 USD/g), and a lowered crystallization temperature at higher concentrations. The addition of Sc in $Zr_{55}Al_{10}Cu_{30}Ni_5$ was found to be more efficient and thermodynamically benevolent, but is likely of a limited industrial utility due to the high cost of scandium (typically 100 USD/g) [86].

Here, we report the formation of amorphous BMG-11 rods cast from ingots containing up to 16,000 ppm oxygen by doping with Er. The resultant materials show rare-earth aluminate dispersions in a fully-amorphous BMG-11 matrix, and exhibit similar properties to high purity BMG-11. This is a practical means to increase the processability of BMG-11 with a relatively low-cost element, Er (typically 5 USD/g).

5.2   Experimental

35-g ingots of $Zr_{52.5}Cu_{17.9}Ni_{14.6}Al_{10}Ti_5$ of varying impurity oxygen concentrations were created by combining high-purity elemental charge materials (purity > 99.9%) with the appropriate amounts of ZrO_2 ($\Sigma Zr = 52.5$ atomic percent, at.%) and mixing in an arc-melting furnace. ZrO_2 is readily absorbed into the alloy under such conditions, as demonstrated by Lin et al. [7]. Ingots of each impurity oxygen concentration were, then, combined in an arc furnace to form master ingots of three impurity-oxygen concentrations. The master ingots were divided into 20-g charges. The charges were, subsequently, alloyed with varying amounts of erbium (0 - 1 at.%). The Er-doped (and un-doped) charges were, then, melted in the arc furnace and drop cast into a water-cooled-copper mold to form rods of 6.4 mm diameter x ~ 70 mm length. A detailed description of the casting apparatus was presented in Chapter 3 [44]. The as-cast rods were sectioned 15 mm from the bottom and again at 25 mm from the bottom, yielding 10-mm-length cylinders, which were used for structural, thermal, and chemical analyses. The microstructure was analyzed by scanning-electron microscopy and energy-dispersive x-ray spectroscopy. Laboratory x-ray diffraction spectra were taken over a *2θ* range of

20º to 80º using CuK$_\alpha$ radiation. Differential-scanning-calorimetry measurements were performed using a heating rate of 20 K/min. Wet-chemical analyses were conducted to determine the oxygen concentrations of the as-cast samples. A series of compression tests were performed under monotonic-loading conditions at a constant strain rate of - 3 x 10^{-5}/s.

5.3   Results

Chemical analyses showed oxygen contents of 5,000, 6,250, and 14,000 ppm for each respective group of samples cast from the three master ingots, scaling with the amount of the ZrO$_2$ addition. Note that one sample (doped with 10,000 ppm Er) was found to contain 16,000 ppm oxygen, likely due to a slight vacuum leak during casting. Laboratory x-ray diffraction (XRD) spectra taken from the as-processed specimens show that at all levels of oxygen impurity content, the Er addition had a considerable effect on the neutralization of oxygen in Zr$_{52.5}$Cu$_{17.9}$Ni$_{14.6}$Al$_{10}$Ti$_5$ during processing. The undoped samples were found to contain tetragonal and cubic intermetallics in the lower-oxygen-containing samples (< 14,000 ppm oxygen). The sample containing 14,000 ppm oxygen was found to crystallize into solely FCC NiZr$_2$ during casting. XRD spectra from the 6,250-ppm and 14,000-ppm oxygen-containing samples (doped and undoped) are presented in Figs. 5.1 and 5.2, respectively. XRD spectra are not presented here from the 5,000-ppm-oxygen-containing samples as they follow the data trend established by those presented and are redundant. The XRD spectra of Fig. 5.1 showed intermetallic Bragg

73
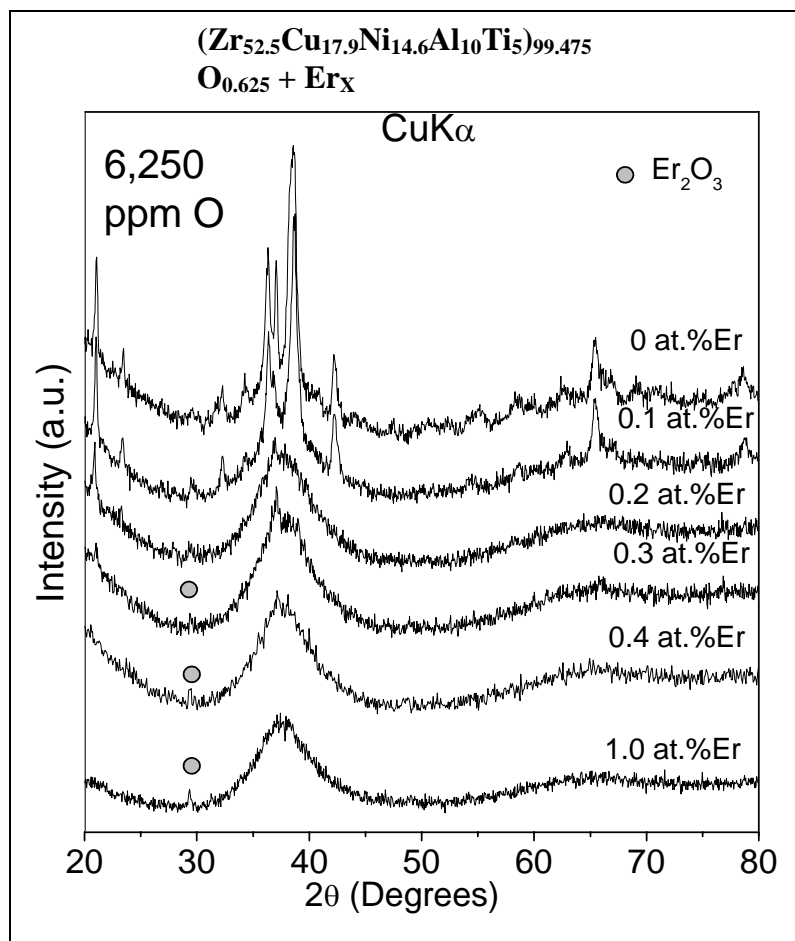
Figure 5.1 X-ray diffraction spectra taken from $Zr_{52.5}Cu_{17.9}Ni_{14.6}Al_{10}Ti_5$ samples containing 6,250 ppm oxygen with varying amounts of the Er dopant.
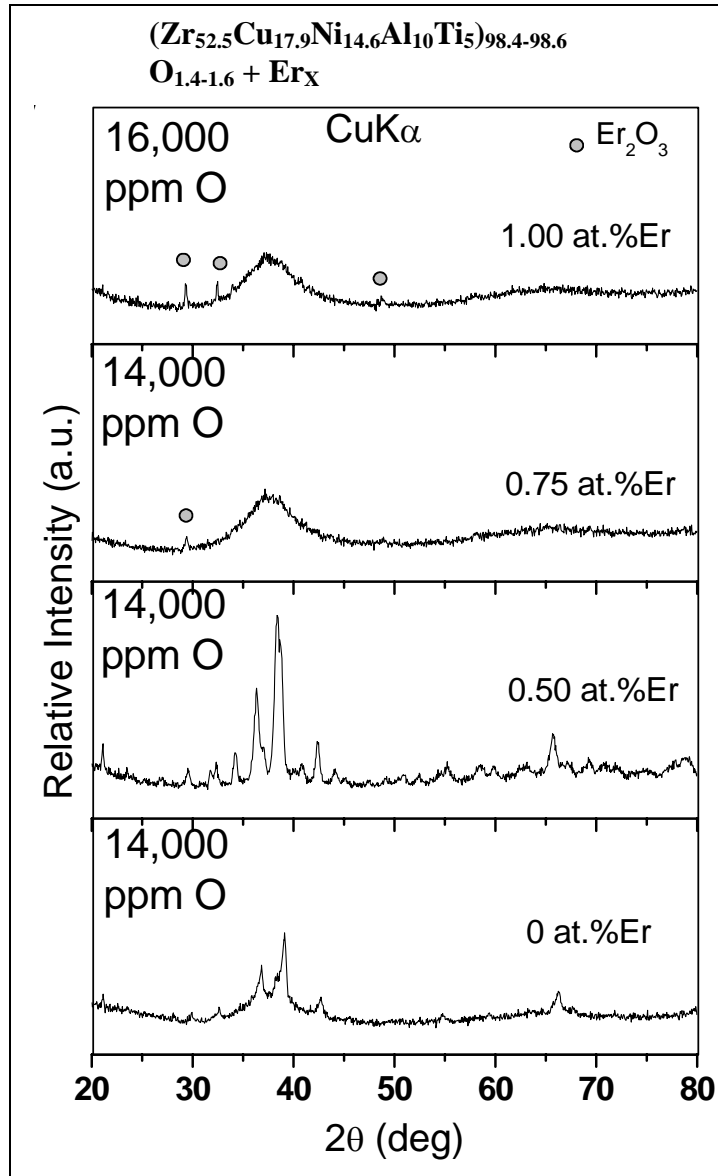
Figure 5.2 X-ray diffraction spectra taken from $Zr_{52.5}Cu_{17.9}Ni_{14.6}Al_{10}Ti_5$ samples containing 14,000 ppm oxygen with varying amounts of the Er dopant. Note that the top-most curve is representative of the sample containing 16,000 ppm oxygen.

peaks from the cubic and tetragonal phases decreasing in intensity with increasing Er content. Also, Er_2O_3 peaks emerge with increasing prevalence as a function of the oxygen/erbium content. In addition, there was no detectable Bragg scattering from intermetallic phases for Er supersaturation (defined here as doping beyond what is required to suppress intermetallic-phase formation) up to 6,000 ppm, which is evident from the bottom spectrum of Fig. 5.1. Figure 5.2 presents a similar effect of doping to that presented in Fig. 5.1, extending to the 14,000 - 16,000 ppm oxygen concentrations. Note that the diffraction spectra of the undoped sample exhibited lower relative intensities of the cubic-phase Bragg peaks at the highest oxygen level.

Scanning-electron microscopy revealed the existence of crystallites in an amorphous matrix with changing particle morphology as a function of the oxygen content in the Er-doped materials, as presented in Figs. 5.3 (a) and (b). The Er-doped samples containing 5,000 - 6,250 ppm oxygen showed cube-like inclusions of typically 2 - 3 μm edge length, while the Er-doped specimens containing 14,000 - 16,000 ppm oxygen exhibited needle-like growths protruding from 600 – 700 nm core crystallites. These inclusions (independent of the morphology) were determined to have a cubic Er_2O_3 structure ($I2_13$, a = 10.54 Å) by the Bragg-peak positions. Energy-dispersive x-ray spectroscopy showed that the crystallites were deficient in Zr, Cu, Ni, and Ti, and enriched in Er, O, and Al. X-ray excitation maps in 1- and 2- spatial dimensions of a particle and the surrounding matrix, at the characteristic energies of the constituent elements, are shown in Figs. 5.4 and 5.5.
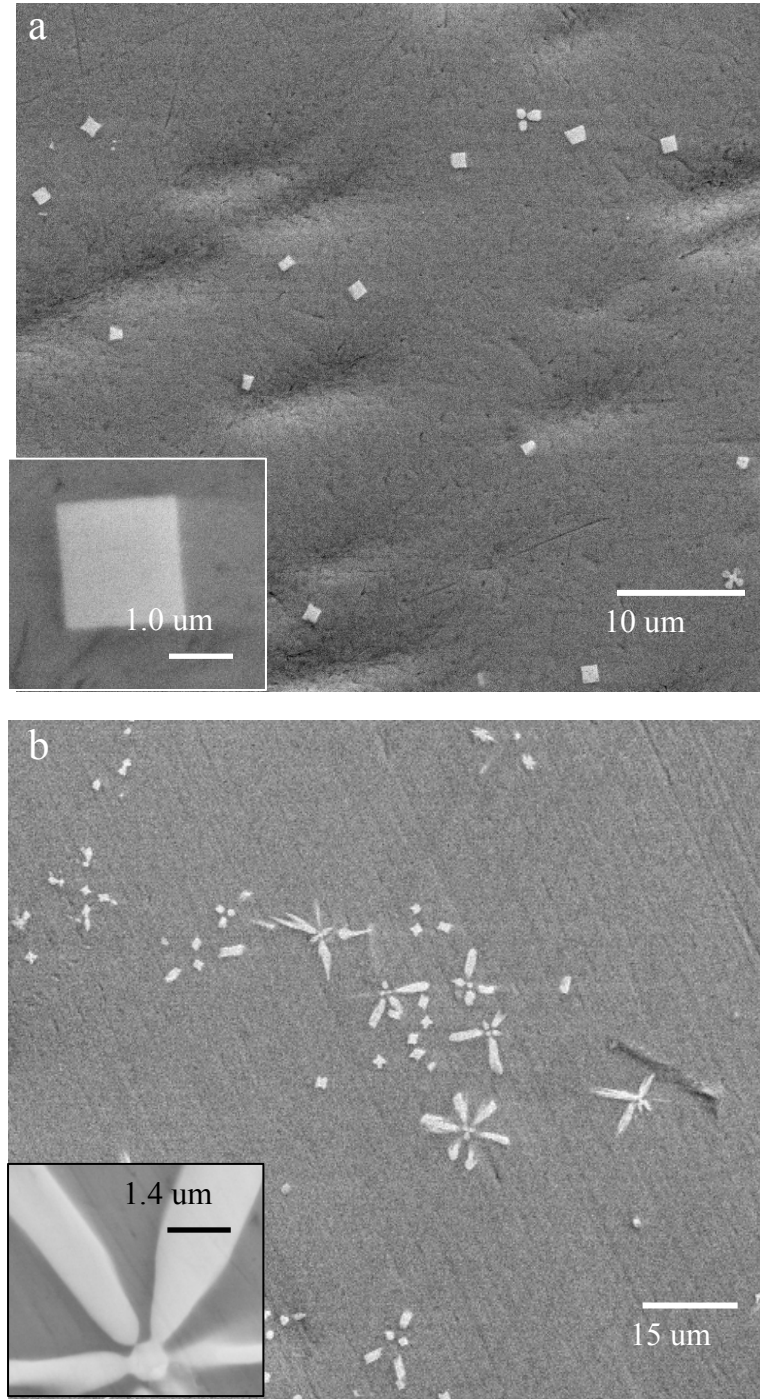
Figure 5.3 SEM micrographs showing the microstructure of the inclusions in Er-doped $Zr_{52.5}Cu_{17.9}Ni_{14.6}Al_{10}Ti_5$ cast samples containing oxygen. (a) Is representative of the 6,250-ppm-O, 4,000-ppm-Er containing sample, and (b) is representative of the 16,000-ppm-O, 10,000-ppm-Er containing sample (insets show higher magnification).
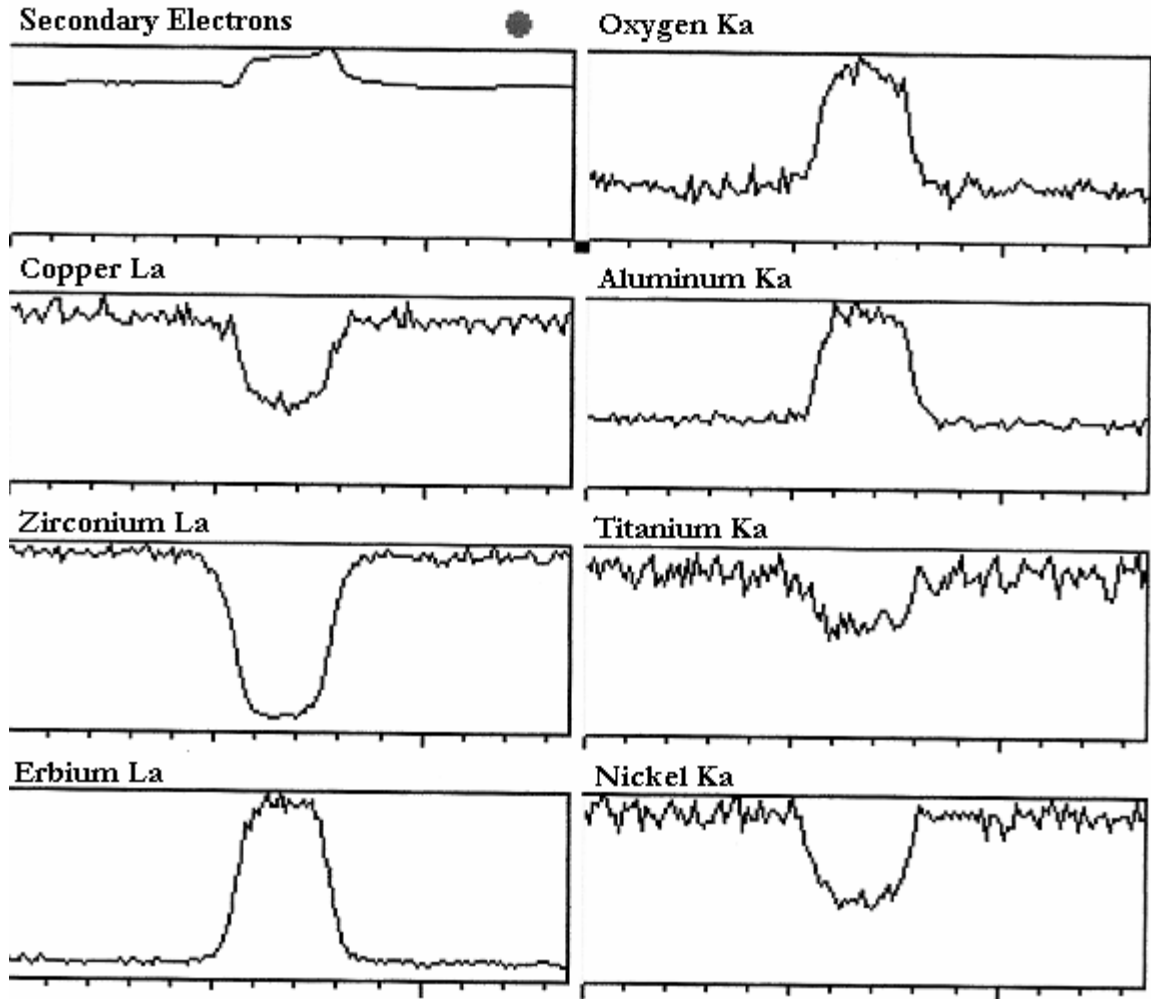
Figure 5.4 Energy-dispersive x-ray-excitation maps in one spatial dimension, generated during a matrix-precipitate-matrix line scan, which shows the profiles for Cu, Zr, and Er (L_α) and O, Al, Ti, and Ni (K_α). The curve at the upper left is the secondary-electron profile for the particle-width reference.
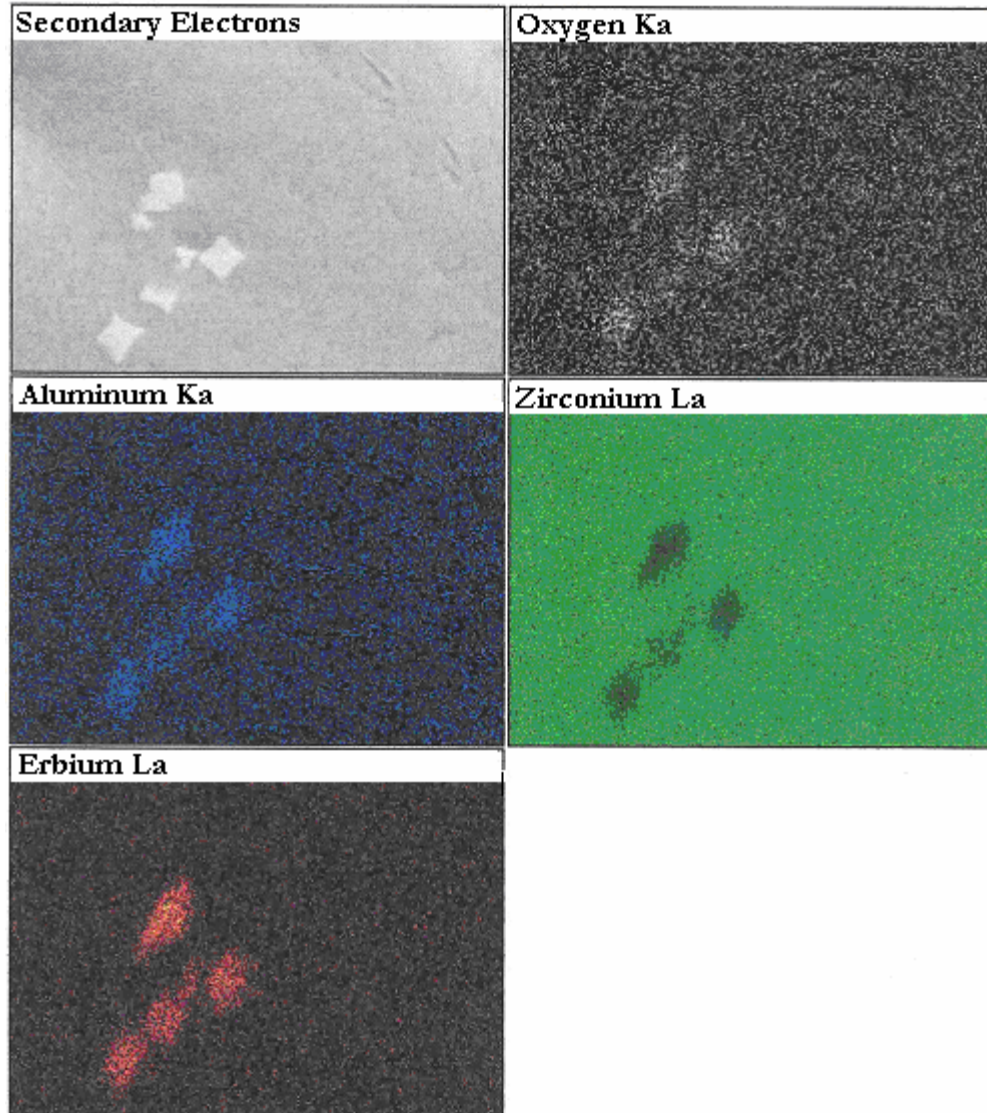
Figure 5.5   X-ray excitation maps in two spatial dimensions, showing a graphical representation of the concentration profiles of a particle and the glass matrix. The image in the upper left is a secondary-electron image of the inclusions.

The glass-transition temperatures (T_g) and crystallization temperatures (T_x) of the Er-doped samples were homogeneous. Several DSC traces are shown in Fig. 5.6 to illustrate this uniformity. The DSC measurements revealed a slight (- 2 K) shift in the peak temperature (T_p) for the sample containing 16,000 ppm oxygen and 10,000 ppm Er. Note also that there was a - 2 K shift of T_x for the sample supersaturated with 6,000 ppm Er (not shown in the figure). The enthalpy change (ΔH_x) during crystallization was found to decrease by ~ 6% in the Er-doped samples containing 14,000 – 16,000 ppm oxygen as compared with the sample containing 5,000 ppm oxygen. The compression testing results are presented in Table 5.1.

Table 5.1   Monotonic compression-testing results for the high-oxygen, Er-doped samples.

Ingot ID	ppm O / ppm Er	Fracture Strength (MPa)
1	5,000 / 1,500	1,650
2	6,250 / 4,000	1,400
2	6,250 / 10,000	1,500
3	14,000 / 7,500	1,430
3	16,000 / 10,000	1,500
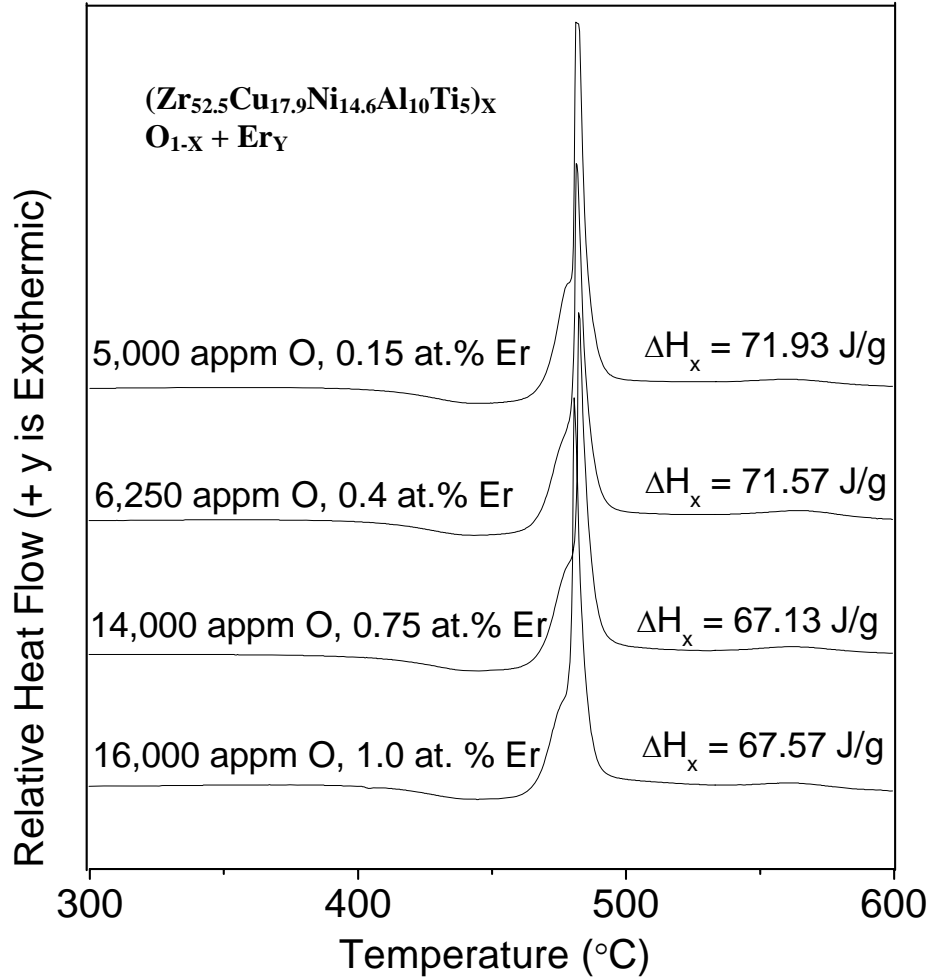
Figure 5.6 Differential-scanning-calorimetry curves and the representative enthalpy of crystallization (ΔH_x) values of the Er-doped specimens with varying impurity oxygen contents.

5.4   Discussion

The effect of the Er dopant on the stabilization of the liquid structure of the $Zr_{52.5}Cu_{17.9}Ni_{14.6}Al_{10}Ti_5$ alloy during processing was quite substantial.   Prior to any subsequent analysis, it seemed intuitive that the oxygen in solution was reacting with the Er dopant during processing and forming erbium-oxide crystallites that exist in equilibrium with the $Zr_{52.5}Cu_{17.9}Ni_{14.6}Al_{10}Ti_5$ alloy during cooling from the melt.   The formation of the rare-earth oxide is thermodynamically favored due to the high chemical affinity of Er for oxygen.   The enthalpy of formation of Er_2O_3 is reported as $\Delta H = -1,899$ kJ/mol [87] and it exists as a stable compound in the superheated-liquid state of BMG-11. The absence of the Er dopant was found to result in the formation of intermetallics.

In the Er-doped samples, aluminum was consumed in the Er-O reaction and manifests itself as antisites in the $I2_13$ lattice at the Er positions.   This substitution is not surprising since both Al and Er have a valence of $+3$, and Al has a small atomic radius (143 pm) in relation to Er atoms (178 pm), giving it good relative mobility in solution. Also, aluminum has a high thermodynamic propensity to react with oxygen ($\Delta H_{Al} = -1,582$ kJ/mol).   The evolution of the morphology of the anticatylist particles from (primarily) micro-sized cubes to nano- to micro-sized "star-like" dendritic particles is interesting.   It seems that the breakdown of the planar-solidification front is highly dependent on the concentration of Er, Al, and/or O in the surrounding material. Note that it is likely that the cube-like inclusions formed more slowly than the star-like inclusions since their growth required a longer-distance net migration of Er, Al, and O. Gebert et al. [88] found similar "star-like" morphologies in a Zr-Cu-Ni-Al glass-forming alloy

containing 2,800 ppm oxygen. These were likely FCC Zr_4Ni_2O, as pointed out by Lu and Liu [35], and, as such, catalyzed the formation of intermetallics.

As presented in the introduction, oxygen-scavenging phenomena have been observed in Zr-based BMGs by Zhang et al. [43] and Jiang et al. [42] by doping with yttrium and scandium, respectively. It is interesting to note that in these previous studies, dopant concentrations of Sc were approximately consistent with those predicted by stochiometry while Y required a saturation of a factor of ~ 10, possibly due to the tendency to form AlNiY in the latter. In the present study, the ability of the Er_2O_3 structure to accommodate Al atoms allowed a stochiometrically *deficient* amount of the dopant to be adequate to suppress the crystallization in some cases.

It seems apparent that the high degree to which Er doping stabilizes BMG-11 lies in both its thermodynamic propensity to react with oxygen as well as the ability of the nucleated oxide particles to exist in a benign state with the undercooled liquid $Zr_{52.5}Cu_{17.9}Ni_{14.6}Al_{10}Ti_5$. This phenomenon is similar to the effects of the Y addition in $Zr_{55}Al_{15}Cu_{20}Ni_{10}$, and Sc addition in $Zr_{55}Al_{10}Cu_{30}Ni_5$, as reported by Zhang and Jiang, respectively [42, 43]. The efficiency of reactants to products (anticatalyst oxides) seems to be optimal with Er. The complex structure of Er_2O_3 would not be a likely catalyst for the formation of the stable tetragonal phases $CuZr_2$ (I4/mmm, a = 3.22 Å, c = 11.18 Å) and $NiZr_2$ (I4/mcm, a = 6.483 Å, c = 5.267 Å), or the metastable FCC $NiZr_2$ (Fd-3m, a = 12.286 Å) phase during undercooling due to large lattice disregistries, per the criteria outlined by Turnbull and Vonnegut [39]. In contrast, it was shown by Altounian et al. [89], that in rapidly solidified stoichiometric $NiZr_2$, oxygen stabilizes the FCC $NiZr_2$ phase. This phase is a common precipitate in primary annealed Zr-based BMGs [88, 90,

91]. We note here the formation of FCC Ni_2Zr in the *as-cast*-oxygen-containing samples (Figs. 5.1 & 5.2). The broad nature of the Bragg diffraction peaks from the sample containing 14,000-ppm oxygen suggests that the alloy formed a FCC $NiZr_2$ nanostructure during casting. As such, nanocrystallization was favored by the presence of a high amount of oxygen, which may have resulted in an enhanced concentration of FCC-innoculant dispersions in the undercooled liquid. Assuming, then, that a sufficient amount of oxygen is neutralized as the stable $(Er, Al)_2O_3$ phase, the free-energy barrier for crystal nucleation approaches that for homogeneous nucleation, facilitating the vitrification of the glass-forming-alloy composition during casting in the presence of relatively large amounts of oxygen.

The uniformity of the thermal stability of the as-processed specimens, independent of the oxygen and/or erbium concentrations, suggests that the Al deficiency in the matrix created by the Er/Al/O reaction does not change the eutectic-energy landscape of the alloy substantially. This observation seems counterintuitive, as glass-forming alloys are often quite sensitive to compositional variations. Furthermore, an Er supersaturation up to 0.6 at.% was found not to promote the nucleation of intermetallics during casting. However, there was a slight (2 K) decrease in T_x in the Er-supersaturated sample, which implies that Er has a weak destabilization effect when present in solution in the glass. The slight decrease of $\mathit{\Delta H_x}$ at the highest oxygen concentration was likely a consequence of the relative amounts of the stable $(Er, Al)_2O_3$ phase in the samples.

The compressive rupture strengths of the high-oxygen content, Er-doped BMG-11 samples (1,525 +/- 125 MPa) were found to vary slightly and irregularly, with the O and Er concentrations. The variance (8.2%) is believed to be within the margin of error under

the setup used. The slight decrease in the compressive strength in the Er-doped samples, as compared to literature values for high-purity BMG-11 (1.75 GPa), may be due to the preferential nucleation of shear bands at the anticatalyst / matrix interfaces. We note also that there was no apparent effect on the plasticity of the as-cast materials by shear band - particle interactions.

5.5   Conclusion

In conclusion, we report here upon the formation of $Zr_{52.5}Cu_{17.9}Ni_{14.6}Al_{10}Ti_5$ BMG matrix composites with oxygen concentrations of up to 1.6 at.% by doping with erbium. This Er-dopant stabilized the liquid structure by reacting with the oxygen and Al atoms while the alloy was in the liquid state, during processing, by the formation of $(Er, Al)_2O_3$ anticatalyst particles in lieu of cubic-oxide particles, which catalyze the nucleation of FCC $NiZr_2$.   The rare-earth aluminate particles did not trigger the heterogeneous nucleation of intermetallics in the undercooled alloy due to their structural dissimilarity with the competing eutectic phases.   Particle morphologies were dependant on the oxygen concentration, evolving from cube-like inclusions to a simple dendritic "star-like" morphology.   It was found that neither Er nor oxygen content affected the thermal stability of the as-cast Er-doped specimens.   However, overdoping with Er seemed to lead to a weak destabilization of the glass upon reheating.   The compressive rupture strength was found to be approximately invariant in the as-cast composites regardless of the Er/O content. In addition, we note that due to the very high chemical affinity of Er

for O, this method should easily be applicable to other glass-forming compositions, particularly in the family of Zr-based BMG-forming alloys.

Chapter 6: Investigations of Oxygen-Induced Nucleation in a Zr-Based Glass-forming Alloy

Foreword

The current chapter describes investigations of oxygen-induced nucleation in the VIT-105 alloy. These studies utilized synchrotron x-ray and neutron scattering to further identify catalysts and products involved in heterogeneous nucleation. The work described herein has been assembled into a draft for publication in a peer-reviewed journal, which has been modified slightly for incorporation into this dissertation.

Wall, J. J., Weber, R., Kim, J., Liaw, P. K., and Choo, H., "Synchrotron X-ray and Neutron Scattering Investigations of Oxygen-Induced Nucleation in a Zr-Based Glass-Forming Alloy," **to be designated.**

6.1 Introduction

The devitrification of metallic-glass systems by isothermal annealing has been used to produce glassy-matrix composites [92, 93], nanostructured materials [94, 95], and quasicrystalline phases [96, 97], and has been shown to result from shear deformation [98, 99]. Altounian et al. [89] showed that the first nucleation product in an amorphous stoichiometric $NiZr_2$ during reheating is a metastable face-centered-cubic (FCC) phase with a lattice parameter, a, of 12.27 Å in the presence of > 1 at.% oxygen. Subsequent work indicates that this FCC phase forms in a variety of Zr-based bulk-metallic-glass-

forming alloys (BMGs) upon reheating in the presence of oxygen [88, 91, 100, 101]. Oxygen contamination, in a general sense, results in a reduced glass-forming ability in Zr-based BMGs, as demonstrated in the VIT-105 composition ($Zr_{52.5}Cu_{17.9}Ni_{14.6}Al_{10}Ti_5$) by Lin et al. [7].

6.2   Experimental

VIT-105 ingots with oxygen contents of 5,000 ppm, 6,250 ppm, 14,000 ppm, and 16,000 ppm (*atomic* herein) were produced by melting elemental constituents and ZrO_2 in a water-cooled hearth using an arc-melter under an ultra-high purity (UHP) argon cover. The ingot containing 16,000-ppm oxygen was doped with 10,000 ppm of Er. The ingots were, then, drop-cast into rods of 6.4 mm in diameter x 80 mm in length and sectioned for analyses. A description of the casting equipment and preliminary analyses can be found in [44] and [81], respectively. Disks of 1.0 mm in thickness were cut from each casting for ex-situ synchrotron x-ray measurements. Three-millimeter diameter spheroids of the un-doped 14,000 ppm and Er-doped 16,000-ppm oxygen-containing samples were used for an in-situ x-ray study. These samples were prepared by arc-remelting a small amount of the as-cast material on a water-cooled copper plate, allowing the surface tension of the melt to form a spheroid.

6.2.1 Synchrotron X-ray Scattering Measurements / Techniques

Ex-situ synchrotron x-ray scattering (SXRS) measurements were performed on the disks of the as-cast materials at the Advanced Photon Source (APS), located at the Argonne National Laboratory on the 1-ID beam-line. The measurements were performed in a transmission geometry using an incident X-ray beam energy, E_i, of 80.70 keV (λ = 0.1536 Å) and a sample to detector (Mar-230 image-plate) distance, z, of 547.3 mm. The x-ray wavelength, detector non-orthogonality, and z were refined using a NIST-SRM 674 [102] CeO_2 Debye pattern taken under identical conditions. The x-ray beam cross section was 500 μm x 500 μm.

In-situ, time-resolved SXRS measurements on the 14,000 ppm and Er-doped 16,000 ppm oxygen-containing samples in the superheated liquid state were performed on beamline 11-ID-C at the APS. Scattering measurements were made in a transmission geometry using E_i and z of 115.12 keV (λ = 0.1077 Å) and 449.4 mm, respectively, again refined using a NIST-SRM CeO_2 pattern. The x-ray energy was sufficient to penetrate the samples, providing a bulk probe of the liquid. The x-ray beam cross section was 1,000 μm x 1,000 μm. A Mar-345 image-plate detector was used. The acquisition time of the image plate was approximately 30 seconds, followed by a readout time of 90 seconds. X-ray spectra were collected continuously for approximately 5 minutes during each experiment, yielding 3 separate scattering patterns for each sample. The samples were suspended in a containerless environment using an aerodynamic levitator installed on the beam-line and heated with a 240-W-CO_2 laser, using a configuration similar to that employed in a prior study [103]. The samples were levitated by flowing UHP argon

(approximately 1 L/min.) through a specially-designed nozzle within an enclosed stainless-steel chamber. Note that the chamber was not hermetically sealed and, thus, did not achieve a complete isolation of the sample environment. The x-ray beam intercepted only the top half of the sample. Kapton windows in the chamber allowed the transmission of the incident and scattered radiation with minimal attenuation. A schematic of the beam-line levitation experimental setup is shown in Fig. 6.1.

The sample temperatures were controlled by adjusting the incident laser-beam power. The apparent temperature, T_A, of each sample was measured with a Mikron M90V pyrometer that operates at a wavelength of 650 nm. The pyrometer was aligned to view a 1-mm-diameter spot in the region where the sample was probed by the x-ray beam. T_A was held constant at 1,200ºC and 1,500ºC for the undoped and Er-doped samples, respectively, throughout the duration of the experiment. The true temperatures of the samples were estimated from the T_A values using Wein's approximation to Planck's Law, Eq. (4-3). Spectral-emissivity values of 0.48 and 0.68 for the undoped and Er-doped samples, respectively, were estimated from the literature data on similar materials at the temperatures of interest [104, 105]. The error in the emissivity was conservatively estimated at 30%. Corrections to the emissivity values were made for the reflected thermal radiation from the pyrometer-focusing lenses and Pyrex-viewing window. The estimated true temperatures, T, of the samples were 1,320ºC ± 40ºC and 1,595ºC ± 60ºC for the undoped and Er-doped samples, respectively. The temperature gradient in the probed volume of each sample was estimated to be ≤ 10ºC.
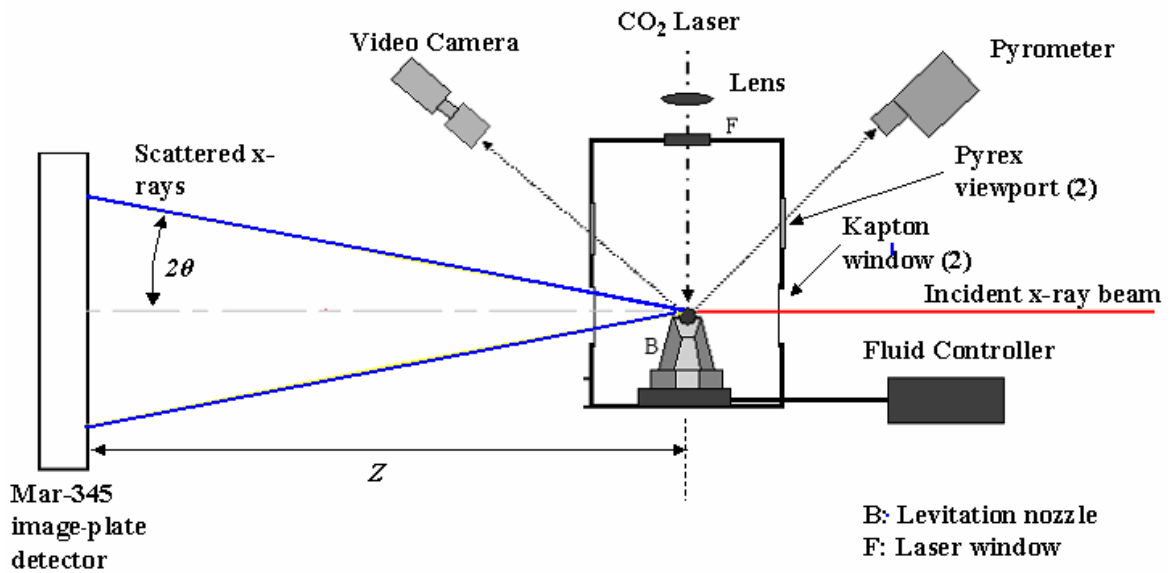
Figure 6.1   A schematic of the beam-line aerodynamic levitation experimental setup. The primary components of the levitator and measurement equipment are highlighted. The transmission-scattering geometry is indicated by the incident and scattered radiation.

6.2.2   Scattering-Data Analyses

The 2-D image-plate data sets were integrated about the azimuth to obtain the scattering intensity patterns, *I(Q)*, where *Q* is the scattering-momentum transfer, which is proportional to the diffraction-plane spacing, *d*, by the relation $Q = \frac{2\pi}{d}$. The data was reduced to this form using the Fit2D software [106]. The *I(Q)* patterns were fit by the whole powder-pattern-matching Rietveld method [49] using the GSAS program [107]. Details of the method used to fit diffraction from the glass are provided in Appendix B.

6.3   Results

The ex-situ SXRS patterns showed that the samples containing 5,000-ppm, 6,250-ppm, and 14,000-ppm oxygen crystallized during casting. It was observed that increasing the oxygen content from 5,000 to 6,250 ppm resulted in an increased number of diffracting crystals, seen in the patterns as additional Laue diffraction spots, Fig. 6.2 (a & b). Rietveld fits of the integrated diffraction spectra revealed that the primary phase in the samples containing 5,000 and 6,250-ppm oxygen was a tetragonal Al_3Zr_2-type phase ($P4_2$/mnm) with *a* = 7.40 Å, *c* = 6.66 Å, coexisting with a small relative amount of a secondary phase. The structure of the primary phase is consistent with the electron-diffraction identification of Zr-Cu(Ni) crystalline inclusions in an as-cast, high-purity VIT-105 presented by Pekarskaya et al. [108]. Diffraction from the minor phase is consistent with FCC Zr_2Ni (Fd-3m).
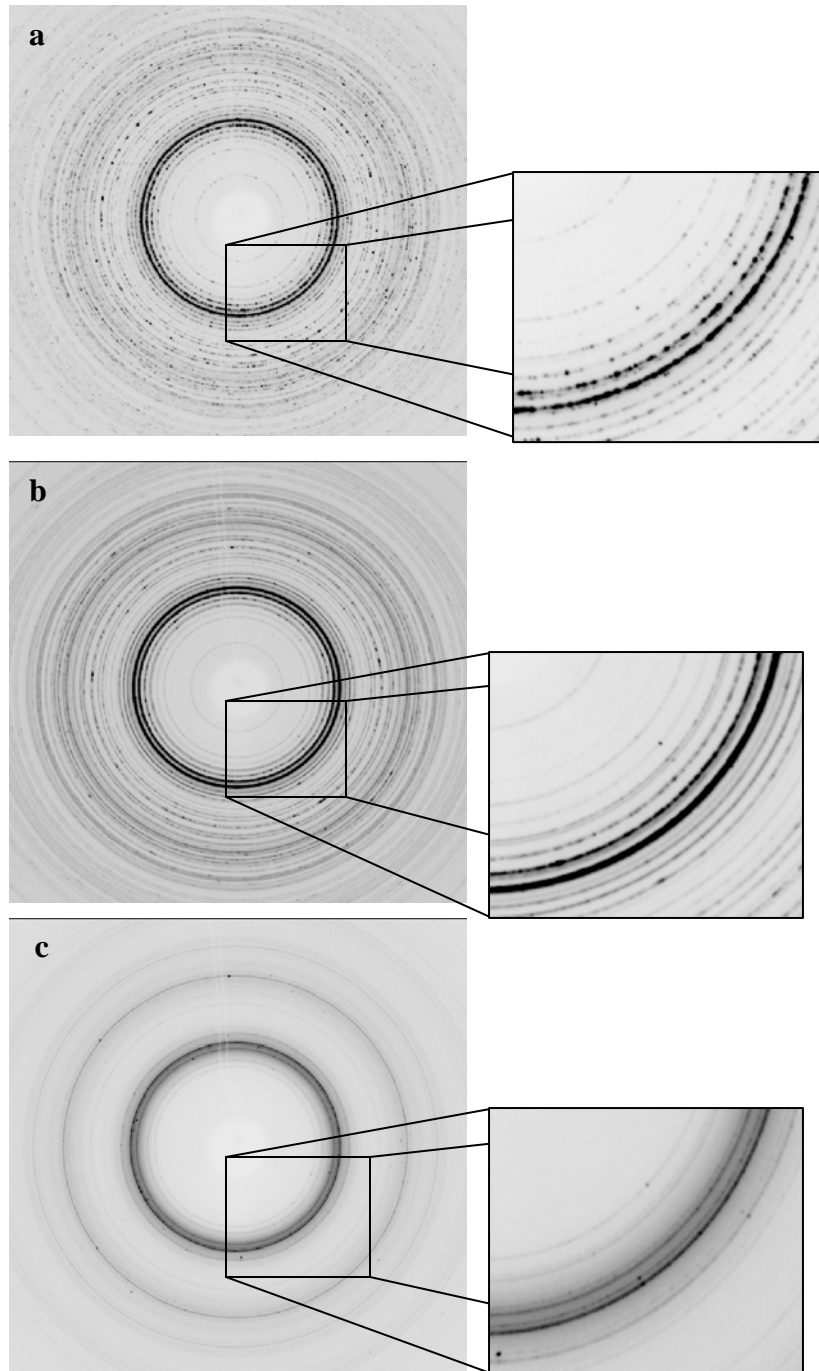
Figure 6.2 2-dimensional synchrotron x-ray scattering spectra from as-cast VIT-105 samples containing; (a) 5,000 ppm oxygen, (b) 6,250 ppm oxygen, and (c) 14,000 ppm oxygen, collected in transmission geometry by a MAR-230 image plate. The 4th-quadrant-scattering data was enlarged to show details.

The sample containing 14,000 ppm oxygen was found to contain a fine-grained structure, as is apparent from the (relative) intensity and continuity of the Debye rings, Fig. 6.2(c). Fitting of the integrated $I(Q)$ pattern revealed coexisting Fd-3m phases with lattice parameters of 11.93 Å and 12.16 Å, respectively, after least-squares refinement. These phases are consistent with the Zr_3Ni_2Ti and Zr_2Ni structures, both of which can be stabilized at high temperatures by interstitial oxygen. Note that the $Zr_4Ni_2O_X$ and $Zr_6Ni_4Ti_2O_X$ structures presented by Mackey et al. [109] were used as starting structures for the fit. In addition, a significant amount of a residual amorphous material was present, which was evident (qualitatively) from the relative amount of glass scattering in the integrated $I(Q)$ pattern. The fitted diffraction patterns for the samples containing 5,000 and 14,000-ppm oxygen are shown in Figs. 6.3 and 6.4, respectively.

Upon a close inspection of the 2-D diffraction pattern of the as-cast sample containing 14,000-ppm oxygen, it was observed that, in many instances, intense Laue diffraction spots from planes in the FCC phases were coupled along a radial projection from the center. This significant finding reveals that relatively large crystals of the two phases, which are similar in atomic structure, have the exact same crystallographic orientation in the sample. Examples of coupled diffraction spots for several *hkl* planes are shown in Fig. 6.5. These coupled Laue spots indicate diffraction from large (phase 1):(phase 2) oriented crystalline agglomerates that appear to have formed via epitaxial heterogeneous nucleation.
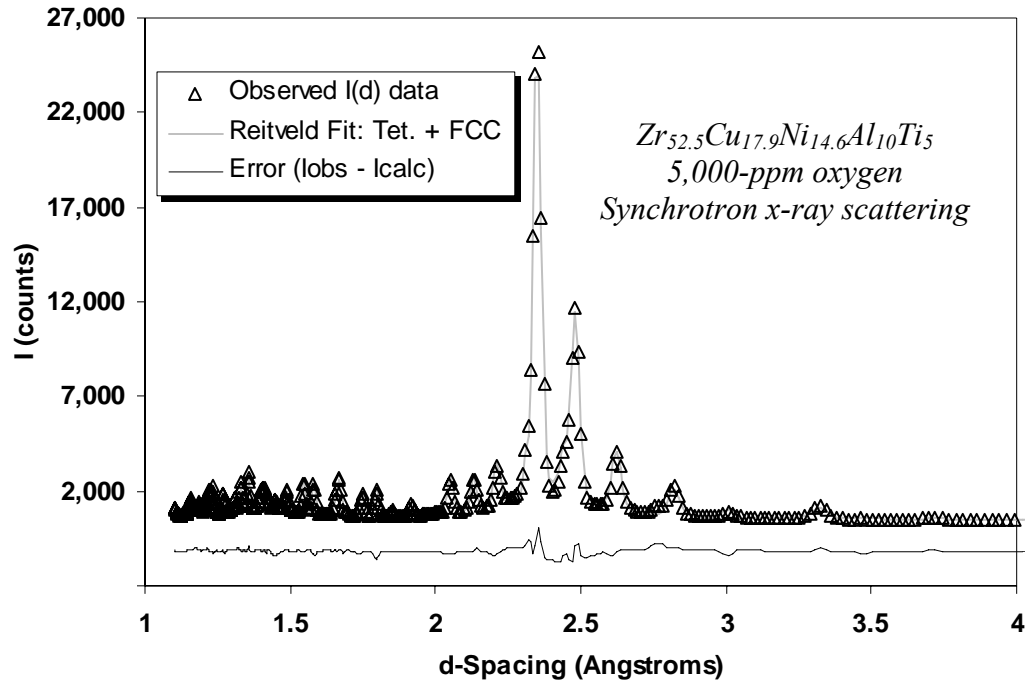
Figure 6.3 Rietveld fit of the integrated *I(d)* spectrum for the as-cast sample containing 5,000-ppm oxygen. The open triangles indicate the measured data points; the solid line shows the fit. The difference curve (fit error) is plotted below the spectrum. Note, in the figure, "Iobs." denotes measured scattering data and "Icalc." refers to the fit.
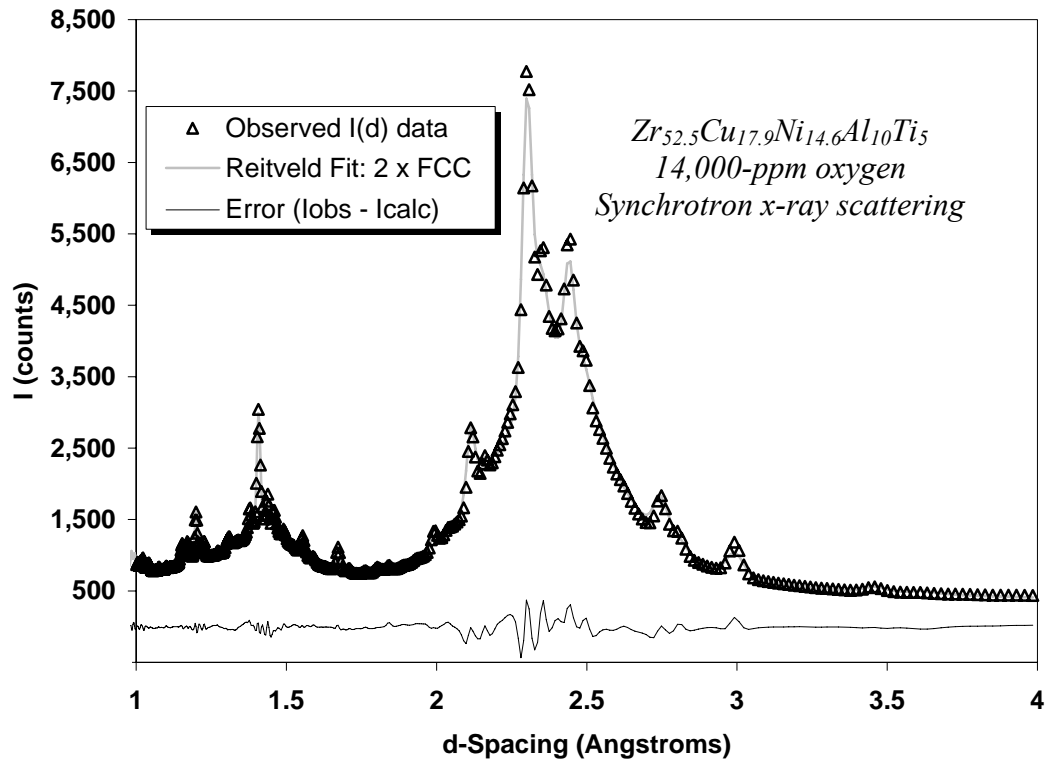
Figure 6.4   Rietveld fit of the integrated *I(d)* spectrum for the as-cast sample containing 14,000-ppm oxygen. The open triangles indicate the measured data points; the solid line shows the fit. The difference curve (fit error) is plotted below the spectrum. The difference curve (fit error) is plotted below the spectrum. Note, in the figure, "Iobs." denotes measured scattering data and "Icalc." refers to the fit.
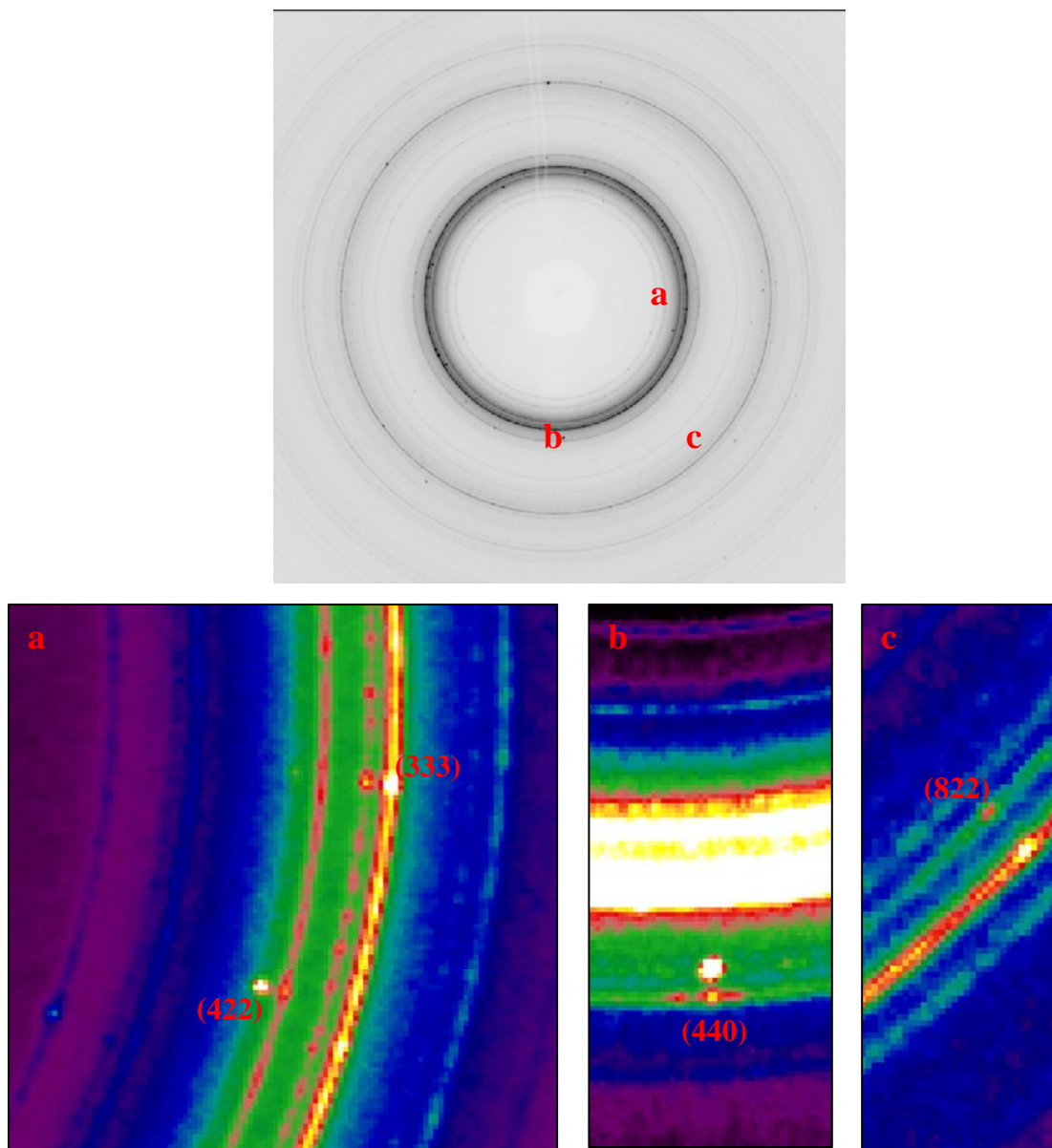
Figure 6.5   Examples of coupled Laue diffraction spots in the 4th-quadrant-scattering pattern of the as-cast 14,000-ppm oxygen-containing sample. The top image is the full Debye pattern for reference. The regions denoted "a", "b", and "c" were enlarged, and the intensity scales were reconfigured to highlight the coupled diffraction spots. The pairing of Laue spots along a radial projection from the center is indicative of oriented crystalline agglomerates formed by heterogeneous nucleation.

The in-situ beamline aerodynamic-levitation experiments were performed to characterize oxygen-stabilized intermetallic phases present in the superheated-liquid state. The 14,000-ppm-oxygen-containing sample was melted and held at $T = 1,320 \pm 40°C$. The levitated melt was stable for several seconds and, then, became unstable and partially solidified. The destabilization was indicative of reoxidation from the sample surface, which resulted in the immediate formation of a large amount of an oxygen-stabilized intermetallic at the sample apparent temperature. Fitting of the diffraction patterns of the partially-solidified sample at $T = 1,320 \pm 40°C$ showed that the oxygen-stabilized phase was similar in structure to the tetragonal phase found in the samples containing 5,000 - 6,250-ppm O, having a constricted lattice (a = 7.35 Å, c = 6.60 Å).

The 16,000-ppm-oxygen-containing sample was doped with Er to prevent the massive reoxidation observed in the undoped sample. It was predicted that the Er_2O_3 particles formed during the sample preparation would migrate to the sample surface at temperatures above the melting point of the alloy, effectively slowing and eventually arresting the absorption of oxygen from the sample surface. The molten sample was stable at the test temperature for the duration of the experiment (5 minutes). The levitated, Er-doped sample at $T = 1,595 \pm 60°C$ was found to contain an FCC phase during an isothermal hold period of approximately 3 minutes. After this period, the oxygen-stabilized cubic phase dissolved. A diffraction pattern taken after ~ 5 minutes during the isothermal hold showed a liquid structure with weak Bragg scattering from Er_2O_3 crystallites. Fitting of the integrated-scattering pattern indicated that the phase present from 1 - 3 minutes was FCC, and structurally very similar to the coexisting FCC phases observed in the as-cast sample containing 1.4 at. % oxygen, having a lattice

parameter of a = 12.25 Å. The observed $S(Q)$ patterns for the time-resolved levitation measurements are shown in Figs. 6.6 & 6.7.

6.4   Discussion

The existence of a tetragonal phase, similar in structure to that in the as-cast samples, was found at T = 1,320 ± 40˚C in the presence of large amounts of oxygen. The presence of the tetragonal intermetallic was exacerbated during the aerodynamic levitation of the undoped sample by the uptake of oxygen from the sample surface. The ability of Zr-based BMGs to form oxygen-stabilized intermetallics in the superheated-liquid state allows them to imbibe oxygen from their surfaces, resulting in heterogeneous nucleation at shallow undercooling during processing. This reoxidation can be avoided by the addition of small amounts of Er. The mechanism of the Er dopant to stabilize the liquid is twofold: first, it acts to getter the oxygen in solution, forming a stable oxide in the melt. Second, the newly-formed oxide migrates to the surface of the melt, forming a scale and, thus, inhibiting further oxygen uptake. Furthermore, the Er oxide is benign to the heterogeneous nucleation of the undercooled liquid, as shown in a previous study [81].

The oxygen-containing tetragonal intermetallic would readily catalyze the formation of the tetragonal phase found in the as-cast samples containing 6,250 and 5,000 ppm oxygen, per the *nucleation catalysis* criteria of Turnbull and Vonnegut [39]. As such, it seems that the presence of the oxygen-stabilized tetragonal phase was directly responsible for their crystallization during casting.
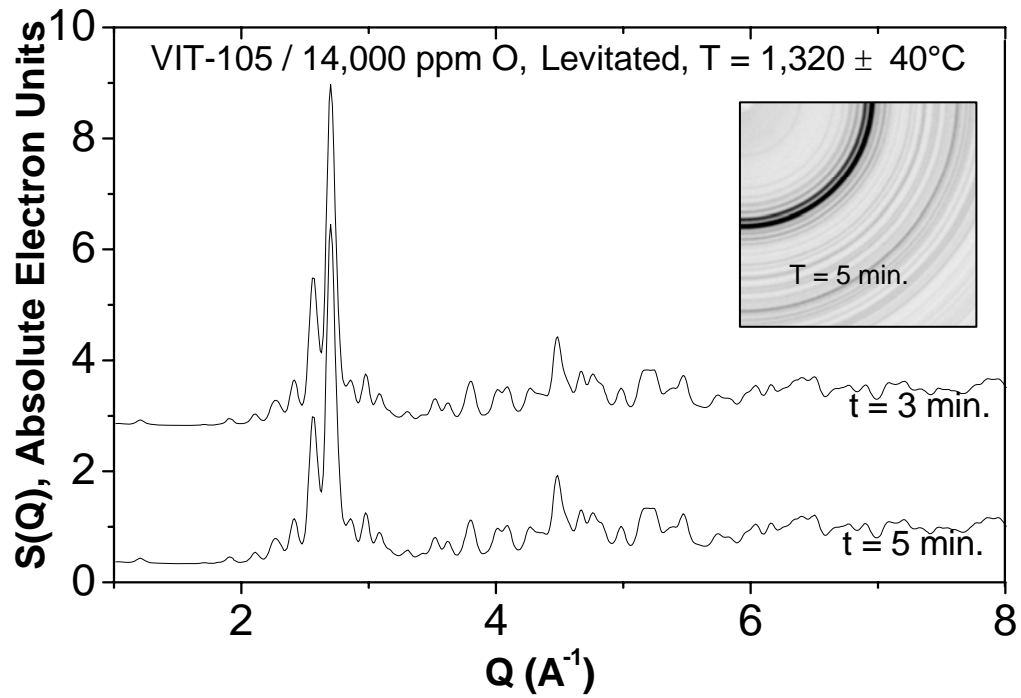
Figure 6.6   *S(Q)* curves of the in-situ SXRD data taken at t = 3 minutes and t = 5 minutes after heating to T = 1,320 ± 40°C under containerless-aerodynamic-levitation conditions showing strong diffraction from tetragonal oxygen-stabilized intermetallics.
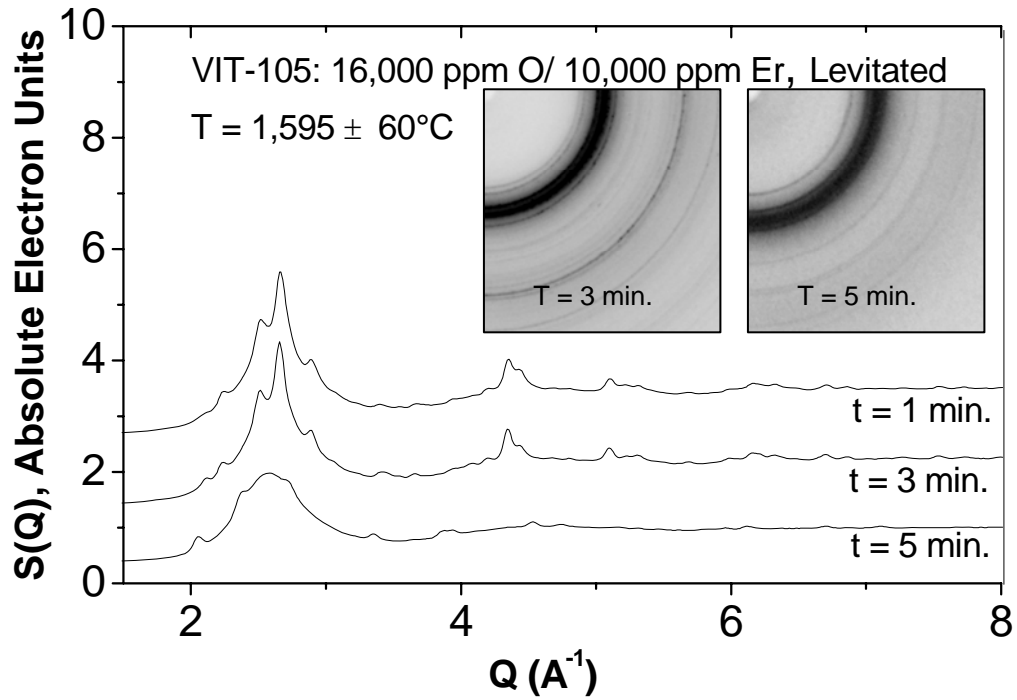
Figure 6.7 *S(Q)* curves of the Er-doped sample after heating to $T_a = 1,595 \pm 60°C$. Note the dissolution of the oxygen-stabilized intermetallic particles into the superheated liquid at t > 3 minutes. Er_2O_3 particles, formed during the sample preparation, migrated to the sample surface, blocking reoxidation. The weak Bragg diffraction peaks in the liquid-diffraction pattern are from Er_2O_3. Corresponding 4th-quadrant-Debye patterns are inset.

The highest levels of oxygen in the alloy facilitated the retention of a cubic structure after casting, showing [FCC]:[FCC] particles formed through catalyst-product epitaxy, but without a massive transformation of the amorphous material. This incomplete transformation was probably due to a very low thermodynamic driving force for the nucleation of the FCC Zr_2Ni phase at shallow undercooling.

An oxygen-stabilized FCC-catalyst phase was found to exist at $T = 1,595 \pm 60°C$ in the Er-doped sample during an isothermal hold period of $\sim$ 3 minutes, after which point it dissolved, leaving the oxygen to react with Er. The oxygen-stabilized FCC phase would not be a likely catalyst for the heterogeneous nucleation of the equilibrium tetragonal $CuZr_2$ or $NiZr_2$ phases, or the primitive tetragonal phase formed in the samples containing 5,000-ppm and 6,250-ppm O. Thus, the FCC phase is not likely to directly catalyze the tetragonal phase during recalescense. The in-situ experiment revealed the presence of an FCC intermetallic in the superheated-liquid state, but the majority of the oxygen would have been gettered in the sample by Er. As such, the exact mechanism for the formation of the FCC + FCC + amorphous structure in the as-cast sample containing 14,000-ppm oxygen is not understood at present.

6.5   Conclusion

The heterogeneous nucleation of intermetallic phases due to the presence of oxygen was studied using ex-situ and in-situ synchrotron x-ray scattering in as-cast and aerodynamically-levitated samples, respectively. The as-cast samples containing 5000 - 6,250 ppm oxygen nucleated (primarily) a primitive tetragonal intermetallic phase during

casting. Ths sample containing 14,000 ppm oxygen solidified into coexisting FCC phases by catalyst:product epitaxy. Oxygen-stabilized intermetallic precursory phases were found in the superheated-liquid state of VIT-105. Furthermore, the addition of a small amount of erbium was found to inhibit surface reoxidation in the alloy.

Chapter 7: An Electrostatic-Levitation Investigation of Nucleation in VIT-105

The current chapter presents the final experimental investigation included in this dissertation. This study was a microgravity investigation in which the heterogeneous nucleation in the VIT-105 alloy was explored. The results from this investigation are consistent with those presented in the previous chapter (Chapter 6). Note that the specific goals of this study were to examine the effects of oxygen and sample thermal history on heterogeneous nucleation. This work has been assembled into a manuscript for submission to a yet to be determined peer-reviewed journal.

J. J. Wall, C. T. Liu, W-K Rhim, J. J. Z. Li, P. K. Liaw, H. Choo, and W. L. Johnson, "A Model for Nucleation in a Zr-Based Bulk-Metallic Glass," **to be designated**.

7.1   Introduction

Bulk-metallic glasses (BMGs) are a relatively new class of materials that have been studied with steadily growing interest since their discovery about 30 years ago [2]. The materials exhibit a number of interesting physical properties, such as high strengths (up to 5 GPa in a recently discovered Co-based system [8]) and high elastic strains to failure [53]. In addition, the configurational stability of glass-forming alloys in the undercooled-liquid state make them good candidate materials to study nucleation.

It is well known that Zr-based BMGs are inherently susceptible to oxygen contamination. Oxygen may be introduced into the materials if impure elemental-starting

materials are used or by a contaminated processing environment. In general, the presence of oxygen is undesirable in Zr-based BMGs, as it results in a reduction of the glass-forming ability (GFA), leading to crystallization during cooling from the liquid state. A number of recent studies have shown that a metastable FCC phase forms in a variety of Zr-based BMG-forming alloys upon reheating in the presence of oxygen [88, 91, 100, 101].

Electrostatic levitation (ESL) provides an ideal environment in which to observe nucleation and melting, as it decouples the sample from extrinsic heterogeneous nucleation sites. As such, nucleation is governed solely by processes intrinsic to the sample. Previous electrostatic-levitation studies have identified an overheating threshold in Zr-based BMGs, which is a superheating temperature, T_{thr}, that must be exceeded prior to cooling or the materials crystallize at shallow undercooling. This threshold temperature is systematically dependant on the oxygen concentration of the alloy. In this study, we present new results to further define the mechanisms of the nucleation of intermetallics in the BMG-forming alloy VIT-105 ($Zr_{52.5}Cu_{17.9}Ni_{14.6}Al_{10}Ti_5$).

7.2   Experimental

The samples used for this study were extracted from two separate heats, one produced using high-purity elemental charge materials (Zr purity > 99.9%), and the other produced using commercial-grade materials (Zr purity > 99.0%). Wet chemical analyses revealed that the high-purity alloy (PA) had an oxygen concentration of 560 ppm (*atomic herein*), and the lower-purity alloy (CA) had an oxygen concentration of 3,000 ppm.

Note that these heats are the same material as those used by Liu et al. in a previous study [35]. 50-mg extractions from the CA and PA heats were arc-melted on a water-cooled Cu plate, forming spheroids by the surface tension of the melt, which were used for the electrostatic-levitation study.

ESL was used to suspend the CA and PA spheroids, which were, subsequently, heated to the superheated-liquid state using a Nd-YAG laser. The molten, levitated samples were free-cooled by radiation into the supercooled-liquid state, at which point they crystallized. The sample temperatures were measured using a 2-color pyrometer[14]. The specific volume (V_{sp}) evolution during cooling, crystallization, and remelting was measured from CCD images of the sample periphery taken in-situ. A typical example of the $T(t)$ and $V_{sp}(t)$ profiles for a sample free-cooled from the superheated-liquid state is presented in Fig. 7.1. A comprehensive description of the levitator can be found in [67]. The threshold temperatures (T_{thr}) of each alloy were experimentally determined by heating to various temperatures and free-cooling, noting the amount of undercooling before recalescence. One of the PA samples was heated to $T = T_{thr}$ and immediately free-cooled. This sample and another PA sample (free-cooled from above T_{thr}) were removed from the levitator and characterized using neutron scattering. The neutron-scattering measurements were performed using the General Purpose Powder Diffractometer at the Intense Pulsed Neutron Source facility of Argonne National Laboratory.

---

[14] The measured temperatures were corrected for the wavelength-independent emissivity assumption. Details of the assumption can be found in [110]. The emissivity ratios for liquid Ni-75Zr presented by Krishnan et al. [103] were used to approximate those for VIT-105.
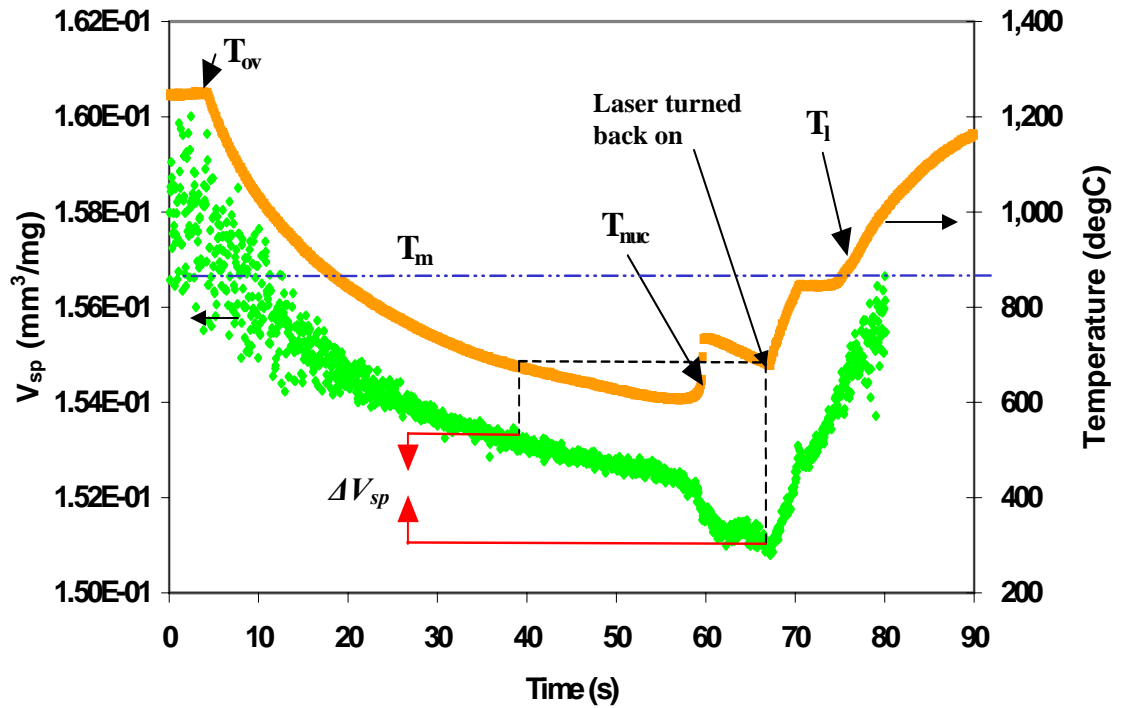
Figure 7.1 A plot of the temperature profile during free-cooling and that of the corresponding specific volume. Note the features of interest: T_l is the liquidus temperature, T_{ov} is the overheating temperature, T_{nuc} is the nucleation temprature, and ΔV_{sp} is the specific-volume change due to crystallization.

7.3   Results

Figure 7.2 shows a plot of the data points corresponding to the overheating threshold temperatures, T_{thr}, and their respective nucleation temperatures, T_{nuc}, for the PA and CA VIT-105 alloys containing varying amounts of oxygen. The values obtained by Lin et al. [7] for VIT-105 containing varying amounts of oxygen are included in the figure. The subscripts, *"1"* and *"2"*, for T_{nuc} indicate free cooling from above and below T_{thr}, respectively. Note how both T_{thr} and T_{nuc1} are systematically dependant on the oxygen content, while T_{nuc2} is invariant. It must be noted here that the values of T_{thr} obtained in the current study are higher than those of the previous study. The reason for this discrepancy is unclear at the present time.

A comparison of the $V_{sp}(T)$ behavior of the PA and CA alloy revealed that the alloys exhibit varying degrees of volume hysteresis above the eutectic temperature, Figs. 7.3 & 7.4. This hysteresis indicates that an intermetallic phase remains in the melt at temperatures above what would constitute the liquidus in an ideally-pure sample (T_l^*). The persistent intermetallic phase is, then, oxygen stabilized, which is evident from the relative magnitudes of the hysteresis observed in the CA alloy (590-ppm O) and the PA alloy (3,000-ppm O). As such, this oxygen-stabilized intermetallic phase is believed to be directly responsible for T_{thr}. Under this scenario, at T_l^*, a majority of the eutectic phase melts, but rather than going into solution, the oxygen in the sample interstitially stabilizes an intermetallic phase (Type 1, herein), which is a structural analogue to a eutectic phase. Further heating requires the oxygen to concentrate in the Type-1 phase,
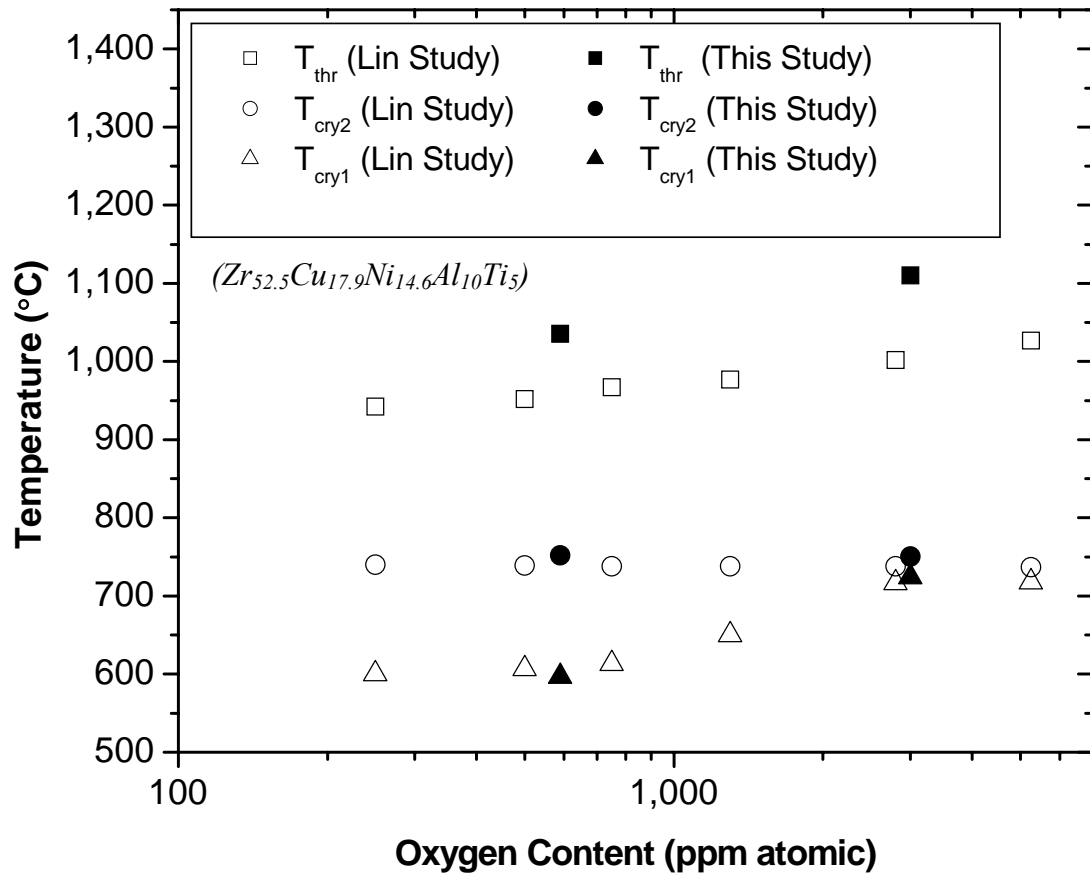
Figure 7.2 The initial temperature threshold for maximum undercooling, T_{thr}, crystallization temperature for samples free cooled from below the threshold temperature, T_{cry2}, and crystallization temperature for samples free cooled from above the threshold temperature, T_{cry1} versus respective oxygen content in VIT-105 samples. The data from the current study is plotted with that from the study conducted by Lin et al. [7].
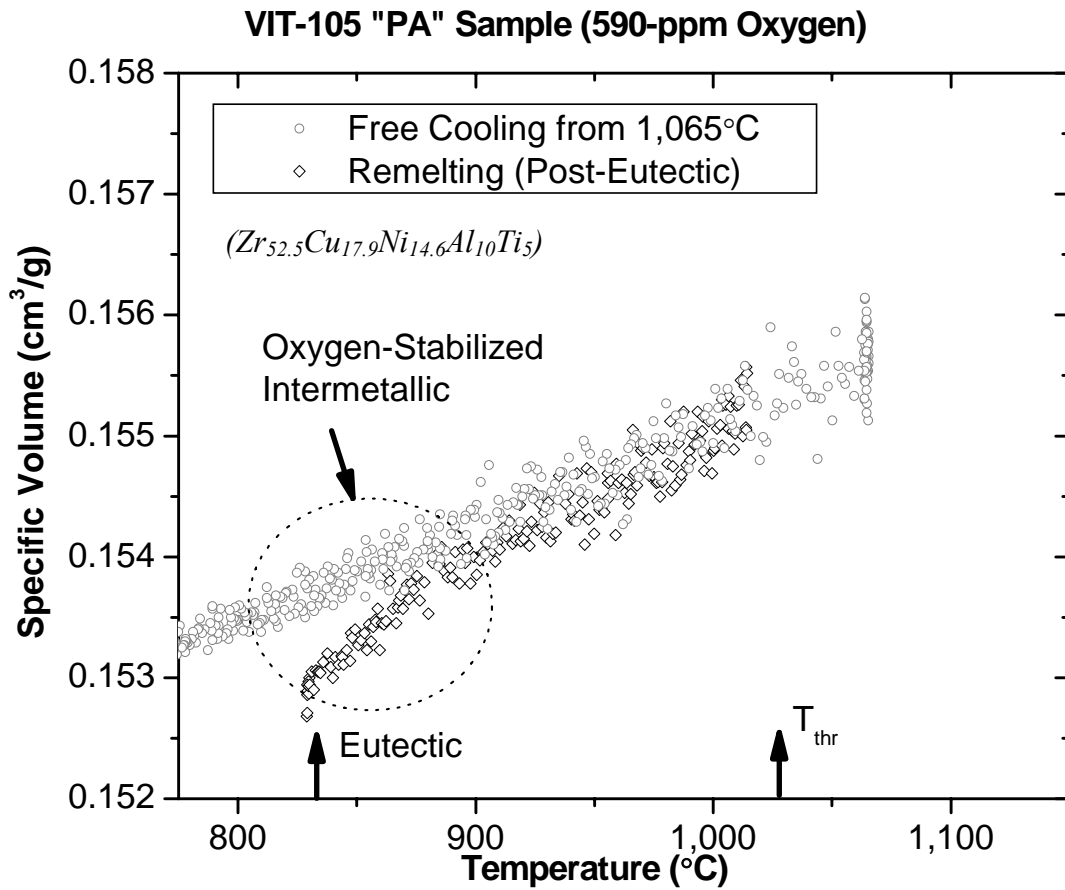
Figure 7.3   Temperature dependence of the specific volume during free-cooling and subsequent remelting of the VIT-105 PA sample cooled from above T_{thr}.

VIT-105 "CA" Sample (3,000-ppm Oxygen)

- Free Cooling from 1,150°C
- Remelting (Post-Eutectic)

$(Zr_{52.5}Cu_{17.9}Ni_{14.6}Al_{10}Ti_5)$

Oxygen-Stabilized Intermetallic

Eutectic

T_{thr}
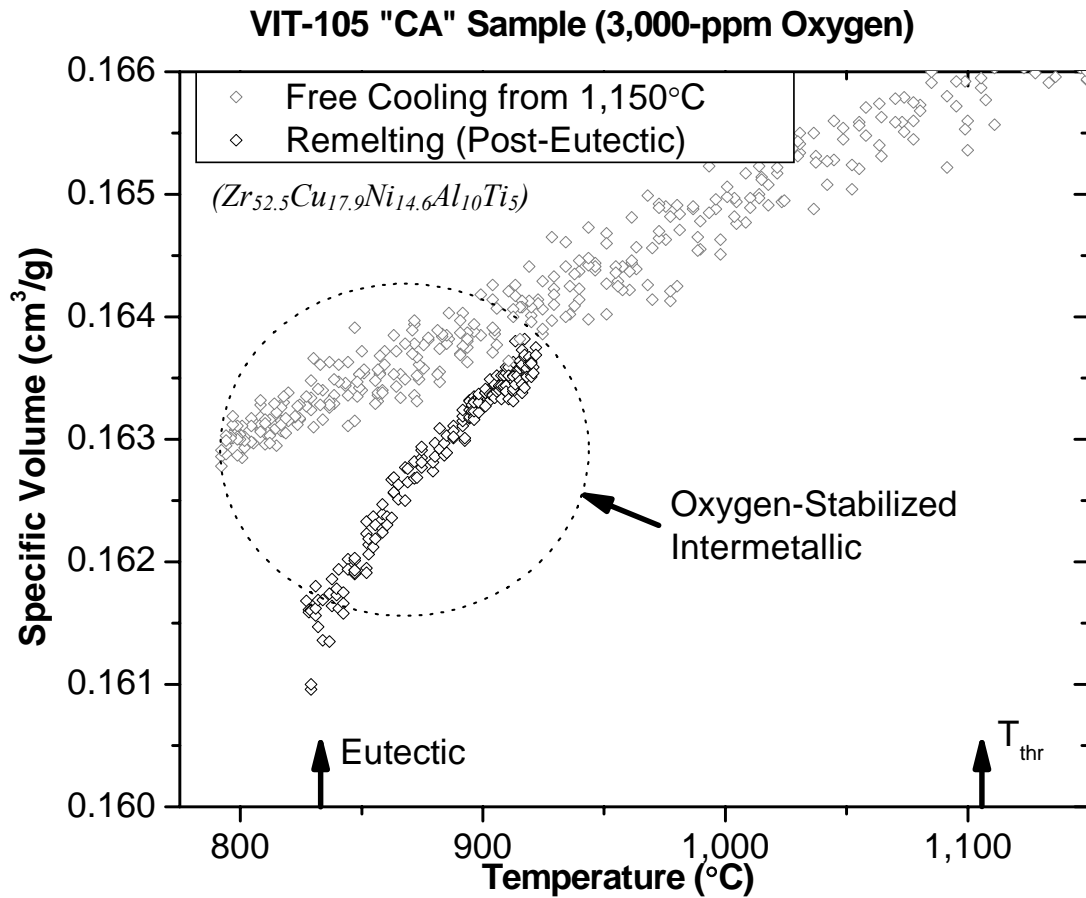
Figure 7.4   Temperature dependence of the specific volume during free-cooling and subsequent remelting for the CA alloy. Note the effect of oxygen on the magnitude of the hysteresis of V_{sp} after the eutectic transformation, as compared to the CA alloy presented in Fig. 7.3.

whereby reducing its net volume fraction with increasing temperature. At some level of superheating (corresponding to T_{thr}), the oxygen concentration within the Type-1 particles becomes too high for the structure to exist stably, and they transform into a different oxygen-stabilized intermetallic phase (Type 2, herein), which is structurally dissimilar to the eutectic phase. Note that if the oxygen-stabilized (eutectic-like) Type-1 phase were to melt into solution at T_{thr}, it would reform upon cooling below T_{thr}. To investigate the above mechanism in high-purity VIT-105, we shall further examine the PA alloy.

Three distinct crystallization modes were observed in the PA alloy during free-cooling, dependant on the applied thermal history in the superheated-liquid state: 1) an isothermal hold above T_{thr}, 2) an isothermal hold below T_{thr}, and 3) rapid heating to T_{thr} and immediately free-cooling. Plots of $V_{sp}(T)$ during free-cooling, crystallization, and reheating are presented for Cases 1 - 3 in Figs. 7.5, 7.6, and 7.7, respectively. Cases 1 and 2 showed exothermic crystallization at deep and shallow undercoolings, respectively, which is consistent with Fig. 7.2. In these cases, crystallization corresponds to a net decrease in the specific volume as the samples decrease their configurational entropy. In Case 3, where the sample was heated to T_{thr} and immediately free-cooled, the sample dilated during solidification. This dilation suggests that the transformation at T_{thr} involves an intermediate phase, which has a relatively open crystallographic structure, and catalyzes the formation of a nonequilibrium low-density intermetallic during undercooling.

VIT-105 "PA" Sample (590-ppm Oxygen): Case 1

Legend:
- ○ Free Cooling from 1,065°C
- □ Crystallization/Cooling
- △ Reheating of the Solid
- ◇ Eutectic & Remelting

$(Zr_{52.5}Cu_{17.9}Ni_{14.6}Al_{10}Ti_5)$

Crystallization

Eutectic Transformation

T_{thr}

Axis labels: Specific Volume (cm³/g); Temperature (°C)
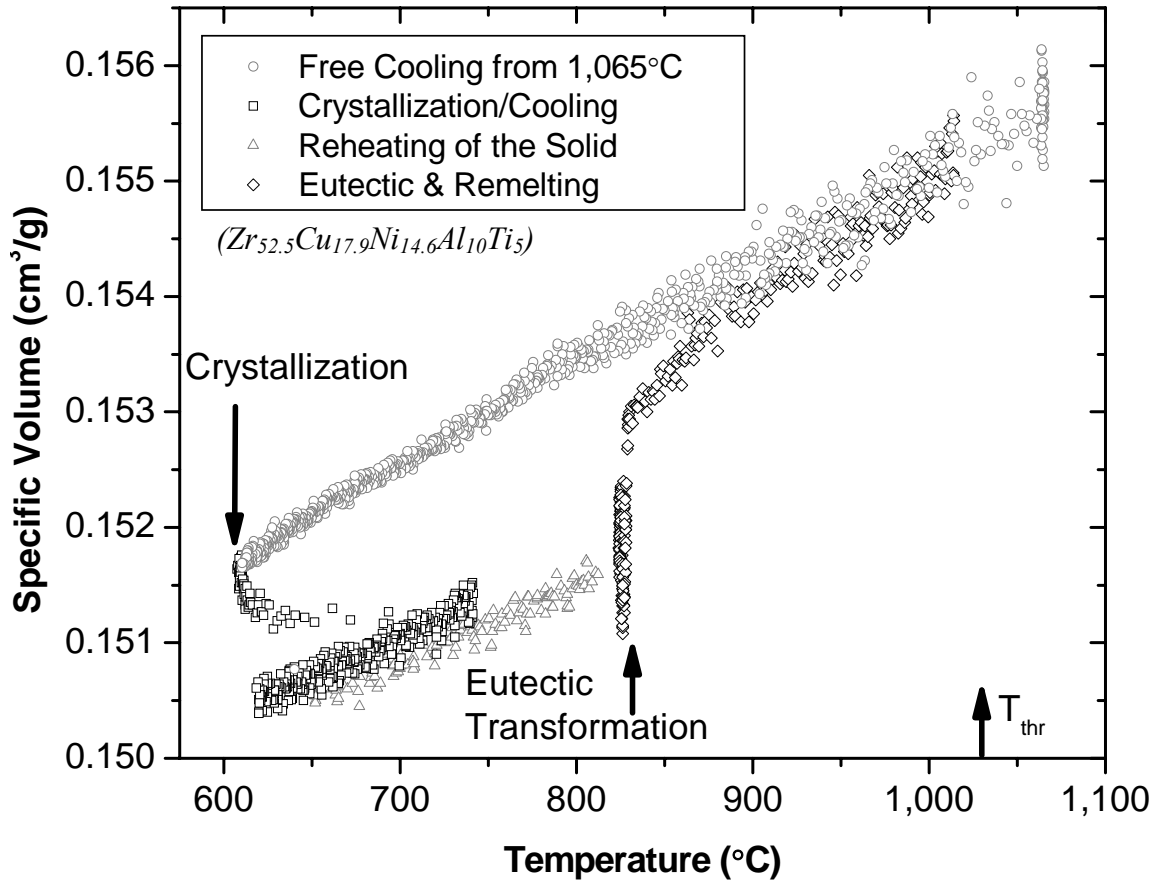
Figure 7.5 The $V_{sp}(T)$ of the PA alloy during a solidification-remelting cycle with an initial sample temperature of $T > T_{thr}$ in the ESL before free cooling. Note that the data points in the figure correspond to the full range of those presented in Fig. 7.3(a).

113

VIT-105 "PA" Sample (590-ppm Oxygen): Case 2

Legend:
- ○ Free Cooling from 965°C
- □ Crystallization/Cooling
- △ Reheating of the Solid
- ◇ Eutectic & Remelting

$(Zr_{52.5}Cu_{17.9}Ni_{14.6}Al_{10}Ti_5)$

Crystallization

Eutectic Transformation

T_{thr}

Y-axis: **Specific Volume (cm³/g)**
X-axis: **Temperature (°C)**
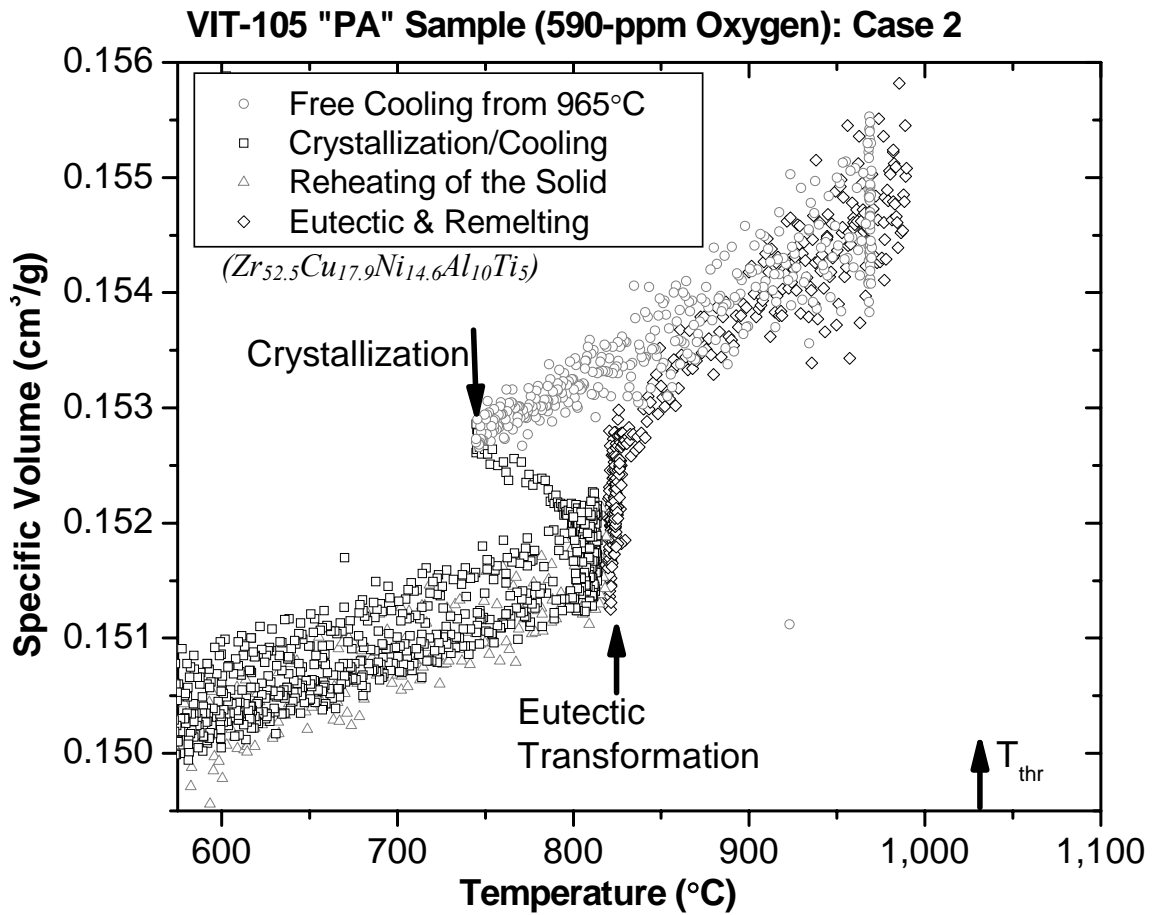
Figure 7.6   The $V_{sp}(T)$ behavior during a solidification-remelting cycle of a PA-alloy sample with an initial temperature of $T < T_{thr}$ before free-cooling.
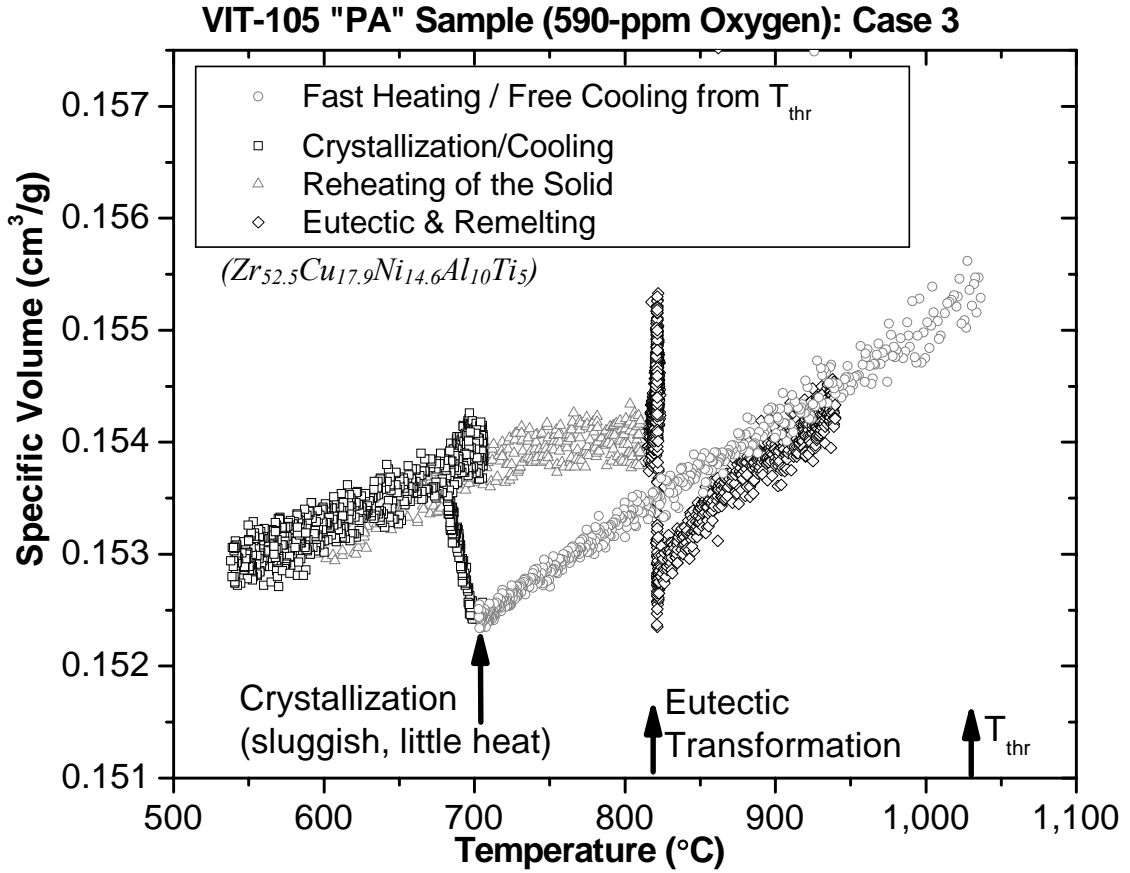
Figure 7.7 The $V_{sp}(T)$ behavior during a solidification-remelting cycle for a PA sample heated rapidly to T_{thr} and immediately free-cooled. Note the expansion of the sample during crystallization.

The neutron-diffraction measurements showed that the phases formed during recalescense in the PA-alloy samples cooled from above T_{thr} (Case 1) and heated rapidly to T_{thr}, then immediately free-cooled (Case 3), were different. The Case-3 ($+ \Delta V_{sp}$) sample diffraction pattern was fit with coexisting tetragonal phases. Least squares refinement of the Rietveld fit revealed that these phases were P4$_2$/mnm with $a = 7.41$ Å and $c = 6.66$ Å, and I4/mmm with $a = 3.20$ Å and $c = 11.10$ Å. The fit diffraction pattern is shown in Fig. 7.8. The Case-1 sample diffraction pattern showed broad diffraction peaks of low intensity, as compared to that of the Case-3 sample. Efforts to fit the Bragg peaks for the Case-1 sample diffraction pattern using the Reitveld method were unsuccessful due to the weak character of the diffraction, Fig. 7.9. By a comparison of the peak positions, it can be stated that the phases that formed in each of the PA samples were different. Indexing of the peak positions revealed that the primary crystalline component in the Case-1 sample was most likely tetragonal Zr$_2$Ni, which is a eutectic phase. The peak positions of the Zr$_2$Ni phase are denoted in Fig. 7.9. Note the relative peak widths suggest that the phase(s) formed in the Case-1 sample were nano-sized.

7.4   Discussion

After remelting, at temperatures below T_{thr}, oxygen acts to stabilize the tetragonal Zr$_2$Ni eutectic phase in the superheated-liquid VIT-105. As such, both the PA and CA alloy contained an oxygen-stabilized eutectic nucleation-catalyst at $T_l^* < T < T_{thr}$. This claim is supported by the oxygen-concentration independence of T_{nuc}, when cooling from $T < T_{thr}$.

116
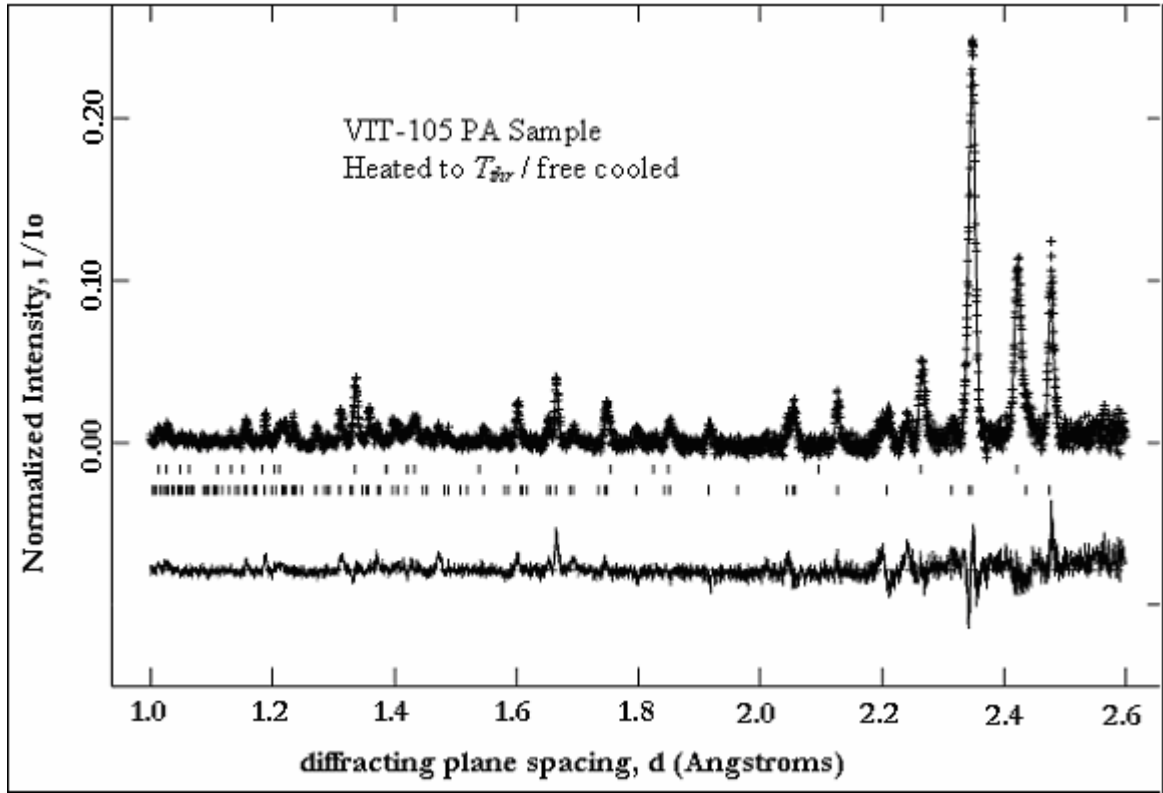
Figure 7.8 Rietveld-fit of the Case-3 sample neutron diffraction pattern. The "+" marks are the measured data, the solid line is the fit, and below is the difference curve. Note that the intensity errors were probably due to the small sample and relatively large crystallites.
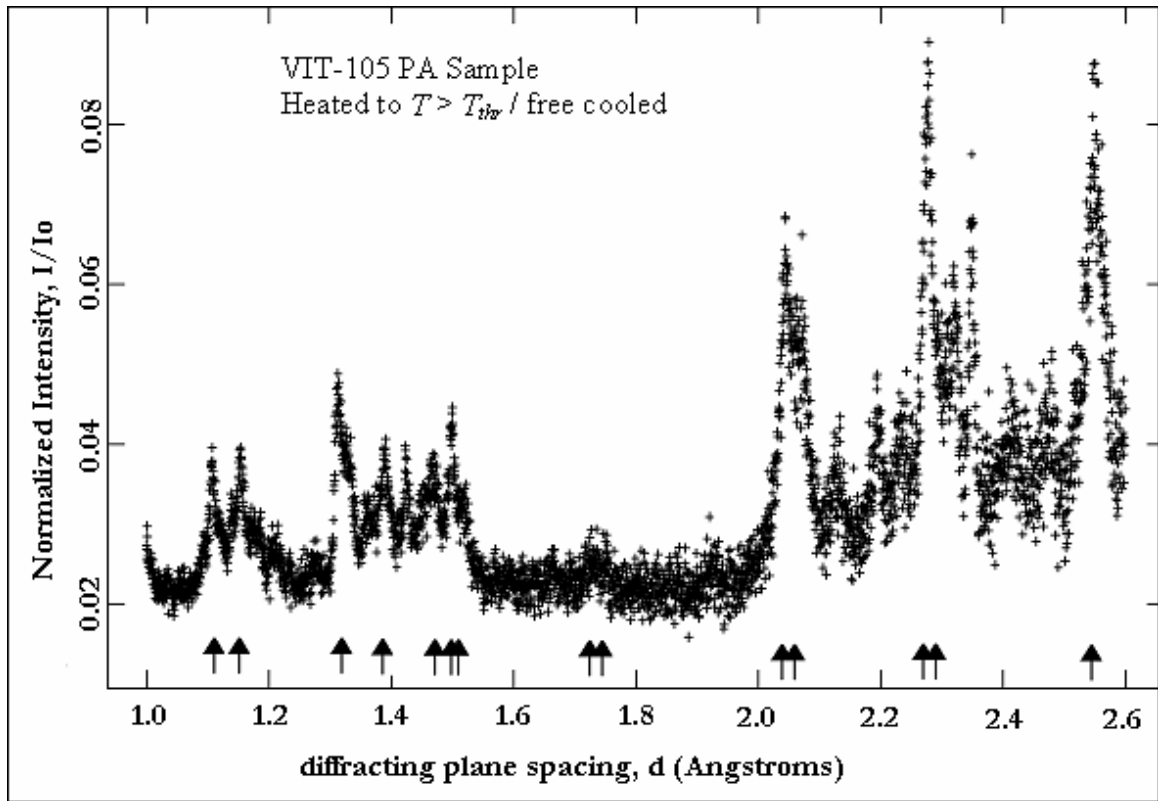
Figure 7.9   Neutron *I(d)* scattering pattern of the Case-1 sample (unfit). The "+" marks are the measured data. The arrows correspond to the tetragonal Zr_2Ni peak positions. Note the intensity, positions, and widths of the peaks relative to those in Fig. 7.8.

T_{thr}, then, corresponds to the transformation of the oxygen-stabilized tetragonal Zr_2Ni phase. At T_{thr}, in a high-purity alloy, an unstable primitive tetragonal phase forms, which either melts or, as we will assume here, decomposes into a Type-2-oxygen-stabilized intermetallic. It seems plausible that the Type-2-oxygen-stabilized intermetallic phase is a structural analogue to FCC Zr_2Ni, which is known to be stabilized by oxygen at high temperatures [89, 109], and has been reported to form in devitrified Zr-based BMGs containing oxygen. The observed increase in V_{sp} in the Case-3 PA alloy during solidification was unexpected. Shen et al. [111] reported a volume increase during reheating of the $Pd_{40}Cu_{40}Ni_{20}$ glass-forming alloy, and it was stated at the time that it was the only known glass-forming alloy to expand upon crystallization. The formation of the primitive tetragonal phase at T_{thr} may, then, account for the irreversibility of the (Type-1) - (Type-2) transformation. The formation of the unstable primitive tetragonal phase at T_{thr} indicates that the oxygen-stabilized Type-1 phase occupies a saddle point in the Gibbs free energy. Thus, the Type-1 phase is inherently metastable in the superheated liquid for samples containing low amounts of oxygen. As such, T_{thr} corresponds to an activation energy for the transformation of the oxygen-stabilized "eutectic-like" phase into the structurally-dissimilar Type-2 phase. As oxygen lowers the density of the liquid, above some nominal oxygen concentration, the primitive tetragonal oxygen-stabilized phase becomes stable above T_{thr}, and acts as a catalyst for heterogeneous nucleation at relatively shallow undercooling.

7.4   Conclusion

Heterogeneous nucleation in the $Zr_{52.5}Cu_{17.9}Ni_{14.6}Al_{10}Ti_5$ composition produced using high-purity and commercial-purity elemental materials was studied using ESL. The PA samples exhibited lower threshold temperatures and deeper maximum undercoolings than the CA samples. The PA sample was found to expand during solidification when cooling from $T = T_o$ due to the formation of a nonequilibrium tetragonal phase via heterogeneous nucleation. The experimental observations revealed some of the mechanisms that govern heterogeneous nucleation. The results strengthen and elaborate upon the mechanism for oxygen-induced nucleation presented in Chapter 6.

Chapter 8: Conclusions of the Research

A number of results were obtained through this research. The respective contribution of each result to the field of BMG-processing science remains to be seen. However, at the very least, the research as a whole and the associated journal papers will benefit the scientific community by adding to the body of the experimental and analytical work available to scientists. The results of this research are summarized as follows.

1. A combined drop/suction-casting machine was developed for the research presented in this dissertation as well as that of other students, post-docs, and faculty in the UT MSE department. The tooling and vacuum system were custom designed and retrofitted to a Materials Research Furnaces model ABJ-900 commercially available arc-melting furnace. The machine has been shown to offer relatively fast changeover times in both drop- and suction-casting operational modes, as compared with previous standalone designs. The capacity of the design presented in Chapter 3 to produce BMG materials was proven experimentally using the VIT-105 composition by drop-casting or suction-casting ingots into three separate geometries. This machine currently resides in the NSF International Materials Institutes (IMI) laboratory and has generated materials for the studies catalogued in this dissertation, as well as a number of others by other students and post-doctoral research staff.

2.   As presented in Chapter 4, a bulk-metallic-glass-forming alloy, $Zr_{57}Ti_5Ni_8Cu_{20}Al_{10}$, was processed in a containerless environment at cooling rates of $69 - 1.2$ K/s, using aerodynamic levitation. The experimentally-measured critical-cooling rate for this composition was found to be 10 ± 1 K/s. The vitrification above the critical-cooling rate was observed by tracking the time-temperature behavior of the cooling samples and confirmed by XRD. This study has shown that aerodynamic-levitation processing is a useful method to study the vitrification and solidification in glass-forming alloy systems over a relatively wide range of cooling rates, as compared to other containerless-processing methods. This set of experiments served as a "proof of concept" for the in-situ diffraction study presented in Chapter 6.

3.   Chapter 5 reported on the formation of $Zr_{52.5}Cu_{17.9}Ni_{14.6}Al_{10}Ti_5$ BMG matrix composites with oxygen concentrations of up to 1.6 at.% by doping with erbium. This Er-dopant stabilized the liquid structure by reacting with the oxygen and Al atoms, while the alloy was in the liquid state, during processing, by the formation of $(Er, Al)_2O_3$ anticatalyst particles in lieu of cubic-oxide particles, which catalyze the nucleation of FCC $NiZr_2$. The rare-earth aluminate particles did not trigger the heterogeneous nucleation of intermetallics in the undercooled alloy due to their structural dissimilarity with the competing eutectic phases. The particle morphologies were dependent on the oxygen concentration, evolving from cube-like inclusions to a simple dendritic "star-like" morphology. It was found that neither Er nor oxygen content affected the thermal stability of the as-cast Er-

doped specimens. However, overdoping with Er seemed to lead to a weak destabilization of the glass upon reheating. The compressive rupture strength was found to be approximately invariant in the as-cast composites regardless of the Er/O content. In addition, we note that due to the very high chemical affinity of Er for O, this method should easily be applicable to other glass-forming compositions.

3.   Chapter 6 presents the results from a study of the heterogeneous nucleation of intermetallic phases due to the presence of oxygen. This nucleation mechanism was studied using ex-situ and in-situ synchrotron x-ray scattering in as-cast and aerodynamically-levitated samples, respectively. The as-cast samples containing 5,000 - 6,250 ppm oxygen nucleated (primarily) a primitive tetragonal intermetallic phase during casting. The sample containing 14,000 ppm oxygen solidified into coexisting FCC phases by catalyst:product epitaxy. Oxygen-stabilized intermetallic precursory phases were found in the superheated-liquid state of VIT-105. Furthermore, the addition of a small amount of erbium was found to inhibit surface reoxidation in the alloy, consistent with the study presented in Chapter 5. The in-situ synchrotron x-ray scattering study served as a catalyst for the future collaboration with APS on similar studies with UT researchers. The scientific merit of these collaborations should become apparent in the near future.

4.   Chapter 7 presents a microgravity investigation of nucleation in a Zr-based BMG-forming alloy.   Heterogeneous nucleation in the $Zr_{52.5}Cu_{17.9}Ni_{14.6}Al_{10}Ti_5$ composition produced using high-purity and commercial-purity elemental materials was studied using ESL.   The PA samples exhibited lower threshold temperatures and deeper maximum undercoolings than the CA samples.   The PA sample was found to expand during solidification when cooling from $T = T_o$ due to the formation of a nonequilibrium tetragonal phase via heterogeneous nucleation.   The experimental observations revealed some of the mechanisms that govern heterogeneous nucleation.   The results strengthen and elaborate upon the mechanism for oxygen-induced nucleation presented in Chapter 6.

In summary, the research conducted through the pursuit of this Ph.D. has yielded a versatile machine to process BMG materials by drop- and suction-casting.   A new processing method, aerodynamic levitation, was used to produce a Zr-based BMG and probe the supercooled-liquid state.   A new doping scheme was introduced to allow the retention of a glass in the VIT-105 BMG-forming alloy containing up to 1.6 at.% oxygen. In-situ beam-line aerodynamic levitation as well as electrostatic levitation were used to characterize the mechanisms responsible for the destruction of the glass-forming ability in the VIT-105 BMG-forming alloy.

Chapter 9: Future Work

With respect to the aerodynamic-levitation study presented in Chapter 4: It was shown that aerodynamic levitation is a viable method to process BMG-forming alloys and directly observe the glass transition. Furthermore, the method can be used to directly measure the critical cooling rates. Future work should extend these capabilities to measure time-temperature-transformation curves for a multitude of other glass-forming alloys. The measurements can be made quickly and efficiently, as compared to other containerless-processing techniques.

With respect to the Er-doping study presented in Chapter 5: the effect of erbium on the glass-forming ability of the VIT-105 BMG forming alloy was quite profound. It appears that the mechanism of the oxygen-induced destruction of the glass forming ability is similar to other Zr-based BMGs as well. Future studies should be conducted to determine if this doping strategy applies to the entire family of Zr-based BMG-forming alloys. The in-situ beam-line aerodynamic-levitation study presented in Chapter 6 showed that $(Er,Al)_2O_3$ is stable well above the liquidus of VIT-105 in the presence of oxygen, and acts as a nucleation anticatalyst during cooling. The effect should extend to a multitude of other alloys that do not readily nucleate crystalline phases similar in structure to that of the erbium-aluminate oxide.

With respect to the oxygen-induced nucleation studies: much work remains to be done to fully characterize the effect of oxygen on heterogeneous nucleation in Zr-based BMGs. The research work presented here is the most comprehensive study to date, and the mechanism proposed explains a number of phenomena associated with heterogeneous

nucleation, but the picture is not entirely clear. A difficulty that I found with respect to developing the mechanism is that data had to be extrapolated upon, and assumptions were made, which invariably has resulted in some degree of error. Virtually every assumption made could be quantified using beam-line electrostatic levitation. If such a facility becomes standard at a synchrotron beam-line, measurements should be made to measure the full phase diagrams of the VIT-105 alloy containing varying amounts of oxygen. In Chapter 7, using electrostatic levitation, it was determined that an oxygen-stabilized eutectic phase remains in the superheated liquid after melting. The temperature evolution of the oxygen-stabilized phase and the transformation that occurs at the threshold temperature should be quantified by direct experimental observation. Again, such a study would be made possible by in-situ beam line electrostatic levitation.

With respect to the data analysis: the Rietveld fitting of the crystalline species in a glass is rarely, if ever, done currently, and the method used for fitting the scattering from the glass in reciprocal space has not, to my knowledge, been done previously. Future studies should use this technique for phase identification. The technique is not easy to employ for a material that is primarily a glass, but if done successfully, it provides far more compelling evidence for successful phase identification than simply labeling peaks in a diffraction pattern, as is the current trend in the literature.

REFERENCES

References

1.   W. Clement, R. H. Willens, and P. Duwez, Nature **187** (1960) 869.

2.   H. S. Chen, Acta Metall. **22** (1974) 1505.

3.   H. S. Chen, J. T. Krause, and E. Coleman, J. Non-Cryst. Solids **18** (1975) 157.

4.   A. L. Drehman, A. L. Greer, and D. Turnbull, Appl. Phys. Lett. **41** (1982) 716.

5.   A. Inoue, T. Nakamura, T. Nishiyama, and T. Masumoto, Mater. Trans. JIM **33** (1993) 937.

6.   A. Pekar and W. L. Johnson, Appl. Phys. Lett. **63** (1993) 2342.

7.   X. H. Lin, W. L. Johnson, and W-K Rhim, Mater. Trans. JIM **39** (1997) 477.

8.   B. Shen, C. Chang, T. Kubota, and A. Inoue, J. Appl. Phys. **100** (2006) 013515.

9.   Z. P. Lu, C. T. Liu, J. R. Thompson, and W. D. Porter, Phys. Rev. Lett. **92** (2004) 245503.

10.   V. Ponnambalam, S. J. Poon, and G. J. Shiflet, J. Mater. Res. **19** (2004) 1320.

11.   http://www.liquidmetal.com.

12.   W. Kauzmann, Chem. Rev. **43** (1943) 219.

13.   D. A. Porter and K. E. Easterling, *Phase Transformations in Metals and Alloys - 2nd edition* (1992) **Chapman & Hall**, New York, NY.

14.   R. Busch, JOM **52** (2000) 39.

15.   D. R. Uhlmann, J. Non-Ctyst. Solids **7** (1972) 337.

16.   C. A. Angell, Science **267** (1995) 1924.

17.   K. Ito, C. T. Moynihan, and C. A. Angell, Nature **398** (1999) 492.

18.	K. L. Ngai and O. Yamamuro, J. Chem. Phys. **111** (1999) 10403.

19.	L. M. Martinez and C. A. Angell, Nature **410** (2001) 663.

20.	T. Abe, M. Shimono, K. Hashimoto, K. Hono, and H. Onodera, Scripta Mater. **55** (2006) 421.

21.	W. L. Johnson, JOM **54** (2002) 1047.

22.	S. Mukherjee, J. Schroers, Z. Zhou, W. L. Johnson, and W-K. Rhim, Acta Mater. **52** (2004) 3689.

23.	R. Busch, W. Liu, and W. L. Johnson, J. Appl. Phys. **83** (1998) 4134.

24.	R. Busch, Y. J. Kim, and W. L. Johnson, J. Appl. Phys. **77** (1995) 4134.

25.	A P Solokov, Science **273** (1996) 1675.

26.	D. Turnbull, Solid State Physics - volume 3 (1956) **Academic**, New York, NY.

27.	D Turnbull, Cont. Phys. **10** (1969) 473.

28.	P. Desre, T. Itami, and I. Ansara, Z. Metallk, **84** (1993) 185.

29.	P. Desre, T. Itami, and I. Ansara, Mater. Trans. JIM **38** (1997) 583.

30.	J. F. Loffler, Intermetallics **11** (2003) 529.

31.	M. Avrami, J. Chem. Phys. **7** (1939) 1103.

32.	M. Avrami, J. Chem. Phys. **8** (1940) 212.

33.	M. Avrami, J. Chem. Phys. **9** (1941) 177.

34.	M. A. Johnson and R. F. Mehl, Trans. AIME **135** (1939) 416.

35.	Z. P. Lu and C. T. Liu, Acta Mater. **50** (2002) 3501.

36.	A. L. Greer, Nature **366** (1993) 303.

37.	W. L. Johnson, MRS Bull. **24** (1999) 42.

38.	A. Inoue, T. Zhang, and A. Takeuchi, Mater. Sci. Forum **269-272** (1998) 855.

39.   D. Turnbull and B. Vonnegut, Ind. Eng. Chem. **44** (1952) 1292.

40.   Z. P. Lu and C. T. Liu, J. Mater. Sci. **39**:(2004) 3965.

41.   Z. P. Lu, C. T. Liu, and W. D. Porter, Appl. Phys. Lett. 83 (2003) 2581.

42.   F. Jiang, Z. J. Wang, Z. B. Zhang, and J. Sun, Scripta Mater. **53** (2005) 487.

43.   B. Zhang, M. X. Pan, D. Q. Zhao, R. J. Wang, and W. H. Wang, Mater. Trans. JIM **11** (2000) 1410.

44.   J. J. Wall, C. Fan, P. K. Liaw, C. T. Liu, and H. Choo, Rev. Sci. Instr. **77** (2006) 033902.

45.   C. Fan, P. K. Liaw, and H. Choo, Scripta Mater. **53** (2005) 1407.

46.   B. Zhang, D. Q. Zhao, M. X. Pan, W. H. Wang, and A. L. Greer, Phys. Rev. Lett. **94** (2005) 205502.

47.   W. J. Kim, Y. K. Sa, J. B. Lee, and H. G. Jeong, Intermetallics **14**:(2006) 377.

48.   S. K. Chung, W-K Rhim, D. Barber, K. F. Man, G. Gutt, A. Rulison, and R. E. Spjut, Rev. Sci. Instr. **64** (1993) 2961.

49.   H. M. Rietveld, J. Appl. Crystallogr. **2**:(1969) 65.

50.   S. Schneider, J. Phys.: Condens. Matter **13** (2001) 7723.

51.   P. W. Anderson, Science **267** (1995) 1615.

52.   L. M. Wang, W. H. Wang, L. L. Sun, J. Zhang, and W. K. Wang, Phys. Rev. B **63** (2001) 052201.

53.   C. A. Schuh and T. G. Nieh, J. Mater. Res. **19** (2004) 46.

54.   G. Y. Wang, P. K. Liaw A. Peker, B. Yang, M. L. Benson, W. Yuan, W. H. Peter, L. Huang, M. Freels, R. A. Buchanan, C. T. Liu and C. R. Brooks, Intermetallics **13** (2005) 429.

55.   C. Fan, R. T. Ott, and T. C Hufnagel, Appl. Phys. Lett. **81** (2002) 1020.

56.   A. A. Kundig, A. Dommann, W. L. Johnson, and P. J. Uggowitzer, Mater. Sci. Eng. A **375** (2004) 327.

57.   H. E. N. Stone, J. Phys. E **4** (1971) 1058.

58.   J. E. Crow and A.R. Sweedler, Rev. Sci. Instr. **44** (1973) 1398.

59.   X. Gu, L. Q. Xing, and T. C. Hufnagel, J. Non. Cryst. Solids **311** (2002) 77.

60.   A. Inoue, T. Zhang, and M. Eiichi, United States Patent 5,740,854 (1998).

61.   J. J. Wall, R. Weber J. Kim, P. K. Liaw, and H. Choo, Mater. Sci. Eng. A **445-446** (2007) 219.

62.   C. C. Hays, J. Schroers, W. L. Johnson, T. J. Rathz, R. W. Hyers, J. R. Rogers, and M. B. Robinson, Appl. Phys. Lett. **79** (2001) 1605.

63.   C. C. Hays and W. L. Johnson, J. Non-Cryst Solids **250-252** (1999) 596.

64.   R. W. Hyers, R. C. Bradshaw, J. R. Rogers, T. J. Rathz, G. W. Lee, A. K. Gangopadhyay, and K. F. Kelton, Int. J. Thermophys. **25** (2004) 1155.

65.   K. F. Kelton, G. W. Lee, A. K. Gangopadhyay, R. W. Hyers, T. J. Rathz, J. R. Rogers, M. B. Robinson, and D. S. Robinson, Phys. Rev. Lett. **90** (2004) 195504.

66.   T. J. Rathz, M. B. Robinson, R. W. Hyers, J. R. Rogers, and D. Li, J. Mater. Sci. Lett. **21** (2002) 301.

67.   G. J. Fan, M. J. Freels, H. Choo, P. K. Liaw, J. J. Z. Li, W-K Rhim, W. L. Johnson, P. Yu, and W. H. Wang, Appl. Phys. Lett. **89** (2006) 241917.

68.   G. J. Fan, J. J. Z. Li, W-K Rhim, D. C. Qiao, H. Choo, and P. K. Liaw, Appl. Phys. Lett. **88** (2006) 221909.

69.   D. Turnbull, J. Appl. Phys. **21** (1950) 1022.

70. Y. J. Kim, R. Busch, W. L. Johnson, A. J. Rulison, and W-K. Rhim, Appl. Phys. Lett. **65** (1994) 2136.

71. X. H. Lin, W. L. Johnson, and W-K. Rhim, Mater. Trans. JIM **38** (1997) 473.

72. S. Mukherjee, J. Schroers, W. L. Johnson, and W-K. Rhim, Phys. Rev. Lett. **94** (2005) 245501.

73. S. Mukherjee, H-G. Kang, W. L. Johnson, and W-K. Rhim, Physical Review B **70** (2004) 174205.

74. J. K. R. Weber, J. J. Felten, and P. C. Nordine, Rev. Sci. Instr. **67** (1996) 522.

75. J. K. R. Weber, S. Krishnan, and P. C. Nordine, JOM **43** (1991) 8.

76. J. K. R. Weber, J. G. Abadie, A. D. Hixson, P. C. Nordine, and G. A. Jerman, J. Am. Ceram. Soc. **83** (2000) 1868.

77. S. Whittaker, AIChE J. **18** (1972) 361.

78. L. Q. Xing, T. C. Hufnagel, J. Eckert, W. Löser, and L. Schultz, Appl. Phys. Lett. **77** (2000) 1970.

79. W. H. Wang, C. Dong, and C. H. Shek, Mater. Sci. Eng. R **44** (2004) 45.

80. A. S. Krishnan, J. K. R. Weber, C. D. Anderson, P. C. Nordine, W. H. Hofmeister, C. Mortin, and R. J. Bayuzick, Mater. Sci. Eng. A **219** (1996) 21.

81. J. J. Wall, C. Fan, P. K. Liaw, and H. Choo, Mat. Sci. Eng. A, In Press (2007). **DOI: 10.1016/j.msea.2007.04.025**.

82. G. Y. Wang, P. K. Liaw, A. Peker, B. Yang, M. L. Benson, W. Yuan, W. H. Peter, L. Huang, A. Freels, R. A. Buchannan, C. T. Liu, and C. R. Brooks, Intermetallics **13** (2005) 429.

83.   G. Y. Wang, P. K. Liaw, W. H. Peter, B. Yang, M. Freels, Y. Yokoyama, M. L. Benson, B. A. Green, T. A. Saleh, R. L. Mcdaniels, R. V. Steward, R. A. Buchannan, C. T. Liu, and C. R. Brooks, Intermetallics **12** (2004) 1219.

84.   G. Y. Wang, P. K. Liaw, W. H. Peter, Y. Yokoyama, M. L. Benson, B. A. Green, M. J. Kirkham, S. A. White, T. A. Saleh, R. L. Mcdaniels, R. V. Steward, R. A. Buchannan, C. T. Liu, and C. R. Brooks, Intermetallics **12** (2004) 885.

85.   W. H. Peter, P. K. Liaw, R. A. Buchannan, C. T. Liu, C. R. Brooks, J. A. Horton, C. A. Carmichael, and J. L. Wright, Intermetallics **10** (2002) 1125.

86.   Prices approximated from Alfa Aesar, Ward Hill, MA.

87.   E. J. Huber, E. L. Head, and C. E. Holley, J. Phys. Chem. **60** (1956) 1582.

88.   A. Gebert, J. Eckert, and L. Schultz, Acta Mater. **56** (1998) 5475.

89.   Z. Altounian, E. Batalla, J. O. Strom-Olsen, and J. L. Walter, J. Appl. Phys. **61** (1987) 149.

90.   A. R. Yavari, A. Le Moulec, A. Inoue, W. J. Botta, G. Vaughan, and A. Kvick, Mater. Sci. Eng. A **304-306** (2001) 34.

91.   M. F. de Oliveira, W. J. Botta, M. J. Kaufman, and C. S. Kiminami J. Non-Cryst. Sol. **304** (2002) 51.

92.   J. Eckert, A. Reger-Leonhard, B. Weiss, M. Heilmaier, and L. Schultz, Adv. Eng. Mater. **3** (2001) 41.

93.   L. Q. Xing, C. Bertrand, J. -P. Dallas, and M. Cornet, Mat. Sci. Eng. A **241** (1998) 216.

94.   A. L. Greer, Nature **368** (1994) 688.

95.   T. Kulik, J. Non-Cryst. Solids **287** (2001) 145.

96. D. V. Louzguine-Lugin and A. Inoue, J. Nanosci. Nanotechnol. **5** (2005) 999.

97. U. Köster, J. Meinhardt, S. Roos, and H. Liebertz, Appl. Phys. Lett. **69** (1996) 179.

98. J. J. Kim, Y. Choi, S. Suresh, and A. S. Argon, Science **295** (2002) 654.

99. M. Chen, A. Inoue, W. Zhang, and T. Sakurai, Phys. Rev. Lett. **96** (2006) 245502.

100. J. Saida and A. Inoue, J. Non-Cryst. Solids **317** (2003) 97.

101. U. Köster, D. Zander, and R. Janlewing, Mater. Sci. Forum **386** (2001) 89.

102. C. R. Hubbard, NIST SRM 674 Certificate of Analysis (1983).

103. S. Krishnan, J. J. Felten, J. E. Rix, J. K. R. Weber, P. C. Nordine, M. A. Beno, S. Ansell, and D. L. Price, Rev. Sci. Instr. **68** (1997) 3512.

104. B. Bitnar, W. Durisch, J.-C. Mayor, H. Sigg, and H. R. Tschudi, Sol. Energy Mater. Sol. Cells **73** (2002) 221.

105. V. Ya. Chekhovskoi, V. D. Tarasov, and N. V. Grigor'eva, High Temp. **42** (2004) 252.

106. H. P. Hammersly, ESRF International Report No. EXP/AH/93-02 (1993).

107. A. C. Larson and R. B. Von Dreele, Los Alamos National Laboratory Report LAUR 86-748 (1994).

108. E. Pekarskaya, J. F. Löffler, and W. L. Johnson, Acta Mater. **51** (2003) 4045.

109. R. Mackay, G. J. Miller, and H. F. Franzen, J. Alloys Comp. **204** (1994) 109.

110. M. A. Khan, C. Allemand, and T. A. Eagar, Rev. Sci. Instr. **62** (1991) 392.

111. T. D. Shen, U. Harms, and R. B. Schwarz, Appl. Phys. Lett. **83** (2003) 4512.

112. F. C. Frank, Proc. R. Soc. London A **215** (1952) 43.

113. C. J. Howard, J. Appl. Cryst. **15** (1982) 615.

114.   A. Le Bail, H. Duroy, and J. L. Fourquet, Mat. Res. Bul. **23** (1998) 447.

APPENDICES

Appendix A: Notes and Vendor Information

Chapter 1

- The as-cast BMG materials shown in Fig. 1.6 were produced using the casting machine described in Chapter 3.

- A number of simplifications were made in the discussion of metallurgical thermodynamics and kinetics to fit within the context of the discussion. For a comprehensive treatment of these subjects, see the appropriate texts. I recommend those by Gaskell and Balluffi (see below):

  David R. Gaskell, *Introduction to Metallurgical Thermodynamics*, available from the Hemisphere Publishing Group, LLC.

  Robert W. Balluffi, Samuel M. Allen, and W. Craig Carter, *Kinetics of Materials*, available from Wiley-Interscience.

Chapter 2

- The laboratory x-ray diffractometer (Phillips X'pert) was obtained from Phillips U.S. distributor PANalytical Inc., Natick, MA USA.

- The differential-scanning calorimeter (Diamond model) was purchased from Perkin-Elmer, Waltham, MA, USA. The samples were held using annealed aluminum pans under an Ar-gas cover.

- The scanning-electron microscopes (Hitachi S-800 and S-3200) were obtained from Hitachi High Technologies America, Inc., Pleasanton, CA, USA.

- The universal-testing machine (MTS 810) was obtained from MTS, Eden Prairie, MN, USA. The compression platens used for the compression tests were held using hydraulic grips similar to those pictured in Fig. 2.3, both of these were purchased from MTS.

- Shiva Technologies is located in Syracuse, NY, USA (http://www.shivatec.com).

- The electrostatic levitator used for the study presented in Chapter 7 was built by Dr. Won-Kyu Rhim at the NASA Jet Propulsion Laboratory of Caltech. The levitator shown in Fig. 2.4 (NASA-MSFC ESL) is of similar design. However, the Caltech ESL has a tetrahedral laser-heating system to minimize thermal gradients in the sample.

- The 1-ID and 11-ID synchrotron x-ray beam lines are available for experimental research through the Advanced Photon Source user program by proposal. The in-situ study on the 11-ID beam-line required an aerodynamic levitator. This sample

environment is non-standard at the time of this writing and, thus, not available through the user program.

- The General Purpose Powder Diffractometer neutron scattering instrument is available for experimental research through the Intense Pulsed Neutron Source user program by proposal.

- The GSAS program is freely-available software that can be accessed via the Collaborative Computational Project Number 14 (CCP14) Homepage (http://www.ccp14.ac.uk).

Chapter 3

- The arc-melter was purchased from Materials Research Furnaces, Inc. (Model ABJ-900), Suncook, NH, USA.

- The copper hearth and molds for the modified arc-melter were made by the UT machine shop. I have a full set of production drawings.

- The electropneumatic-gate valves, screw valves, and vacuum flanges were purchased from MDC Vacuum Products, LLC, Hayward, CA, USA.

- The three-dimensional models and thermal finite element analyses were done using the Pro/Engineer and Pro/Mechanica software packages, respectively. These software packages are available from the Parametric Technology Corporation, Needham, MA, USA.

- The elemental metals for the study described in Chapter 3 and the subsequent alloying studies were purchased from Alfa-Aesar, Ward Hill, MA USA.

Chapter 4

- The noise in the T(t) curves of Fig. 4.2. is primarily due to surface fluctuations on the molten sample created by the levitation gas.

Chapter 5

- The effectiveness of using the Er dopant as a means to protect against surface oxidation may be more than was stated in Chapter 5. The ability of Er to impede the oxidation was discovered in the initial stages of this study. In this stage, to gage the effectiveness of the element, in a qualitative sense, an arbitrary amount of Er was added to a heavily-oxidized ingot and melted in the arc-melter, which, at the time, was known to have a massive vacuum leak. The cast material formed a glass and a large amount of oxide particles migrated to the exterior of the uncast material in the crucible. As such, the addition of Er to even high-purity BMG

materials is likely to improve its processability significantly. Note that this account was left out of the body of Chapter 5 as it is poorly quantifiable and there is no scientific proof that it occured beyond my account. The story is included here as it is an interesting side note that could make for a more interesting future investigation.

Appendix B: Procedure for Fitting Glass Scattering

Fitting of the diffuse-scattering contribution of the amorphous material was accomplished by fitting the broad "amorphous" peaks in the spectra to reflections from a complex FCC unit cell (Fd-3m, 96 atoms) that contains strained icosahedral clusters. The FCC structure and an internally located strained icosahedral cluster are shown in Fig. B.1 (a & b). This approach to fitting scattering from the glass is a logical extension of Frank's hypothesis, which states that an undercooled liquid, and, by extension, a metallic glass, should exhibit a high degree of local icosahedral order [112]. Note that Frank's hypothesis has recently been demonstrated experimentally in multicomponent metallic liquids by Kelton et al. [65]. The peak fits used pseudo-Voigt functions modified to include asymmetry [107, 113] using the LeBail method [114], which forces the structure factor, $S(Q)$, for each reflection to match the measured data. The Lorentzian broadening-coefficient due to the particle size was increased to match observed broad-peak widths due to diffraction by the glass. In addition, the atomic strain terms were refined to allow the constrained shifting of the atoms in the structure. This method was effective in modeling the broad-scattering peaks, thus removing interference with the fits of Bragg peaks from the crystalline phases. This approach was found to be superior to a polynomial for fitting the diffracted radiation from the glass.
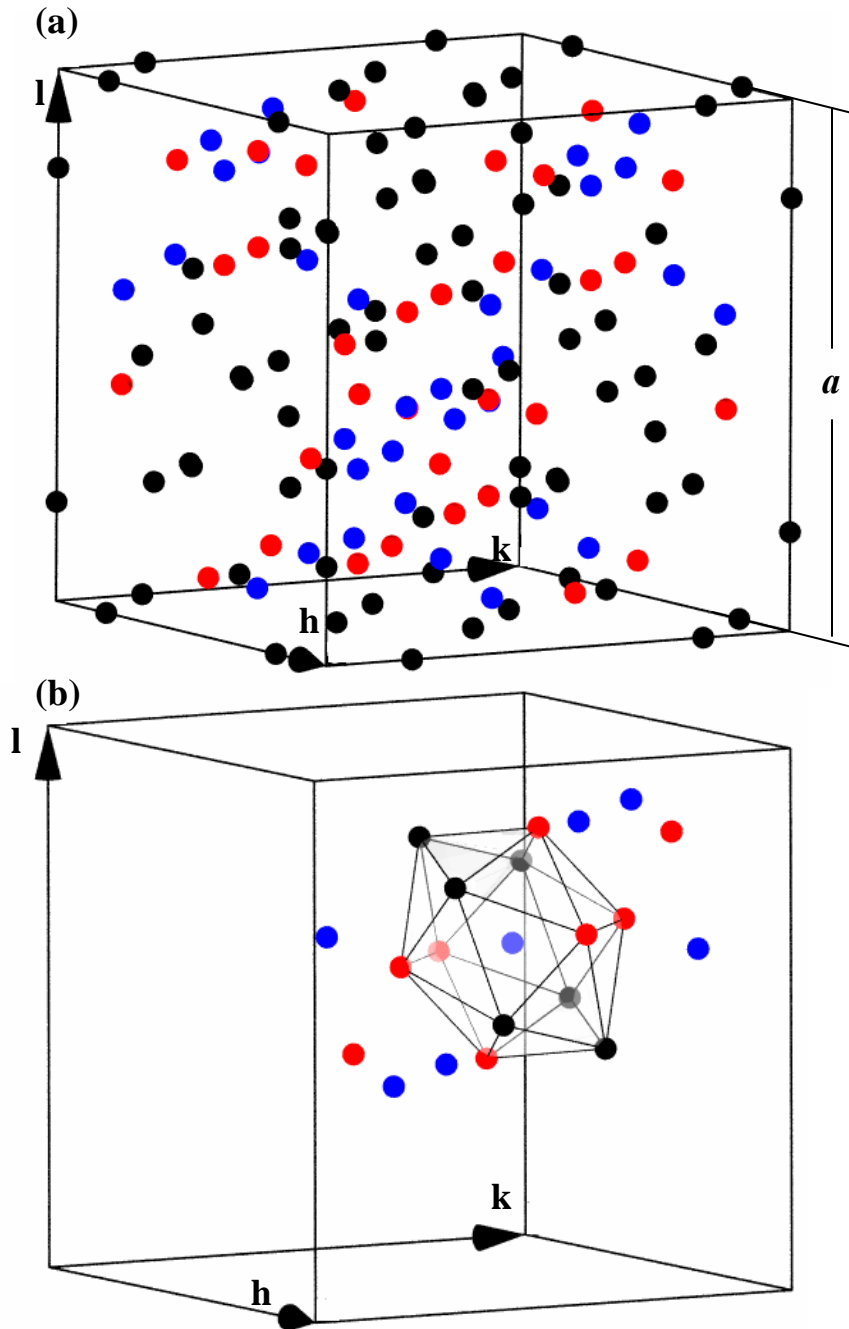
Figure B.1   (a) The 96 atom Fd–3m unit cell used as a starting structure to fit the glass scattering. The black, red, and blue dots are the 48f, 32e, and 16d Wyckoff sites, respectively.   (b) Illustrates the 13-atom-strained icosahedral configuration of neighboring atoms to the 16d sites. The atoms at a distance > $a/3$ from the center atom have been removed from (b) for clarity.

The method employed for fitting the scattering from the glass was really done for this research exclusively, but is adaptable to other glasses (I have done this recently for both neutron and x-ray scattering data not presented here). In addition, it would be interesting to see if anyone can improve upon the method and/or use it to describe a glass structure.

The use of the LeBail method to fit glass scattering is tricky but can be done repeatably and effectively with adequate practice. The tricky aspects are primarily due to the tendency of GSAS to crash in LeBail (glass) + Rietveld {phase(s)} modes during the least squares refinement immediately after running the Powpref subroutine, which would normally be done after any phase or profile parameters are changed manually. My approach to fitting scattering from the glass using GSAS is listed below. Note that this procedure assumes that the user is familiar with the software.

1) Fit the glass scattering with a polynomial, e.g., a shifted Chebseyev, first. This fit should be done by manually selecting points on the diffraction pattern that generally model the glass-scattering profile. The EXPGUI interface has a feature that allows manual fitting of the background. Do not refine the background further.

2) Model the Bragg-diffraction pattern(s) from crystalline phase(s). Fitting of the Bragg diffraction should ultimately be done in Reitveld mode, but can be done in LeBail mode as well. Refine the appropriate profile parameters using the least-

squares procedure to model the peak profiles as accurately as possible. After the refinement is done, turn off the profile-refinement flags for the crystalline phases.

3) Create a new phase that will be used for fitting the glass. As mentioned in the text, in this case a complex FCC structure was used, which fits the glass scattering quite well for both x-rays and neutrons for the VIT-105 glass (as well as several other Zr-based BMGs). The starting structure used is presented in Table B.1.

4) Before fitting the glass scattering, change the crystal-size-broadening coefficient to that of particles of ~ 3 nm. This coefficient is dependant on the profile function used for fitting. In the current case (synchrotron x-ray scattering), the broadening coefficient was the "LX" profile parameter in the Pseudo-Voigt profile function, but is either a directly or indirectly refinement parameter in all of the profile functions available in GSAS. If using another profile function, consult the GSAS manual (available via download at the Collaborative Computational Project Number 14 (CCP14) Homepage (http://www.ccp14.ac.uk) to find the appropriate parameter and its mathematical definition. The parameter value can be extracted from the mathematical definition.

Table B.1. Starting Structure Used for Modeling VIT-105 Glass
Scattering in GSAS

a (Angstroms)   12.200
Space Group   F d -3 m

Atom	Site	x/a	y/a	z/a	V_{iso}
Zr	48f	0.250	0.125	0.125	0.02
Zr	32e	0.500	0.500	0.500	0.02
Zr	16d	0.700	0.700	0.700	0.02

5) Next, go back to the background definition and fit it with a 2-term polynomial using two points near the low and high Q limits of the diffraction pattern. The fit should be a slightly-curved poly-line that matches the slope of the scattering pattern at the low and high Q limits, Fig. B.2. This background fit will be used later, but for now do not refine it.

6) Now, with all phases in Rietveld mode and ALL of the refinement flags off, run Powpref and Genles. This seems pointless, but is necessary to keep GSAS from crashing in the next step. In addition, any time that Powpref is run, this must be repeated. Note that if GSAS crashes at any point during fitting while running Genles, return to this step.

7) After running the pointless least-squares routine, switch the glass-approximation phase to LeBail mode and run Genles again refining the lattice parameter and particle-size-broadening coefficient, Fig. B.3. All flags for the crystalline phases

$(Zr_{52.5}Cu_{17.9}Ni_{14.6}Al_{10}Ti_5)_{99}Er_1$
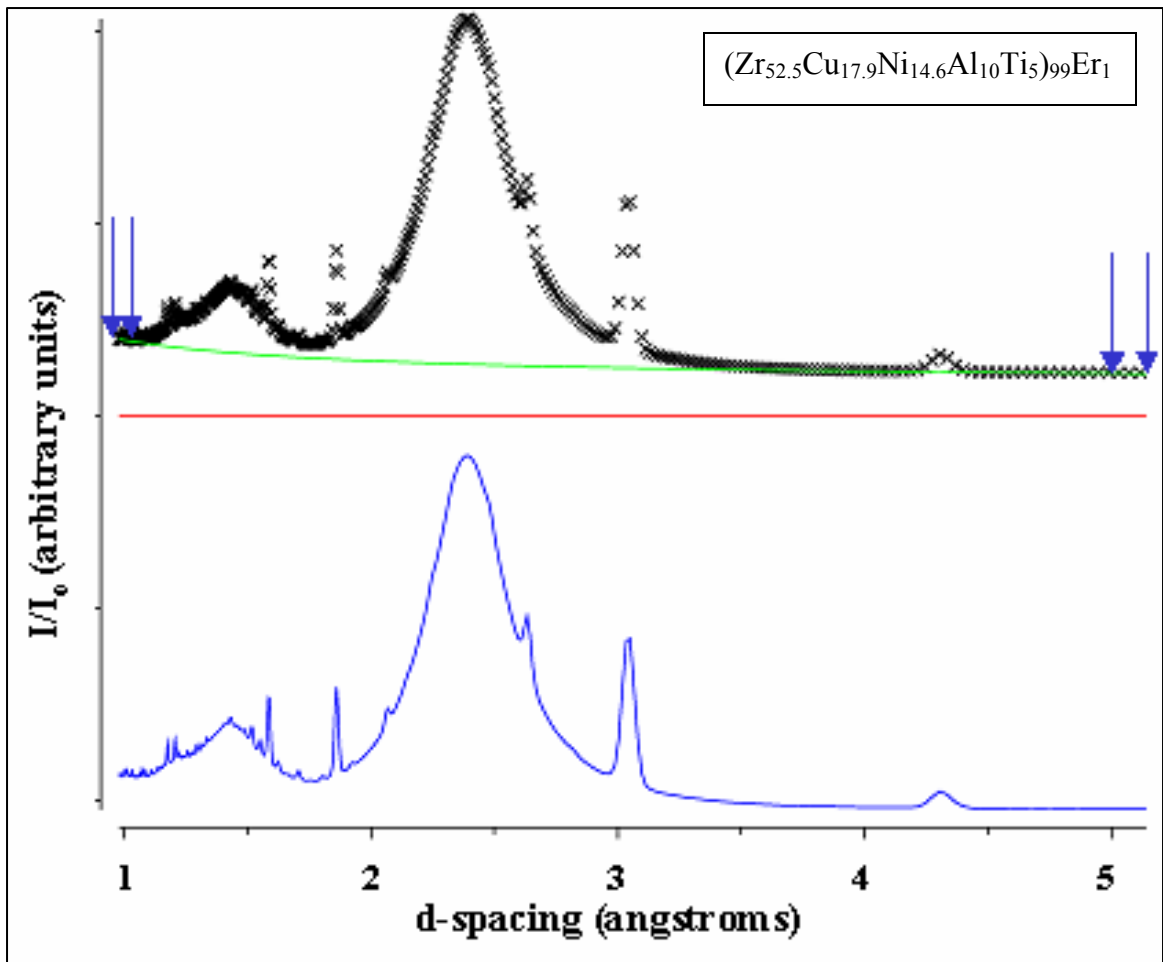
Figure B.2   (Upper) an example from GSAS of the manual background fit using a 2-term polynomial. The green curve is the background, the red line is the fit (zero for now), the crosses are the measured scattering-data points. The blue arrows indicate where the points for the fit were selected. (Lower) the difference curve. Note the patterns used for this demonstration are synchrotron x-ray patterns. The material is glassy VIT-105 + $(Er, Al)_2O_3$ (i.e., the 16,000-ppm-O, 10,000-ppm Er material presented in Chapter 5).
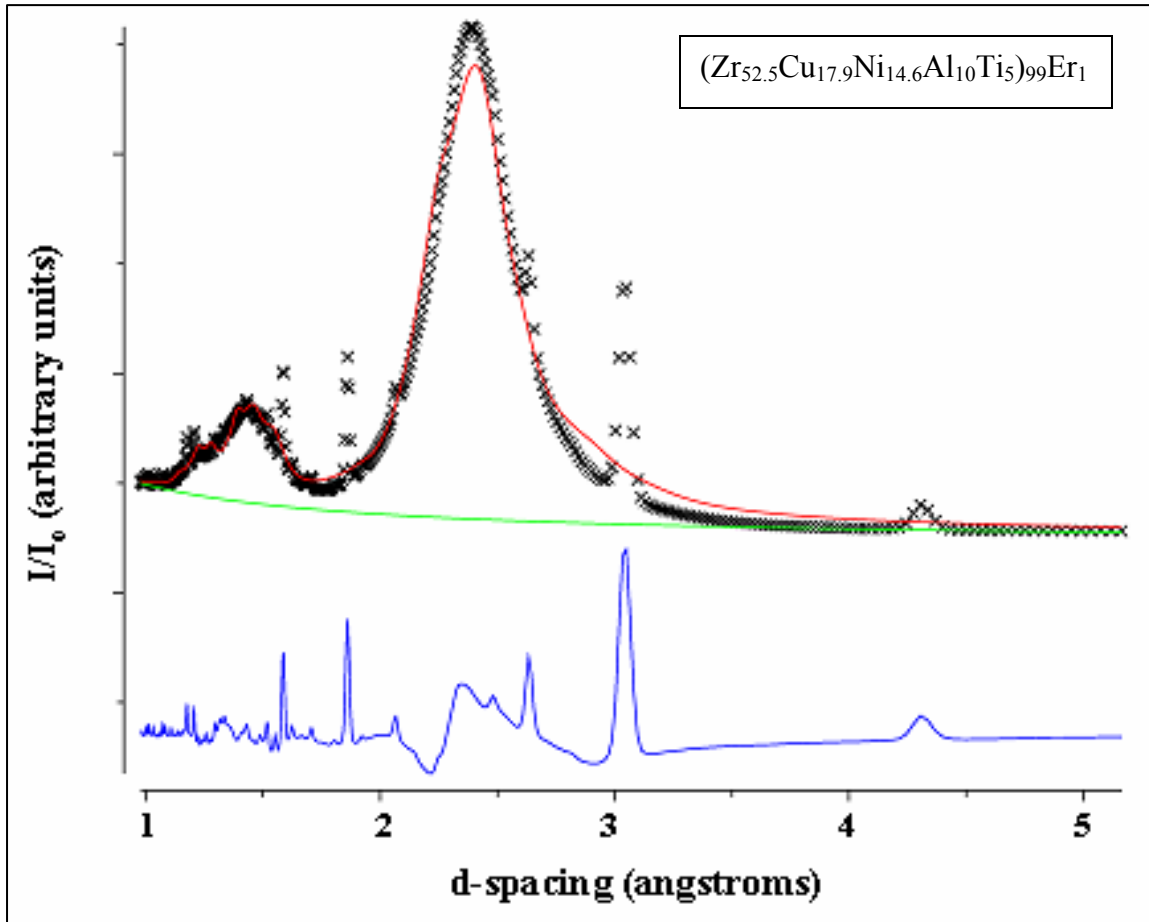
Figure B.3 The initial stages of the glass fit. This fit was generated by 10 least-squares iterations using the starting structure in LeBail mode and refining the particle-size broadening-coefficient and lattice parameter. Note the crystalline (Er, Al)$_2$O$_3$ phase has not been added at this point.

should be off. If the fit diverges, try turning the crystalline phase flags themselves off (i.e., remove the phases from the fit), and repeat step 6. The fit should start to model the glass scattering but the fit will not be very good. Refine the peak asymmetry and strain profile parameters and run Genles a few more times. In my case, this was adequate to obtain a good fit of the glass, but any variable in the profile function and/or structure can be refined, even if it is physically impossible (e.g., Uiso < 0). Be warned, however, that refining some parameters and creating a nonphysical fit should only be done if the fit is not being used to make any assertions whatsoever about the structure or volume fraction of the glass. In my case, this was not necessary, ultimately, but was done in the initial stages of developing the fitting method and would probably be useful for initial attempts at fitting a scattering from a glass; particularly one with a more complex local order.

8) After a obtaining a good fit with the glass scattering, for the glass phase: turn off all profile-parameter and phase-refinement flags with the exception of the lattice parameter – never turn this off or GSAS will crash. Refine the profile and phase coefficients for the crystalline phases further, together with the background, until you are satisfied with the overall fit, Fig. B.4.

The example figures shown are for a BMG containing a single crystalline phase. Note that this method can be used to fit multiple crystalline phases (as was the case in the figures presented in Chapter 6). This is, however, more tricky and takes a considerable

amount of computer and user effort. A general procedure for this is not available at the

moment, but the information provided here should act as a good starting basis.
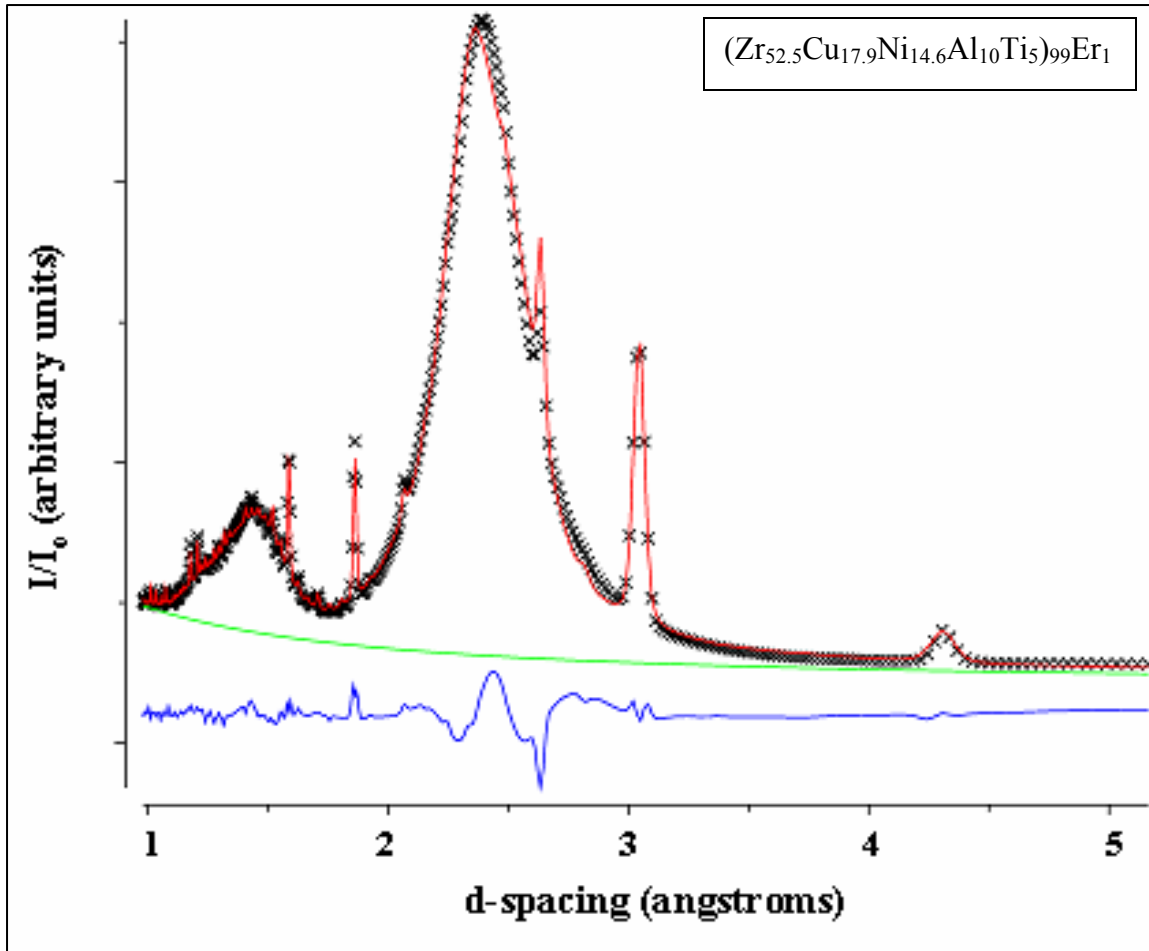
Figure B.4 The fit after adding the $(Er, Al)_2O_3$ phase and running Genles a few times, refining different paramenters. This fit still has a large amount of error but is beginning to model the glass nicely. From this point, careful iterations and the refinement of different parameters should be done on a trial and error basis to improve the fit.

Vita

James J. Wall (Joe) was born in St. Louis, Missouri in March 1978. He lived there until beginning his undergraduate studies at the University of Missouri in 1996. There he earned the degrees of Bachelor of Science and Master of Science in 2001 and 2003, respectively, in the field of mechanical and aerospace engineering with minor degrees in mathematics and materials science. He went on to pursue his doctorate in materials science and engineering at the University of Tennessee, which was granted in December 2007.

At the time of this writing, Joe resides in Los Alamos, New Mexico and works at the Manuel J. Lujan Jr. neutron scattering center at Los Alamos National Laboratory.